Titre: Title:	Photonic Implementation of the One-Way Model of Quantum Computation
Auteur: Author:	Yasaman Soudagar
Date:	2011
Type:	Mémoire ou thèse / Dissertation or Thesis
Référence: Citation:	Soudagar, Y. (2011). Photonic Implementation of the One-Way Model of Quantum Computation [Thèse de doctorat, École Polytechnique de Montréal]. PolyPublie. https://publications.polymtl.ca/734/

UNIVERSITÉ DE MONTRÉAL

PHOTONIC IMPLEMENTATION OF THE ONE-WAY MODEL OF QUANTUM COMPUTATION

YASAMAN SOUDAGAR
DÉPARTEMENT DE GÉNIE PHYSIQUE
ÉCOLE POLYTECHNIQUE DE MONTRÉAL

THÈSE PRÉSENTÉE EN VUE DE L'OBTENTION DU DIPLÔME DE
PHILOSOPHIÆ DOCTOR
(GÉNIE PHYSIQUE)
DÉCEMBRE 2011

UNIVERSITÉ DE MONTRÉAL

ÉCOLE POLYTECHNIQUE DE MONTRÉAL

Cette thèse intitulée :

PHOTONIC IMPLEMENTATION OF
THE ONE-WAY MODEL OF QUANTUM COMPUTATION

présentée par : SOUDAGAR Yasaman
en vue de l'obtention du diplôme de : Philosophiæ Doctor
a été dûment acceptée par le jury d'examen constitué de :

M. FRANCOEUR Sébastien, Ph.D., président
M. GODBOUT Nicolas, Ph.D., membre et directeur de recherche
M. STEINBERG Aephraim M., Ph.D., membre et codirecteur de recherche
M. AZANA José, Ph.D., membre
M. JENNEWEIN Thomas, Ph.D., membre

To my parents,
who gave me birth in Iran, and life in Canada...

Acknowledgment

When my family and I arrived in Canada so many years ago, even though we have lived through a revolution and an eight year war under a scary dictator regime, we were still innocent : We had not lived through immigration yet.

Upon our arrival at this vast, great country, where the sky is blue, our ship inevitably fell apart and each of us ended up on our own little raft in the middle of the ocean to survive. We did manage to keep each other in sight and shout encouragements at each other, but we did not have the power to help one another.

During this time, an incident with my younger brother, Yashar, gave me reason to do everything in my power to stay afloat. When we received our health cards there was the option of donating organs, which was a completely new notion to us. I decided it is a great idea and, one night during dinner, announced my decision of donating my organs after death to my family. My brother surprised me by suddenly getting really irritated and with a strangely distorted face and a voice full of pain almost screamed at me : "YOU CANNOT DO THAT !" After a moment I overcame my surprise at his strong reaction and realized it is the thought of my death that is causing him so much pain, not the organ donations !

After having to stay alive at least for the sake of my brother, what helped me swim was Kyokushin Karate, which is a full contact form of martial arts. The training itself pretty much prepares one to face life but, more importantly, Sensei Carl Choo was there for me as an older brother. He would talk to me when he would sense I had a problem and let me train, even though sometimes I could not afford to pay the fees. Sensei Carl and his wife, June, became my second family.

Meanwhile, on the academic side, pretty much since I arrived in Canada, Prof. John Sipe, in the University of Toronto, became my academic Godfather. The first time I met him, he took me to an office where his students were, pointed his finger towards a box which I knew was called a computer but had never touched before and a white book with a large blue letter C on it, and said somethings in English. I could read and write English to some extent then, but did not have proper listening comprehension and oral communication skills. I guessed he wanted me to learn the stuff in that book, which apparently had something to do with a computer. I vanished for a while, gathered money working in a coffee shop, bought a computer and took a course in Windows and Microsoft Office, where I learned what a file is and how to open it. My academic Godfather, John, has helped and supported me throughout the years in many different ways and even now continues to do so.

I am indebted to Dr. Yuri Medvedev and Dr. Victor Rodych. As my first contacts with

Canada's intellectual life, these amazing people made all the hardship of immigration worthwhile. Yuri, who recruited me for York University's Putnam team, had such an interesting approach to life that no matter what I felt when entering his office, when I was leaving it after only 2 minutes I would feel I am standing on the top of the Everest. Victor patiently taught me both English and Philosophy of Science. His classes were the most interesting and intriguing classes of my life.

I am thankful to my Masters' supervisor, Dr. Marko Horbatsch, for recruiting me to work with him.

When I decided to go to Montreal for my doctorate, Dr. Jose Fernandez was the professor who recruited me. During the very first week of my arrival at Polytechnique, he took me to a Quantum Information Conference and introduced me to Elham Kashefi. Elham not only became my collaborator but also a great friend and, in many cases, a role model. From her, I learned to have confidence in myself. She also introduced me to a number of mathematicians and scientists, whom in addition to being highly intelligent, turned out to be exceptional people and friends : Payman, Babak, Golnoosh, Moogeh, Ramin and Paul.

Finally, for my Ph.D. I joined the group of Nicolas Godbout in the Engineering Physics department. At that time, my sister and brother in law presented me the laptop I have used all these years and am using right now to write my thesis. A couple of years later, they gave birth to little Salma, and that pretty much resolved most of my existential issues. The birth of little Arian last year resolved all of it.

Upon my arrival at Nicolas' group, I met François Busque. He was the president of the OSA chapter and got me involved in it, through which I made many very good friends. From François I learned many things, such as the knots and bolts of leading an organization and also the importance of packaging ! I ended up doing a lot of community outreach, which has been a highly rewarding experience, as the result of François' existence and his character.

Then it was Bryan the Great (Burgoyne) or Bryan the therapist. Bryan would bring in a new game every single day and the whole group would play it during lunch. No need to say, he himself was the one winning all the time. Playing games was a very effective way of creating a sense of belonging and togetherness to most students in the group. Bryan never charged me a penny for all those counseling sessions he gave me in the Bat Cave. And then he recommended me to Genia Photonics for the new position they had available. I am really happy I will be in the same team as Bryan again.

Although the duration of the time I worked with Félix Bussières and Joshua Slater has been short, it has been very rewarding. You guys are definitely on my Physics Fantasy team.

Jean-Simon Corbeil is the funniest and most positive guy on the planet. Whenever I would start complaining about work he would say in a comic tone : "Come on Yas ! Tu es capable !"

With his tone and that sentence he would convey to me : “We are all confident that you can do it, so stop being a bore and do it !” During the past couple of years, especially during the past few weeks during writing my thesis, whenever I felt I cannot go on any longer, his exact sentence and tone rang in my head, bringing a smile to my lips and courage to my heart.

In addition, for more than the two and a half years I have been in Toronto, JS has picked up my paycheck every single month and has gone all the way to my bank and deposited the money into my account. Maybe one day I will get a chance to make up for this great help of yours JS !

I am particularly thankful to Brigitte Boissonneault, for putting so much effort in translating the abstract to French. During this very interesting process of translation, I came to appreciate the close connection between language and logic. That is because of the meticulous logic Brigitte applied to every single sentence I had written in English in the abstract. Brigitte is also impressive in the way she found the correct translation for all the expressions online, not only those related to general optics but also those specific to quantum information theory. Lets just say that at the end the French translation of the abstract turned out to be a much more elegant and accurate text than the original English, so much so that in some instances I changed the English text to match Brigitte’s elegant work ! I should thank Alex and Maryse for providing help for this part as well.

I am thankful to my other friends in Montreal, who have been a great support and the spice of my life : Maryse, Fanny, Mahasta, Fadwa, Lucie, Izabel and Caroline Boudoux.

I thank Mikaël Leduc, our lab technician for being the concrete supportive wall we could all lean on in the lab. I thank him also for showing me one of the most beautiful things I have seen in my life. When his first daughter, Maïa, was born, Mikaël came back to the lab after a couple of weeks of paternity leave. But in reality he was not there for quite a few days, because he was really walking on clouds. I had never seen a man walk on clouds before !

Of course, I thank Nicolas for his support, scientific and financial, throughout these years. But those are the usual goods that come with doing a Ph.D. Nicolas has given me two very important things which are not easy to come by. He literally taught me to be positive. Interesting enough, this happened when we were writing a grant proposal ! Before that I was not even aware of my attitude. Nicolas is the most liberal person I have ever met. He has set a great example for me on how to be liberal. Now I actively work on both these aspects of myself.

In addition to these, I have had great discussions with Nicolas about music and literature. It is a real pleasure to be able to talk to one’s Ph.D. advisor about different interpretations of Bach’s suites for solo Cello and minimalist composers.

I sincerely thank Mme. Lyne Dénomé and Mme. Joanne Sirois for always helping me out

with all the administrative and financial matters, even though they had to deal with me in English.

I thank Dr. Suzanne Lacroix, for her support and for teaching me French.

I can write a thesis on my experience with Aephraim Steinberg and his group at the University of Toronto, so what I will say here will not do justice.

It has been a great privilege to be in Aephraim's lab, photons side. A very important thing I have learned there is what it takes to be able to compete internationally. Being in this lab, I have been able to communicate my work to very well known scientists who would come to the department to give presentations and to visit the lab.

In addition to being intimidatingly smart, Aephraim is a great teacher and can give a profound understanding about very complex concepts. This has helped me gain a significant understanding of very interesting scientific material. I look forward haveing discussions about philosophy and literature with Aerphraim.

I am indebted to Aehphraim for all the support he has given me during the past couple of years, both for my scientific and outreach work.

It has been a rewarding experience to work with Xingxing, the Encyclopedia Fisica, and with Krister, the Mr. Fun, Lee-Dylan-Ardavan, The Trio, Amir, the Genius, and recently Alex, the Debater, who has also taught me how to write a resume.

I should thank my fabulous friends in Toronto, who are the greatest support : Aida, who has been my Sangé Sabur, Negar, who laughs with me, Nazanin, Babak and their two lovely girls, Shirin, Reza and their two lovely boys, Moogeh, who is a true inspiration, Behi, Sandrine and Aggie, the wonderful women, who have helped me with different aspects of my thesis, and my Capoira gang, especially, Prof. Kmelo, Tomatinho, Microphone, Modelo and Coruja.

More than a year ago, I met my fabulous partner, Jalani. Since then, he has given me so much support I sometimes wonder if I am abusing his kindness. Other than feeding me and putting up with my stressed behavior, countless times, he let me go to his home after taking data, at 3, 4, 5 am, even though he would have to wake up to go to work at 7 am.

Over many months, he has patiently listened to the problems I have had with the setup and gave me suggestions. He has lent me his tablet for doing graphs, read my thesis, chapter by chapter, corrected the English and gave suggestions for improvement and helped me compile it. Whenever I felt weak, he picked me up by encouragements and sharing his experience going through the same process.

Finally, I should thank the people who have had the most influence on my life : my parents. As time passes by, I realize more and more what a great sacrifice it has been for them to sell all their belonging in 20 days and move to Canada. Since middle school, which was the time

I got exposed to science, my dream was to become a scientist. In first year of high school, I fell in love with Physics and Biology. I decided to do Physics to prove women can also be physicists. If my parents had not made this sacrifice and we hadn't come to Canada, I simply would not be able to realize my childhood dream. Yes, it is possible to make dreams come true on a raft! My parents have given me tremendous support, both financial and otherwise during the time I am in Toronto. The financial help from my mother got me out of the gypsy life here and spared me from starvation.

By now, we have connected back our rafts to each other and are not in the danger of drowning any longer. My sister, Tanaz, who is older than I, has been a great support and inspiration. Her GPA in high school was simply the perfect 100%, so obviously I could never keep up with her. At a time when no one knew what a computer was back home, she majored in computer engineering. I always wonder where she got the idea from! Later on, she did an MBA in Sloan, MIT and has a successful career and a beautiful family.

My brother, whom I am very proud of, is a successful Mechanical M.Eng. and P.Eng. I always tease him over being a superficial engineer as opposed to a deep physicist. I hope my achievements, and those of my siblings, make my parents' sacrifices worthwhile.

I am mostly proud of my parents, who were both retired back home. They learned English and entered the professional Canadian job market. My Mother is a teacher in Toronto School Board and my father works as a technician for a Canadian company. They are so capable, sometimes I wonder what they would have become if they were born in Canada!

For me, doing my Ph.D. has been a great journey, during which I have grown significantly as a person and become who I am now. A journey that has given me the rare privilege of being among and working with some of the most exceptional people on this planet.

Résumé

Le calcul quantique par consommation d'intrication requiert comme ressource initiale un type particulier d'état intriqué, les Â«états graphesÂ». Il s'effectue en mesurant des bits quantiques (qubits) uniques dans différentes bases. Ces bases dépendent de l'algorithme utilisé et des résultats des mesures précédentes. Ainsi, on doit pouvoir stocker les nouveaux qubits d'une certaine faÃ§on pendant qu'on traite les résultats des mesures précédentes.

Pour la mise en application de ce modèle (le calcul par consommation d'intrication) en photonique, les fibres optiques constituent la manière la plus pratique de stocker des qubits. Le temps d'arrivée de chaque photon au détecteur, que l'on nomme qubit temporel, est le degré de liberté le plus robuste associé aux photons se propageant dans les fibres optiques. Pour créer la ressource intriquée initiale, on doit d'abord produire des paires de photons EPR, photons qui sont totalement indifférenciables les uns des autres dans tous leurs degrés de liberté, sauf celui qui permettra d'encoder les qubits logiques. Ces paires de photons sont combinées au moyen de portes fusion pour produire des états graphes plus grands. Les portes fusion ne sont pas déterministes et elles présentent une probabilité limitée de succès. De plus, il faut pouvoir stocker les photons. Pour la réalisation de ce modèle basé sur les qubits temporels, on utilise une combinaison particulière de coupleurs 50/50 tout-fibre et de modulateurs électro-optiques pour constituer les portes fusion, ainsi que les portes à qubit unique arbitraires, qui sont nécessaires au calcul en soi. Ces deux étapes, soit la production de graphes au moyen des portes fusion et l'exécution du calcul quantique, exigent le stockage de qubits temporels, ce que la méthode proposée utilisant la fibre optique permet de faire tout naturellement.

L'une des questions auxquelles se sont intéressés les mathématiciens qui travaillent sur le calcul par consommation d'intrication est la détermination des calculs possibles à partir d'un état graphe donné, ainsi que les possibilités de qubits d'entrée et de sortie pour cet état graphe. Les études qu'ils ont faites ont permis d'établir un algorithme utilisé pour élaborer une séquence de mesures et de corrections menant à un calcul déterministe à partir d'un état graphe. Cette séquence est ce qu'on appelle un flot simple tracé sur un graphe. Récemment, on a modifié cet algorithme de manière à trouver le flot généralisé, soit une séquence de calculs sur des graphes présentant des géométries particulières, comme des graphes contenant des structures en boucle. Dans le cadre de cette thèse, nous avons expérimentalement réalisé un graphe en boucle à 4 qubits comportant un qubit d'entrée, c'est-à-dire le plus petit graphe admettant un flot généralisé mais pas de flot simple. Les graphes de ce type à structure en boucle conduisent à une boucle temporelle, donc un circuit non exécutable. Toutefois,

l'utilisation d'un flot généralisé nous permet de trouver un circuit équivalent au graphe en boucle, mais qui respecte la ligne de temps ordinaire et qui peut être exécutable.

Bennett, Schumacher et Svetlichny (BSS) ont proposé d'utiliser la téléportation quantique et la post-sélection pour simuler des boucles temporelles. Il se trouve que des boucles temporelles surviennent naturellement dans le cadre du calcul par consommation d'intrication réalisé avec des états graphes. De plus, le circuit équivalent au graphe en boucle à 4 qubits que nous avons créé est aussi équivalent à la proposition de BSS, dans le cas où la post-sélection du modèle de BSS réussit. Autrement dit, notre graphe en boucle à 4 qubits simule une boucle temporelle sans l'utilisation de la post-sélection.

Pour réaliser le graphe de notre expérience, nous avons utilisé deux degrés de liberté (la trajectoire et la polarisation) de deux photons. Nous avons commencé par produire une paire de photons intriqués en polarisation selon le mécanisme de la conversion paramétrique spontanée, au sein d'un cristal PPKTP. Nous avons ensuite introduit les qubits trajectoire à l'aide de diviseurs de faisceau 50/50. Une combinaison inédite de lames demi-onde a servi à appliquer la porte ¡¡ contrôle-Z ¿¿ requise entre le degré de liberté polarisation d'un photon et le degré de liberté trajectoire d'un autre photon. Notre expérience est la première expérience connue portant sur une opération à 2 qubits entre des degrés de liberté distincts de photons différents qui n'utilise que des effets optiques linéaires. à l'aide d'autres lames demi-onde stratégiquement positionnées, des opérations ¡¡ contrôle-Z ¿¿ ont été appliquées aux degrés de liberté polarisation et trajectoire d'un même photon, ce qui a mené à la création d'un graphe en boucle à 4 qubits.

Nous avons effectué des simulations pour étudier les effets des erreurs découlant d'éléments optiques réalistes et d'alignements imparfaits, et ce, afin de comprendre pleinement les résultats de l'expérience. Les erreurs de précision dans l'ajustement de l'orientation des lames à retard utilisées pour créer l'état graphe et leur déphasage détériorent de 2% la fidélité de l'état par rapport à l'état cible, la faisant passer à 98%. Le réglage imparfait des phases des interféromètres peut dégrader davantage la fidélité, l'établissant à 93%. Toutefois, aucune de ces erreurs n'a d'effet sur la pureté de l'état. Une autre source d'erreurs concerne la visibilité des interféromètres, évaluée à environ 93% dans notre expérience. D'autres erreurs sont liées au débalancement entre les bras de chaque interféromètre et à la qualité des paires de photons intriqués en polarisation. En raison de la sensibilité élevée de la source aux fluctuations de température, l'état de polarisation de ces paires de photons a une pureté d'environ 85% et la fidélité par rapport à l'état cible est de 87% à 91%. Une simulation qui combine ces trois sources d'erreurs indique que celles-ci peuvent mener la fidélité de l'état à un taux aussi bas que 80%. Si l'on tient compte de toutes ces sources d'erreurs, on est en droit de s'attendre à ce que le taux le plus bas de fidélité de l'expérience par rapport aux états cibles soit inférieur

à 70%.

Pour évaluer expérimentalement l'état créé, nous avons réalisé 256Â mesures, soit des mesures dans 16Â bases ajustées pour les qubits polarisation et, à chacun de ces ajustements, des mesures dans 16 autres bases ajustées pour les qubits trajectoire. Pour chaque ajustement de base en polarisation, nous avons procédé à une tomographie sur les 2 qubits trajectoire, et la matrice de densité correspondante a été reconstituée grâce aux méthodes de l'inversion linéaire et du maximum de vraisemblance. Nous avons ensuite comparé les résultats de l'expérience aux résultats de l'état cible idéal, tel que prédit par la simulation de l'expérience. La pureté des matrices de densité ainsi reconstituées varie de $0,72$ à 1. Quant à la fidélité par rapport à l'état cible idéal, elle se situe entre $0,62$ et $0,96$. Si l'on tient compte des erreurs expérimentales, ces valeurs se trouvent dans la gamme des résultats attendus et montrent que nous avons créé un état graphe à 4 qubits coïncidant raisonnablement avec l'état cible.

En utilisant l'état graphe créé comme ressource initiale pour le calcul par consommation d'intrication, nous avons réalisé trois calculs correspondant à trois choix différents de bases de mesure pour les qubits polarisation. Les résultats de ces calculs concordent avec l'état cible attendu, la fidélité étant de 90% et la pureté, de $0,90$.

En plus de proposer une nouvelle méthode pour l'utilisation des fibres optiques dans le calcul par consommation d'intrication, l'état graphe à 4 qubits est expérimentalement créé à l'aide des degrés de liberté polarisation et trajectoire de deux photons. Cette structure de graphe constitue le plus petit graphe admettant un flot généralisé, mais pas de flot simple. La structure en boucle de ce graphe, créée au moyen d'une nouvelle méthode expérimentale, permet de simuler des boucles temporelles sans avoir recours à la post-sélection.

Abstract

The one-way model of quantum computation (QC) uses a particular type of entangled state as its initial resource, which are called graph states. The computation is then performed by measuring single qubits in various bases. These bases depend on the algorithm that is being implemented and the results of the previous measurements. Hence, the qubits need to be stored in some way, while the results of the previous measurements are being processed.

For the photonic implementation of this model, optical fibers are the most practical choice for storing the qubits. The arrival time of each photon at the detector, referred to as the time-bin qubit, is the most robust physical degree of freedom of photons in optical fibers. In order to make the initial entangled resource, one first produces EPR-type entangled pairs of photons, which are fully indistinguishable in all their degrees of freedom, but the one that is encoding the logical qubits. Using fusion gates, these photon pairs are combined to produce larger graph states. Fusion gates are not deterministic and have a finite probability of success. For them to be scalable, one further requires storage of photons. For the implementation of this model by time-bin qubits, one uses a special combination of all-fiber $50:50$ couplers and electro-optical modulators to perform the fusion gates, in addition to the arbitrary single qubit gates necessary for performing the computation itself. Both these steps, namely the production of graphs using fusion gates and performing the quantum computation, require storage of time-bin qubits, which is implemented naturally in the proposed scheme that takes advantage of optical fibers.

One of the questions that has been addressed by the mathematicians working on the one-way model is how to figure out what computations are possible, if any, by a given graph state and the choices of input and output qubits on this graph state. These studies have led to the development of an algorithm for finding a proper pattern of measurements and corrections that leads to deterministic quantum computation on the graph state. This pattern is said to be a *flow* on the graph. Recently this algorithm is generalized to finding the *generalized flow*, which are computation patterns on graphs with interesting geometries, such as graphs that contain loop structures. We experimentally realize a 4-qubit loop graph with an input qubit that renders it to be the smallest graph with a generalized flow and no flow. Such graphs with a loop structure result into a time-like loop and thus a circuit that is not runnable. Using generalized flow, however, allows us to find an equivalent to the loop graph that respects the ordinary time line and is runnable.

Bennett, Schumacher and Svetlichny (BSS) have proposed using quantum teleportation and post-selection to simulate time-like loops. It is shown that time-like loops arise naturally

in the frame work of the one-way model of QC with graph states and the equivalent circuit to the created 4-qubit loop graph is equivalent to the proposal of BSS, provided that the post-selection in the BSS model has succeeded. Hence, our 4-qubit loop graph simulates a time-like loop without the use of post-selection.

For the experimental realization of this graph, we use the polarization and path degrees of freedom of two photons. A pair of polarization entangled photons are first generated using Spontaneous Parametric Down Conversion in a PPKTP crystal. The path qubits are then added using $50:50$ beam splitters. A novel combination of half-wave plates then applies the required controlled-Z gate between the polarization degree of freedom of one photon and the path degree of freedom of the other one. This experiment is the first reported experiment that is performing a 2-qubit operation between degrees of freedom of different photons using only linear optics. Using other strategically placed half-wave plates, controlled-Z operations are added to the polarization and path degrees of freedom on the same photon and the 4-qubit loop graph is thus created.

To fully characterize the experiment, simulations are performed to study the effects of errors from realistic optical elements and alignment. Inaccuracies in the angle of the wave plates that create the graph state and their retardance reduce the fidelity of the state with the target state by 2%, to 98%. The inaccurate setting of phases of interferometers can reduce the fidelity further down to 93%. None of these errors affect the purity of the state. Another source of error is the imperfect visibility of the interferometers, which are about 93% in our experiment. Other errors are introduced by the unbalanced losses in different arms of each interferometer and the quality of the polarization entangled photon pairs. Due to the high sensitivity of the source to temperature fluctuations, the polarization state of these photon pairs has purity of about 85% and the fidelity with the target state of 87% to 91%. A simulation that combines these three sources of error shows they can reduce the fidelity of the state to as low as 80%. Taking all these sources of errors into account, one can expect the lower bound of the experimental fidelity with target states to be less than 70%.

In order to experimentally characterize the created state, $16 \times 16 = 256$ measurements are performed. These measurements include 16 measurement basis settings on polarization qubits and for each of these settings there are 16 basis settings for path qubits. For each polarization basis setting, 2-qubit tomography is performed on path qubits and the corresponding density matrix is reconstructed using the methods of Linear Inversion and Maximum Likelihood. The experimental results are then compared to the results from the ideal target state predicted from the simulation of the experiment. The purities of these reconstructed density matrices range from 0.72 to 1. The fidelities with the ideal target sate range from 0.62 to 0.96. Taking the experimental errors into account, these values fall within the expected results and show

that we have created the 4-qubit graph state with a reasonable overlap with the target state.

Using the created graph state as the initial resource for one-way quantum computing, three computations corresponding to three different choices of measurement basis for polarization qubits are performed. The results of these computations are in agreement with the expected target state with fidelities of 90% and have purities of 0.90.

In addition to the proposal of a novel scheme to implement the one-way model of QC in optical fibers, a 4-qubit graph state is experimentally created using polarization and path degrees of freedom of two photons. This graph structure is the smallest graph that can have a generalized flow and no flow. The loop structure of this graph, that is created by a novel experimental method, allows the simulation of time-like loops without the need to post-selection.

Contents

List of Figures

List of Appendices

List of Acronyms and Abbreviations

cZ	controlled-Z
cNOT	controlled-NOT
H	Hadamard
DOF	Degree of Freedom
DOFs	Degrees of Freedom
EPR	Einstein-Podolsky-Rosen
NMR	Nuclear Magnetic Resonance
EOM	Electro-Optic Modulator
SPDC	Spontaneous Parametric Down Conversion
SHG	Second Harmonic Generation
PBS	Polarization Beam Splitter
PBD	Polarization Beam Displacer
ICFO	The Institute of Photonic Sciences
QC	Quantum Computation
WP	Waveplate
HWP	Half-Wave Plate
QWP	Quarter-Wave Plate
GHZ	Greenberger-Horne-Zeilinger
BS	Beam SPlitter
CTC	Closed Time-like Curve
SGK	da Silva, Galvao and Kashefi
BSS	Bennett, Schummacher and Svetlichny
PPKTP	Periodically Poled Potassium Titanyl Phosphate
KTP	Potassium Titanyl Phosphate
SMF	Single Mode Fiber
FPGA	Field-Programmable Gate Array

Chapter 1

Introduction

In mathematics, there are some problems that are *hard* to solve in the sense that the amount of resources necessary, for example the amount of computational time, grows exponentially with the size of the problem. Hence, one may require more time than the age of the universe to solve the problem. One example of such problems is the simulation of quantum mechanical systems, where the amount of required computation time grows exponentially with the size of the system. Another example is the Factoring problem, in which one tries to find the prime factors from their product. As the size of this product grows, it becomes practically impossible to find the prime factors. This problem is famous mostly for its use in cryptography. For secure communication between two parties, Alice and Bob, Alice generates a key that uses the the prime factors of a number and requires the public announcement of multiple of the prime numbers. An Eavesdropper cannot read the message because it takes her an impractical amount of time to find the prime factors of the publicly announced number.

In 1994, Peter Shor came up with the specific algorithm (Shor, 1994) that uses quantum mechanics to find prime factors of an integer. The number of gates or computational time needed by this algorithm grows polynomially with the size of the integer. This means that a quantum computer renders some present cryptography systems obsolete. Since Shor's factoring algorithm was proposed, there has been much effort in realizing a quantum computer. Although the possibility of solving *hard* problems in polynomial time has created a lot of interest in the computer science community, the possibility of having a quantum computer is particularly interesting to physicists because it is the only machine that can efficiently simulate a quantum mechanical system (Feynman, 1982).

1.1 Basic Concepts of Quantum Information Processing

The logical unit of information for a quantum computer is the quantum bit or qubit. It is a linear combination of $|0\rangle$ and $|1\rangle$, $\alpha|0\rangle + \beta|1\rangle$, such that α and β are complex numbers and $|\alpha|^2 + |\beta|^2 = 1$. Here $|0\rangle$ and $|1\rangle$ are the quantum states of a system being in one

level, denoted $|0\rangle$, or in another, denoted $|1\rangle$. Upon measuring a qubit, one obtains $|0\rangle$ with probability $|\alpha^2|$ and $|1\rangle$ with probability $|\beta^2|$. The computation is equivalent to the application of multi-qubit unitary operations to these qubits. Until 2001, the standard way to think of a quantum computation was to think of a *quantum circuit* (Nielsen et Chuang, 2000). A quantum circuit consists of *lines* that represent the path a logical qubit takes to travel in the circuit. These lines are connected to each other through *gates*, which are the multi-qubit unitary operations to be applied among the qubits. Fig. 1.1 shows an example of a 2-qubit quantum circuit (Nielsen, 2006) and some quantum gates. The input to this circuit

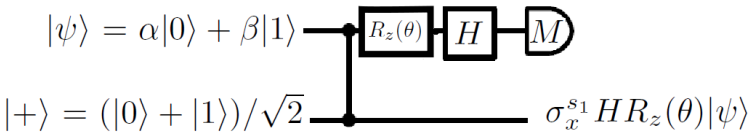

Figure 1.1 An example of a 2-qubit quantum circuit. s_1 is result of measuring the upper qubit and has a value of either 0 or 1.

is

$$|\Psi\rangle|+\rangle = (\alpha|0\rangle + \beta|1\rangle) \otimes \frac{|0\rangle + |1\rangle}{\sqrt{2}} = (\alpha|00\rangle + \alpha|01\rangle + \beta|10\rangle + \beta|11\rangle)/\sqrt{2}$$

The gate between the upper and lower lines, shown by the two connected dots, represents a controlled-Z (also denoted as cZ), which is represented by the matrix

$$controlled - Z = \begin{pmatrix} 1 & 0 & 0 & 0 \\ 0 & 1 & 0 & 0 \\ 0 & 0 & 1 & 0 \\ 0 & 0 & 0 & -1 \end{pmatrix}.$$

The matrices representing the gates are applied to the coefficients of states in the order $|0\rangle$, $|0\rangle$ or $|00\rangle$, $|01\rangle$, $|10\rangle$, $|11\rangle$.

The gates which are applied to the upper line are single qubit gates and are:

$$R_z(\theta) = \begin{pmatrix} 1 & 0 \\ 0 & e^{i\theta} \end{pmatrix},$$

which is a rotation of θ around the z axis of the Bloch Sphere (Fig. 1.2) and Hadamard which applies the following operation:

$$H = \frac{1}{\sqrt{2}} \begin{pmatrix} 1 & 1 \\ 1 & -1 \end{pmatrix}.$$

M stands for measurement. Here we study the action of the circuit on the inputs. The

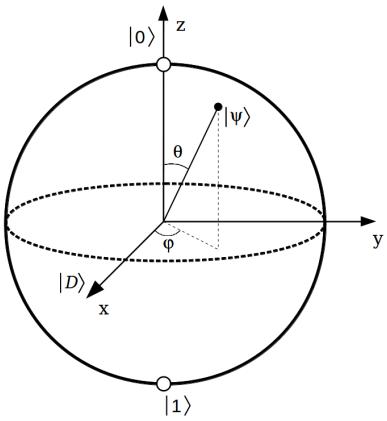

Figure 1.2 Any qubit $\alpha|0\rangle + \beta|1\rangle$ can be represented by a point on the surface of the Bloch sphere, such that $\alpha = \cos(\theta/2)$ and $\beta = e^{i\phi}\sin(\theta/2)$. The radius of the sphere is 1.

controlled-Z gate applies a π phase shift to the second qubit when both first and second qubits are 1:

$$|\psi_0\rangle = cZ|\Psi\rangle|+\rangle = (\alpha|00\rangle + \alpha|01\rangle + \beta|10\rangle - \beta|11\rangle)/\sqrt{2}$$

The single qubit gates are then applied in their appropriate chronological order, which is from left to right, to the upper qubit:

$$\begin{aligned}
R_{z_1}(\theta)|\psi_0\rangle &= (\alpha|00\rangle + \alpha|01\rangle + e^{i\theta}\beta|10\rangle - e^{i\theta}\beta|11\rangle)/\sqrt{2} \\
H_1R_{z_1}(\theta)|\psi_0\rangle &= (\alpha|00\rangle + \alpha|10\rangle + \alpha|01\rangle + \alpha|11\rangle \\
&+ e^{i\theta}\beta|00\rangle - e^{i\theta}\beta|10\rangle + e^{i\theta}\beta|01\rangle - e^{i\theta}\beta|11\rangle)/2 \\
&= |0\rangle \otimes ((\alpha + \beta e^{i\theta})|0\rangle + (\alpha - \beta e^{i\theta})|1\rangle)/2 \\
&+ |1\rangle \otimes ((\alpha - \beta e^{i\theta})|0\rangle + (\alpha + \beta e^{i\theta})|1\rangle)/2 \\
&= |0\rangle \otimes HR_z(\theta)(\alpha|0\rangle + \beta|1\rangle)/2 \\
&+ |1\rangle \otimes \sigma_x HR_z(\theta)(\alpha|0\rangle + \beta|1\rangle)/2,
\end{aligned}$$

where

$$\sigma_x = \begin{pmatrix} 0 & 1 \\ 1 & 0 \end{pmatrix}.$$

This means that when one measures 0 on the upper qubit, the state of the lower qubit is $HR_z(\theta)(\alpha|0\rangle+\beta|1\rangle)$ and when one measures 1 on the upper qubit, the state of the lower qubit is $\sigma_x HR_z(\theta)(\alpha|0\rangle + \beta|1\rangle)$. If one denotes the result of the measurement of the upper qubit by s_1, one can write the state of lower qubit to be $\sigma_x^{s_1} HR_z(\theta)|\psi\rangle$. s_1 has the value of either

0 or 1. Note that the initial qubit on the upper line, $|\psi\rangle$, is not lost after the measurement, but it is transferred to the lower line with some known unitary operations applied to it.

In practice, performing multi-qubit unitary operations is a rather difficult task to accomplish. In 2001, Raussendorf and Briegel (Raussendorf et Briegel, 2001) proposed a novel method for quantum computing, which they called the one-way model. In their method one starts with a special entangled state of n qubits. This state can be represented by a mathematical graph, such that each vertex corresponds to a qubit in the state $(|0\rangle + |1\rangle)/\sqrt{2} = |+\rangle$ and each edge corresponds to a controlled-Z between the connected vertices (Fig. 1.3).

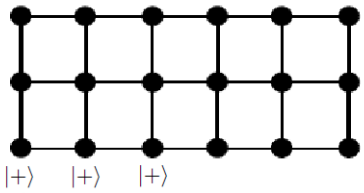

Figure 1.3 An entangled state used as an initial resource for the one-way model of quantum computation. Each vertex is a qubit in state $|+\rangle$ and each edge represents a controlled-Z operation between the connected vertices.

The computation is then accomplished by performing single qubit measurements in various bases that are equivalent to applying $R_z(\theta)$ followed by a *Hadamard*. The *absolute values* of the rotation angles, θ, are determined by the algorithm that is being implemented and the signs of the angles are determined by the results of measurements of the previous qubits (Nielsen, 2006). In order to get some understanding of how the one-way model of quantum computing works, consider the graph of Fig. 1.4.

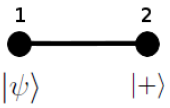

Figure 1.4 The smallest graph. After measurement of qubit 1, the information *flows* to qubit 2.

The state corresponding to this graph is

$$\alpha|00\rangle + \alpha|01\rangle + \beta|10\rangle - \beta|11\rangle$$

where one considers the first qubit, $\alpha|0\rangle + \beta|1\rangle$, to be the input and the qubit that will be measured and the second qubit the output, which will not be measured.

To measure qubit one in basis $HR_z(\theta)$, one applies these operations to qubit one, then sends qubit one to the measuring apparatus. Note that this is the same operation that was performed by the circuit of Fig. 1.1. If qubit one is measured to be 0, the output qubit will be in state $HR_z(\theta)(\alpha|0\rangle + \beta|1\rangle)$, i.e. the second qubit will now carry the logical value of the first qubit subjected to single qubit operations. If the first qubit is measured to be 1, the second qubit will be in state $\sigma_x HR_z(\theta)(\alpha|0\rangle + \beta|1\rangle)$, which is similar to the case when qubit one is measured to be 0, but with an extra σ_x correction. In neither case is the information that was carried on qubit 1 lost. One says the information *flowed* from qubit 1 to qubit 2 and qubit 2 might need to receive a σ_x correction, depending on the measurement result of qubit 1.

In order to see how the *sign* of the measurement angle depends on the result of previous measurement results, we look at the case when the graph contains 3 consecutive qubits (Fig. 1.5). Here, measuring qubit 1 with angle θ_1 leaves the state of the remaining two qubits

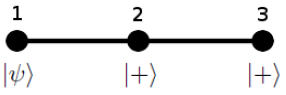

Figure 1.5 The choice of the sign for the measurement angle of qubit 2 depends on the measurement result of qubit 1. The information *flows* from qubit 1 to qubit 2 and from 2 to 3.

at

$$cZ_{2,3}\sigma_x^{s_1} HR(\theta_1)|\Psi\rangle|+\rangle,$$

where s_1 is the result of the measured qubit 1, which has the value of either 0 or 1. In a similar fashion, measuring qubit 2 in basis corresponding to angle θ_2 leaves qubit 3 in state

$$\sigma_x^{s_2} HR(\theta_2)\sigma_x^{s_1} HR(\theta_1)|\Psi\rangle,$$

where s_2 denotes the result of measurement of qubit 2. It is now interesting to look at the $R(\theta_2)\sigma_x^{s_1}$ part of the operators that are acting on $|\Psi\rangle$. If $s_1 = 0$, then $R(\theta_2)\sigma_x^{s_1} = \sigma_x^{s_1} R(\theta_2)$. If $s_1 = 1$, then one can easily show that $R(-\theta_2)\sigma_x^{s_1} = e^{-i\theta_2}\sigma_x^{s_1} R(\theta_2)$. On the other hand, $H\sigma_x^{s_1} = \sigma_z^{s_1} H$. So one can rewrite the order of the operations that are done on qubit 3 as

$$\sigma_x^{s_2}\sigma_z^{s_1} HR(\theta_2)HR(\theta_1)|\Psi\rangle.$$

Hence the choice of sign of θ_2, based on the measurement result of qubit 1 allows the correction due to this measurement to be pushed to the end of the computation, which in this example is after measuring qubit 2. One says that at each time step one needs to feed forward the

measurement results to determine the bases for the qubits that are to be measured in the next time step. The feed forward of these results allows for the one-way model of quantum computation to deterministically implement a computation.

In order for this model to be capable of universal quantum computing, it should be able to realize controlled-Z, *Hadamard* and arbitrary single qubit rotation. The initial resource already contains qubits which are connected to each other through controlled-Z. A *Hadamard* can be implemented by choosing the measurement angle, θ, to be zero. An arbitrary rotation on a single qubit, $|\psi\rangle$, can be implemented by having a 3-qubit line graph connected to it by a controlled-Z. Then one decomposes the rotation into its corresponding three Euler angles, κ_x, $\pm\gamma_z$ and $\pm\delta_x$. The qubits attached to $|\psi\rangle$ are then each measured respectively with an Euler angle, such that the one farthest from the rotating qubit is measured in κ. These operations rotate the initial qubit to $(\kappa_x)(\pm\gamma_z)(\pm\delta_x)|\psi\rangle$ up to known single qubit corrections. Thus the one-way model of quantum computation is universal, meaning it can do universal quantum computing.

1.2 Challenges

The main difficulty in the realization of a quantum computer that works based on the one-way model is in the creation of the initial entangled state, also called the graph state. This initial state is, in fact, the eigenstate of an Ising type Hamiltonian (Raussendorf *et al.*, 2003). For this reason their realization in systems such as optical lattices, where controllable nearest neighbor interaction is a major property of the system, seems promising. However, although great advancement is made in these systems the decoherence still remains an issue (Bloch, 2008).

Another way to approach the problem is using various degrees of freedom (DOF) of photons as the physical carriers of logical qubits to reconstruct the initial entangled state. For example, one can use the polarization of a photon as a qubit, such that the *horizontal* polarization is logical 0 and *vertical*, logical 1. The polarization of a photon can always be written as a linear combination of *horizontal* and *vertical*, i.e. $\alpha|H\rangle + \beta|V\rangle$. It is possible to create pairs of photons in an EPR-like entangled state $(|HH\rangle+|VV\rangle)/\sqrt{2}$ (Kwiat *et al.*, 1999), (Kwiat *et al.*, 1995), (Stevenson *et al.*, 2006), called a Bell pair. This Bell pair is equivalent to the 2-qubit graph of Fig. 1.4, where both qubits are in state $|+\rangle$ before the controlled-Z operation is applied, up to a Hadamard operation on one of the qubits. Any desired graph state can then be constructed by first performing a so called *fusion gate* between these pairs and then between the larger resulting graphs and these pairs (Browne et Rudolph, 2005). We will extensively discuss three DOFs of photons, including polarization,

the methods of creating Bell pairs in each DOF and the fusion gates corresponding to each one, plus the methods of experimentally manipulating them in the next chapter.

There are a number of problematic elements in both the sources of Bell pairs and the requirements for the fusion gate. The creation of photon pairs is still widely non-deterministic, and for the deterministic cases, is highly non-efficient. On the other hand, for the fusion gate to work, one requires the photons to be, in principle, indistinguishable including having the same frequency bandwidth. It is very hard to achieve this indistinguishability directly from the source. The practical method various experimental groups have adapted is to create the pairs from different sources, then ensuring the same frequency profile by filtering (Zhao *et al.*, 2004). This method results into even smaller number of photon pairs.

The fusion gate, that is successful with probability 1/2, is a scalable method, however one needs to store the photons that have already successfully exited the fusion gates, such that they do not lose coherence, while one is waiting for each future gate to be successful. Due to all these difficulties, it is highly desirable to create any required graph with the smallest number of photons. Using different degrees of freedom of photons will potentially make this possible.

1.3 Research Objective

There are two main objectives of the work presented in this thesis. The first is to study the implementation of the one-way model of quantum computation using the so called *time-bin* degree of freedom of photons. The second objective of this work is dedicated to the experimental realization of a 4-qubit *loop* graph, using polarization and path degrees of freedom of photons. This graph has a number of interesting properties related to the theory of measurement-based quantum computation and also to the concept of time-like curves. The experimental realization of it uses a simple but novel method for applying a controlled-Z operation between the polarization of one photon and path of the other one. The goal of the experiment is to perform an experimental study of the properties of the *loop* graph, in addition to the study of the limitations today's technology applies to the realization of the theoretical methods that are proposed in this work.

1.4 Plan of Thesis

In chapter 2 of this thesis, the context in which the research reportd here is performed is clarified. In chapter 3 we study the photonic implementations of the one-way model and propose a scheme for the realization of this model in optical fibers, using time-bin

qubits. In chapter 4, the theoretical background and motivation for the creation of the loop graph is extensively clarified. Chapter 5 contains the experimental method and the simulations necessary to characterize the experimental errors. Chapter 6 contains the detailed characteristics of the experimental setup and the results. Chapter 7 concludes this work.

Chapter 2

Literature Review

After the proposal for the one-way model of quantum computation by Raussendorf and Briegel (Raussendorf et Briegel, 2001), (Raussendorf *et al.*, 2003), (Hein *et al.*, 2006), (Nielsen, 2006), as was discussed in the previous chapter, various research groups around the world have worked on the implementations of this model. Although there are various proposals and some experimental realizations of this model using optical lattices (Bloch, 2008), frequency combs (Menicucci *et al.*, 2008) and Nuclear Magnetic Resonance (NMR) (Ju *et al.*, 2010), the photonic systems so far have proven to be the more convenient to work with, as photonic entangled states are more robust against decoherence compared to other systems (Kok *et al.*, 2007), (Jennewein *et al.*, 2011).

The pioneering experiment using a photonic implementation of the one-way model was done by (Walther *et al.*, 2005). In this experiment, they made various 4-qubit cluster states, namely, a line cluster, a horse shoe cluster, and a square cluster and preformed a 2-qubit Grover's algorithm using the square cluster. Their 4-qubit graph state was created by combining two pairs of polarization entangled photons on polarization beam splitters and looking at 4-fold coincidences. The same group later reported the implementation of the full computation using active feed-forward. During this experiment, they applied corrections conditioned on the result of the measurement of the two qubits to the measurement basis of the third one and then applied conditional final corrections to the output qubit. The corrections were implemented by Electro-Optic Modulators (EOMs). They reported a total speed of less than 150 ns for each correction, which included the completion of the detection stage, logic operations to determine the correction to be applied, and the switching and charging process of the EOMs (Prevedel *et al.*, 2007). The experiment itself was performed in free space, however, two single mode optical fibers were used as delay lines for the two photons that were to receive the change of basis and corrections.

For the realization of a scalable one-way quantum computer, one requires such delay lines for almost all qubits, hence it is natural to think of an all-fiber optical implementation of this model. What remains to be decided upon is which degree of freedom (DOF) of photons is the most suitable for such implementation.

The smallest graph state is the 2-qubit state that is equivalent to an EPR pair up to a

local unitary transformation. In 2004, (Marcikic *et al.*, 2004) demonstrated the persistence of the entanglement of EPR pairs, implemented by the time-bin qubits, over 25 km of optical fiber, where time-bit qubits use the arrival time of photons as the degree of freedom that physically implements the logical qubits and are fully described in chapter 3. Moreover, Dür and Briegel have shown that the life-time of entanglement for the graph state does not depend on the size of the system (Dür et Briegel, 2004). Thus it is plausible to think that the graph states made from time-bins will retain their coherence in optical fibers long enough to allow for the realization of the one-way model of quantum computation. This prompted us to work on a method to manipulate time qubits and propose a scheme for the implementation of this model in optical fiber, using time-bin qubits. Our method is at present the only proposed method for this purpose and is described in chapter 3.

Recently, there is much effort and progress in integrated devices and waveguides, useful for quantum computing (Laing *et al.*, 2010), (Jeremy L. O'Brien, 2009). Our proposal for using time-bin qubits for the realization of the one-way quantum computer is also valid for these systems. In fact, one can combine the use of optical fibers as delay lines with these devices to keep the photons while the single qubit measurements and the feed-forward of the results are being performed.

The persistency of EPR entangled state realized by polarization qubits was demonstrated in 3 km of optical fibers (Catherine Holloway et Jennewein, 2011) and in 100 km of optical fiber when one photon travels through the fiber (Hübel *et al.*, 2007). However, as the optical fibers apply a random unitary operation on polarization qubits, it is not feasible to use this degree of freedom of photons for quantum computing in optical fibers and using time-bin is still the preferred way.

Different experimental groups in the world have implemented various graphs for the one-way model. Vallone *et al.* introduced the first experimental implementation of the cluster states using more than one degree of freedom of photons. Cluster states are graph states with specific shapes. These shapes are the line and tile. The tile corresponds to square shapes sitting adjacent to each other. This group collected photons from four different points of the cone of light coming out of a Spontaneous Parametric Down Conversion (SPDC) process that was used to created polarization entangled photons. Using the momentum correlations inherent to the SPDC process, they chose these four points in a way that would give rise to momentum entanglement for the pair of photons. Hence, the two photons would carry an EPR pair encoded on their polarization degree of freedom of photons and another EPR pair of qubits encoded on their momentum or path degree of freedom. Hence, 4 qubits are being carried on only 2 photons (Vallone *et al.*, 2007), (Vallone *et al.*, 2008c). This state where the photons are entangled to each other in more than one degree of freedom is called

a hyper-entangled state. Vallone *et al.*. then reported the implementation of a one-way computation with active feed-forward using the 4-qubit hyper-entangled state (Vallone *et al.*, 2008b). They also studied the characterization of hyper-entangled states using entanglement witness (Vallone *et al.*, 2008a) and later continued to create a 6-qubit hyper-entangled state that used the polarization DOF and two different momentum DOFs of two photons. They characterized this state using an entanglement witness they devised and performed a 3-qubit Deutsch-Jozsa algorithm (Vallone *et al.*, 2010b), (Vallone *et al.*, 2010a).

Meanwhile the group of Jian-Wei Pan have been increasing the number of photons for the graph states. In order to do so, they used various sets of non-linear crystals to create the photon pairs entangled in their polarization DOF. They then created the larger states by combining pairs of indistinguishable photons from different sets of crystals on polarization beam splitters (PBS) and created states of up to 6-qubits that are using only the polarization DOF (Lu *et al.*, 2007). This group also reported the demonstration of a 4-qubit hyper-entangled state of two photons that used polarization and momentum DOFs. Their work differed from that of Vallone *et al.* in the method they used to collect the photons to generate momentum entanglement. They used a double pass setup, in which the pump beam goes through non-linear crystals, and through SPDC, degenerate and non-collinear phase matching, creates photons that are emitted on a cone. Then the pump is reflected back and goes through the crystal again to create photons emitted into another cone on the other side of the crystal. Collecting photons from these two cones and combining one photon of each cone with a photon of the other cone on a beam splitter erases the information of which cone the photon is coming from and gives rise to entanglement in momentum in addition to polarization DOF (Chen *et al.*, 2007). Using multiple non-linear crystal setups and combining the photons created in each crystal setup with those created in other setups on polarization beam splitters and by further using PBSs to add the momentum DOF to each photon, this group succeeded in creating an 8-qubit state that included the polarization and momentum DOFs, which they used to perform topological error correction using cluster states (Gao *et al.*, 2009). The various entangled states created by the group of Jian-Wei Pan have essentially included the Greenberger-Horne-Zeilinger states and line graphs.

Recently, the group of Sang-Kyung Choix has reported the realization of a 7-qubit cluster state, using the polarization and spatial DOFs of four photons. They introduced an interesting method to combine the spatial DOFs of two photons on a polarization beam displacer (PBD) in a way that erases the information about which photon takes which path when they exit the PBD. The paths of two photons, each from a different 4-qubit, 2-photon line graph, get combined to result into a 7-qubit cluster (Lee *et al.*, 2011).

It is true that there is a lot of great work done for the photonic realization of cluster

states, but none of this work has focused on the creation of graphs, which are the general entangled resource for one-way quantum computing. Although entanglement has been done between different DOFs of the same photon, no experiment has reported on the entanglement between a DOF of one photon and a different DOF of another one. The experimental work reported in this thesis focuses on these aspects.

After the first proposal for the one-way model, Kashefi and her collaborators started working on the development of methods to enable the generalization of finding patterns that allow deterministic quantum computation by any graph state (Danos *et al.*, 2007). They developed an algorithm that determines which qubit should receive a correction after the measurement of previous qubits. The algorithm is said to find the *flow pattern* on the graph. This allows one to find a complete measurement pattern on the graph and consequently the multi-qubit unitary that is being implemented by the measurement pattern, which in turn determines its circuit equivalent (Danos et Kashefi, 2006). They later realized that the notion of the flow can be generalized, such that a set of qubits would receive the correction depending on the measurement result of a qubit, instead of having just one qubit receive this correction. The generalization of the notion of flow enables one to find the measurement pattern on a graph that is optimized in its depth complexity (Browne *et al.*, 2007). The concepts of flow and generalized flow, in addition to the proposed algorithms to find these patterns on a given graph are explained in detail in chapter 4.

An interesting finding of this work is that it is possible to have graphs that have no flow, but generalized flow. On these graphs, one cannot find a measurement pattern for deterministic quantum computing if one is allowed to apply correction on only one qubit after measuring another, but it is possible to find a measurement pattern when one allows a set of qubits to receive corrections from the measurement of one qubit. The smallest example of such graph is a 4-qubit graph with a loop structure shown in Fig. 4.4. Due to its loop structure, in addition to being the smallest graph that has a generalized flow and no flow, this graph has an intrinsic closed time-like loop associated with it.

Ernesto da Silva, Galvao and Kashefi have shown that the one-way model of QC applied to graph states can give rise to time-like loops that are equivalent to the model proposed by Bennett and Schumacher (Bennett et Schumacher, 2004), (Bennett et Schumacher, 2002), then independently by Svetlichny (Svetlichny, 2009), (Svetlichny, 2011), for the simulation of these loops, when the post-selection in this model has succeeded (Dias da Silva *et al.*, 2011). Closed time-like loops, the proposal of Benett, Schumacher and Svetlichny and the relation between the graph states with time-like loops are described in detail in chapter 4.

Due to such interesting theoretical properties, we decided to experimentally implement the 4-qubit loop graph. This is the first experiment that the simulates time-like loops without

the use of post-selection. Although, as described above, various graphs are implemented in photonic systems, in our experiment we propose a novel method using linear optical elements to entangle the polarization DOF of one photon to the path DOF of another photon. This is the property that is unique to our implementation and sets our experiment apart from others.

The work done in this thesis is in close collaboration with various colleagues. Through association with Felix Bussières I learned about time-bin qubits and we developed the gate that applies the arbitrary unitary transformation on a single time-bin qubit. I then worked on the application of these methods to the one-way model, which gave rise to the material covered in chapter 3.

The idea of the 4-qubit loop graph was developed in collaboration with Elham Kashefi. I designed the experiment and the method to create the loop structure. The experiment was then performed at the University of Toronto, in the group of Aephraim Steinberg, where we used the source of entangled photon pairs that Xingxing Xing, a Ph.D. student of Prof. Steinberg, had developed in collaboration with Morgan Mitchel's group in ICFO, Barcelona. The source was fully characterized as a source of single photons. However, after I arrived at the University of Toronto, we started the characterization of the source for polarization entangled photons and its optimization. The rest of the experimental setup and performance is mainly my work with help from Xingxing and discussions with other students in the lab.

Chapter 3

Photonic Implementations of the One-way Model of QC

Various physical systems can be used for implementing the one-way model of quantum computation. Among these, photonic systems have interesting advantages: the quantum states of photons are resilient to decoherence, single qubit gates are simple to implement and several techniques already exist for entangled photon pair generation.

In this chapter, three degrees of freedom (DOF) of photons, namely polarization, path and time-bin, are considered for encoding qubits for use in one-way quantum computation. For each DOF, it is shown how one would implement a one-way quantum computer. The three requirements for the realization of this computer are reviewed for each DOF: the generation of EPR pairs, which are entangled pairs of qubits in state $(|00\rangle + |11\rangle)/\sqrt{2}$, manipulation of single qubits and finally measurement. A method for creating graph states is also shown for each DOF. Finally, the merits of selecting one or several of these DOF is discussed. Two degrees of freedom will be chosen for encoding two qubits on a single photon, facilitating an experimental implementation of one-way QC.

3.1 Polarization Qubits

As an oscillating electromagnetic field, a photon has a polarization associated to it, which is the direction of oscillation of its electric field. This direction of oscillation can be written as the linear superposition of *horizontal* and *vertical* directions, in the form of the state, $\alpha|H\rangle + \beta|V\rangle$, normalized such that $|\alpha|^2 + |\beta|^2 = 1$. We assume the convention that $|H\rangle$ represents the logical $|0\rangle$ and $|V\rangle$ logical $|1\rangle$, so the polarization state of a photon will perfectly match the definition of a qubit.

To create a graph state, one can start by creating EPR states. There are two known ways to create these pairs. One is to use the process of spontaneous parametric down conversion, which is still the method most commonly used. The second method is to use bi-excitons in semiconductor devices. This method is highly promising for the realization of a photonic quantum computer, however, it is still in its infancy.

3.1.1 Spontaneous Parametric Down Conversion

When laser light travels through a crystal, the electromagnetic field interacts with the electric charge of the material and creates an electric dipole moment. The density of this induced dipole moment is referred to as the polarization of the material and, in general, is related to the electric field, $E(t)$, by

$$\vec{P} = \epsilon_0[\chi^{(1)} \cdot \vec{E} + \chi^{(2)} \vdots \vec{E} \cdot \vec{E} + \chi^{(3)} \vdots \vec{E} \cdot \vec{E} \cdot \vec{E} + \ldots], \tag{3.1}$$

where the vertical dots signify tensor operations, as χs are tensors. The nonlinear response of the material gives rise to very interesting quantum phenomenan. One of which, arising from the second order term, is called Spontaneous Parametric Down Conversion (SPDC). During this process, the interaction of the coherent laser field with the material gives rise to the special number state

$$\eta_0|0,0\rangle + \eta_1|1,1\rangle + \eta_2|2,2\rangle + \ldots \tag{3.2}$$

where the coefficients η_i are related to the strength of the laser field and the numbers in kets refer to the number of photons in each output mode. One can design the detection system of photons to be able to distinguish between the various detected number of photons. This allows one to select only the events that give rise to the detection of one photon at each output mode, or in other words, post-select on the number state $|1,1\rangle$, which guarantees having photon pairs, but in a non-deterministic fashion. It is non-deterministic because the success of the event is not determined till the very end, at the detection stage. Looking only at this post-selected state allows one to describe the phenomenon more simply as the annihilation of one *pump* photon, a photon from the ingoing laser beam, and the creation of two photons, named *signal* and *idler*, such that the energy and momentum are conserved. The conservation of momentum is called the phase matching condition. The following two equations are satisfied.

$$\hbar\omega_p = \hbar\omega_s + \hbar\omega_i \tag{3.3a}$$

$$\vec{k}_p = \vec{k}_s + \vec{k}_i \tag{3.3b}$$

where p stands for pump, s for signal and i for idler. Note that each $\vec{k}$ is a function of the frequency of its corresponding photon and the refractive index of the material. Hence, to achieve phase matching for a given pump frequency and desired signal and idler frequencies, $\vec{k}_p$ should have a definite angle with the optical axis of the crystal, called the phase matching angle. There are two types of phase matching, type I, where signal and idler have the same polarization, which is orthogonal to that of pump photon and, type II, where signal and idler

have orthogonal polarizations, so that one of them has the same polarization as the pump photon. Here we explain how to use phase matching type I as one example of how one creates EPR-type polarization pairs using SPDC (Kwiat *et al.*, 1999). In later chapters, we will see how phase matching type II can give rise to polarization entanglement.

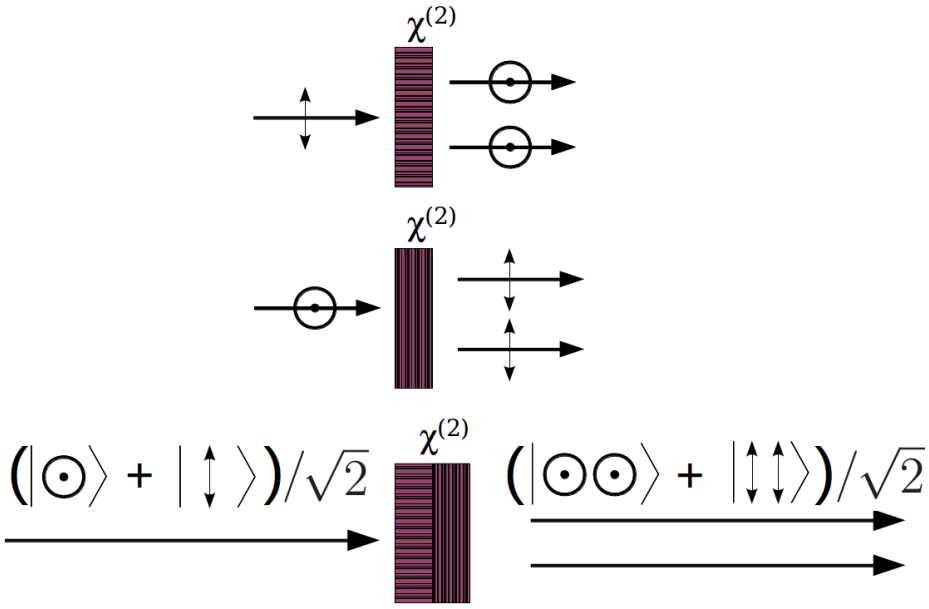

Figure 3.1 Using phase matching type I, 45°-polarized pump photons and two non-linear crystals with their optical axes at 90° orientation with respect to each other one can create EPR pairs in polarization.

Assume a vertically polarized pump photon hitting a crystal and creating horizontally polarized signal and idler photons such that they are degenerate in their energy, $\omega_s = \omega_i$, and all three k vectors are co-linear (Fig. 3.1). Now rotate this whole system by 90 degrees: one will have a horizontally polarized pump photon that creates vertically polarized signal and idler. Superposing these on each other results in a pair of crystals whose optical axes are oriented by 90 with respect to each other. One sends in a pump photon in state $(|H\rangle + |V\rangle)/\sqrt{2}$. The down conversion may occur in one of the crystals, but in principle it is not possible to distinguish in which one. So the signal and idler will be in state $(|HH\rangle + |VV\rangle)/\sqrt{2}$.

3.1.2 Bi-excitons in Solid State Devices

When a photon is absorbed by a semiconductor, an electron may gain enough energy to transfer to the conduction band and leave behind a hole. The electron and the hole attract each other with a Coulomb potential and form a quasi-atom, called an exciton. In

this process, the system evolves from the ground state to the exciton state. If two excitons are created, they can bind together and form a quasi-molecule, called the bi-exciton. If the physical system is such that it cannot distinguish which exciton was created first, then there are two different ways that the excitation process can happen, which is basically the order of birth of the two excitons. This is depicted as different exciton energy levels in Fig. 3.2. When the biexciton de-excites, two photons are created. There are two possible de-excitation paths, such that if the de-excitation happens through one path the emitted photons are in polarization state $|RL\rangle$, where R and L stand for *right-* and *left*-circular polarization, which are respectively $|H\rangle \pm i|V\rangle$. If the de-excitation happens through the other path, the emitted photons are in state $|LR\rangle$ (Fig. 3.3). Ensuring these two exciton energy levels are degenerate renders these two paths indistinguishable, hence the two emitted photons are in state $(|RL\rangle + |LR\rangle)/\sqrt{2} = (|HH\rangle + |VV\rangle)/\sqrt{2}$.

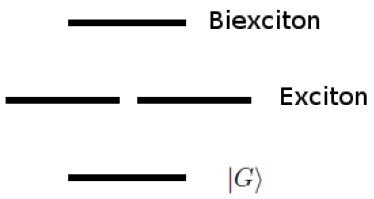

Figure 3.2 Coupled electron-hole pairs in semiconductors create a 2-level energy system with two different mid levels.

The main advantage of this method over SPDC is that it creates photon pairs in a deterministic fashion. Indeed, a beautiful work was recently reported by Sheilds, *et al.*, (Stevenson *et al.*, 2006) in which they use electric signals for the creation of bi-excitons and thus eliminate the contamination from pump photons. This method however is still very new and in development, hence is not yet used as widely by various research groups.

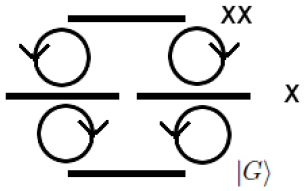

Figure 3.3 Two distinct but coherent decay modes of bi-excitons lead to EPR polarization pairs.

We will now explain how one can manipulate the polarization qubits and measure them.

3.1.3 Manipulation of Polarization Qubits

Polarization qubits can be rotated to any point on the Bloch sphere using birefringent materials. In these materials, the horizontal and vertical polarizations see different optical path lengths and, by the time they leave the material, one of the polarization orientations is retarded in phase relative to the other one, by some phase ϕ. A retarder is represented by the matrix

$$R_z(\phi) = \begin{pmatrix} 1 & 0 \\ 0 & e^{i\phi} \end{pmatrix},$$

Rotating the retarder, such that the angle between its optical axis and the polarization of in-going beam changes, allows one to rotate the in-going polarization to any point of a circle on the surface of the Bloch sphere (Collett, 2005). The general matrix for a rotated retarder with angle β and retardance ϕ is

$$\begin{pmatrix} \cos^2(\beta) + e^{i\phi}\sin^2(\beta) & \cos(\beta)\sin(\beta)(1 - e^{i\phi}) \\ \cos(\beta)\sin(\beta)(1 - e^{i\phi}) & \sin^2(\beta) + e^{i\phi}\cos^2(\beta) \end{pmatrix}.$$

The standard retardances used are $\pi/2$, realized by a quarter-wave plate (QWP) and π, by a half-wave plate (HWP). A sequence of QWP, HWP, QWP can rotate the initial qubit to any point on the Bloch sphere.

Wave plates are normally passive components. As we described in chapter one, in order to do computation, one should measure each qubit in bases $HR(\pm\phi)$, such that the sign of the angle ϕ depends on the results of previous measurements. Hence, an active component is required to apply the necessary change in the angle. One can use a Pockel cell or an Electro-Optic Modulator (EOM) to achieve this goal (Prevedel *et al.*, 2007). A Pockel cell is made of material whose birefringence depend on an applied electric voltage. By varying this voltage the retardance of the wave plate varies. This allows one to quickly set the device to be at $+\phi$ or $-\phi$. One can then use a passive HWP at 22.5° to apply the Hadamard operation and complete the setting of measurement.

3.1.4 Measurement of Polarization Qubits

To measure a polarization qubit one can use a polarization beam splitter cube (PBS) with a single photon detector at each of its output ports. The PBS transmits horizontal polarized photon and reflects vertical polarized photon. If a photon in state $\alpha|H\rangle + \beta|V\rangle$ arrives at a PBS, it is transmitted with probability $|\alpha|^2$ and reflected with probability $|\beta|^2$. If the photon is detected at the transmitted arm, one has measured logical value 0 and if the photon is detected in the reflected arm, one has measured logical value 1.

3.1.5 Graph State Creation

In 2004, Browne and Rudolph proposed a scalable scheme to *fuse* EPR pairs together and create a larger graph (Browne et Rudolph, 2005). They proposed two setups which they called *fusion gates I* and *II* (Fig. 3.4). For Fusion gates to work at all, the photons entering the gate should be indistinguishable in their frequency bandwidth and should arrive at the polarization beam splitter of the fusion gates at exactly the same time. As shown in

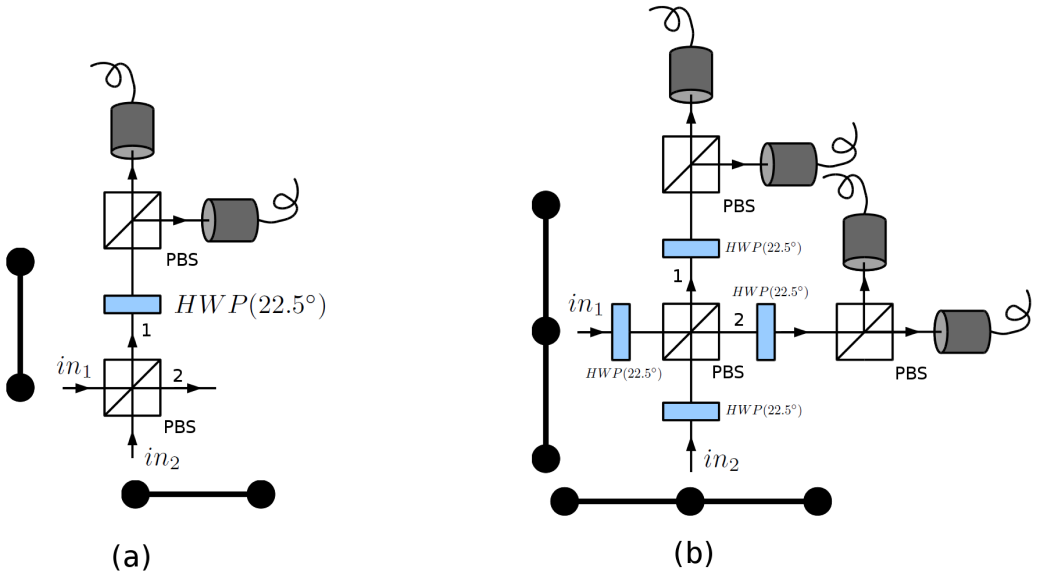

Figure 3.4 Fusion gates as proposed by Browne and Rudolph. (a) One photon from each EPR pair enters the gate from the two input ports. The fusion is successful when there is exactly one photon on path 1 and one photon on path 2. The output of the successful gate is a 3-qubit line graph. (b) Fusion gate II is used to fuse larger graphs together. It is successful when exactly one photon is detected on path 1 and one photon on path 2. In case of success, the 3-qubit graphs result into a 4-qubit graph. The success probabilities of both gates are 1/2.

Fig. 3.4(a), the fusion gate *I* consists of a PBS with a HWP set at 22.5° at one of its output ports. The photons going to this port then go through another PBS with a detector at each output. The other port of this PBS contains no other optical elements and allows a photon to exit the fusion gate and become a part of the graph state.

In order to create many-qubit graphs from polarization of photons, one starts by applying a Hadamard gate to two EPR pairs that are created using SPDC to make two 2-qubit graph states. One photon from each pair is sent through different input ports of the fusion gate,

labeled in_1 and in_2 in Fig. 3.4(a). The state of the photons after the PBS is

$$\frac{|HH_2\rangle + |HV_1\rangle + |VH_2\rangle - |VV_1\rangle}{2} \otimes \frac{|H_1H\rangle + |H_1V\rangle + |V_2H\rangle - |V_2V\rangle}{2}.$$

The subscripts for H and V are the paths taken by that photon. In the above notation, the photon that is sent to the gate from the first pair is placed as the second qubit in the ket. The photon from the second pair is placed as the first qubit in the ket. Note that the choice for the order of placing qubits in kets is arbitrary and one only needs to keep track of the order and keep it constant.

The gate is considered to be successful when only one photon is detected in path 1. In this case, the two smaller graphs fuse together and make a larger one. Success occurs only when both photons have the same polarization, therefore the gate's operation is, in fact, a parity check. When the gate is successful, which happens with probability 1/2, the state of the 4 photons after the PBS is

$$\begin{aligned}\frac{1}{2\sqrt{2}}(&|HH_2H_1H\rangle + |HH_2H_1V\rangle + |VH_2H_1H\rangle + |VH_2H_1V\rangle \\ &+|HV_1V_2H\rangle - |HV_1V_2V\rangle - |VV_1V_2H\rangle + |VV_1V_2V\rangle)\end{aligned}$$

The HWP at 22.5° then applies a Hadamard on the path 1 qubit. The state becomes

$$\begin{aligned}\frac{1}{4}(&|HH_2H_1H\rangle + |HH_2V_1H\rangle + |HH_2H_1V\rangle + |HH_2V_1V\rangle \\ &+|VH_2H_1H\rangle + |VH_2V_1H\rangle + |VH_2H_1V\rangle + |VH_2V_1V\rangle \\ &+|HH_1V_2H\rangle - |HV_1V_2H\rangle - |HH_1V_2V\rangle + |HV_1V_2V\rangle \\ &-|VH_1V_2H\rangle + |VV_1V_2H\rangle + |VH_1V_2V\rangle - |VV_1V_2V\rangle)\end{aligned}$$

If one measures H on path 1, the remaining state is

$$\frac{1}{2\sqrt{2}}(|HHH\rangle + |HHV\rangle + |VHH\rangle + |VHV\rangle + |HVH\rangle - |HVV\rangle - |VVH\rangle + |VVV\rangle)$$

which is the state of a 3-qubit line graph. If one measures V on path 1, the remaining state is

$$\frac{1}{2\sqrt{2}}(|HHH\rangle + |HHV\rangle + |VHH\rangle + |VHV\rangle - |HVH\rangle + |HVV\rangle + |VVH\rangle - |VVV\rangle)$$

which is equivalent to the previous result up to a σ_z correction on path 2, where

$$\sigma_z = \begin{pmatrix} 1 & 0 \\ 0 & -1 \end{pmatrix}.$$

Using this method, arbitrarily long line graphs can be created. When fusion gate I fails, its effect is to measure the two qubits in σ_z or computational basis. As the result of this measurement, any cZ connection with other qubits is severed. To overcome this problem, one can then use fusion gate II to fuse these line graphs together and create any desired graph state. Fusion gate II is similarly successful when there is only one photon on each path after the PBS, and this happens with probability 1/2. Note that in case of failure of this gate, no cZ connection is severed and instead some redundant encoding is created, hence the remaining graphs can be recycled. Another thing to keep in mind as a requirement for using these gates is that one requires some sort of storage for the photons while one is waiting to learn the result of each gate operation.

So far we have discussed all neccessary elements for the realization of a one-way quantum computer that uses only polarization of photons as qubits. We will now explain how one can use path qubits as the means to achieve the same goal.

3.2 Path Qubits

Path degree of freedom is literally the travelling path of a photon. One can create conditions such that the photon will be in a superposition of two different paths. We choose one of these paths to represent the logical 0 and the other one the logical 1, so that the path state of the photon will be $\alpha|0\rangle + \beta|1\rangle$. Since the photon is guaranteed to be in one of these paths, the probability of detecting it in one or the other is 1, which means $|\alpha|^2 + |\beta|^2 = 1$, and one can use the path DOF as a qubit.

3.2.1 Creation of Entangled Path Qubits

One can create entangled path qubits in two different ways. One is to take advantage of the momentum conservation in SPDC (Vallone *et al.*, 2007). As mentioned before, the momenta $\vec{k}$ of the signal and idler photons should add up to that of the pump photon. It is possible to design the phase matching to be non-colinear such that both $\vec{k}_s$ and $\vec{k}_i$ make the same angle with $\vec{k}_p$ (Fig. 3.5(a)). The system is 3-dimensional, however, so the signal and idler photons come out of the crystal in a cone such that the photons emitted at the opposite sides of the cone are correlated in their $\vec{k}$ vectors. One then collects the pair of photons

from four points of the cone, situated opposite to each other, which we label a_1, a_2 and b_1, b_2 (Fig. 3.5(b)). The pair of photons is either coming from the a_1, a_2 points, corresponding to state $|aa\rangle$ or from the b_1, b_2 points, corresponding to state $|bb\rangle$. Ensuring the signal and idler are indistinguishable in all other DOFs results in a coherent superposition of these two possibilities $(|aa\rangle + |bb\rangle)/\sqrt{2}$. We take a to represent logical 0 and b, logical 1.

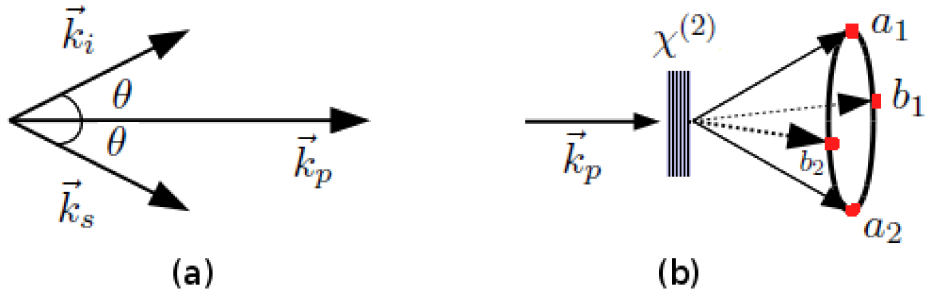

Figure 3.5 Creation of EPR pairs in path DOF. (a) In SPDC, One can design the system so that the phase matching is not colinear, but $|\vec{k}_s| = |\vec{k}_i|$. (b) Photon pairs exit the down-converting crystal in a cone. Collecting the photon pairs from four carefully selected points gives an EPR pair in path qubits.

A second way to create path entangled qubits is to start from a polarization EPR pair $|HH\rangle + |VV\rangle)/\sqrt{2}$. Then one sends each photon to a PBS (Fig. 3.6(a)). We label the transmission ports by a and the reflection ports by b. If both photons are horizontally polarized, they will both transmit into ports a and if they are both vertically polarized, they will both reflect into ports b. So state $|HH\rangle + |VV\rangle)/\sqrt{2}$ becomes $|aa\rangle + |bb\rangle)/\sqrt{2}$. In this section we take any path labeled a to represent the logical 0 and any path labeled b represent logical 1.

One should mention that some research groups have used this method to create the so called hybrid-entangled GHZ states (Gao *et al.*, 2009), since one can also write out the state of the photons after the PBSs to be $|aaHH\rangle + |bbVV\rangle)/\sqrt{2}$. A GHZ state is, in general, a superposition of two kets where each contains only logical values 0 or 1. The state of the photons is said to be hybrid-entangled because it involves entanglement of more than one degree of freedom of photons.

Using this method, the polarization entangled qubits produced from bi-exciton systems can be converted to path qubits. PBSs can also convert path qubits to polarization qubits. One flips the polarization of one path with a $HWP(22.5°)$ and combines both paths on a PBS as shown in Fig. 3.6(b).

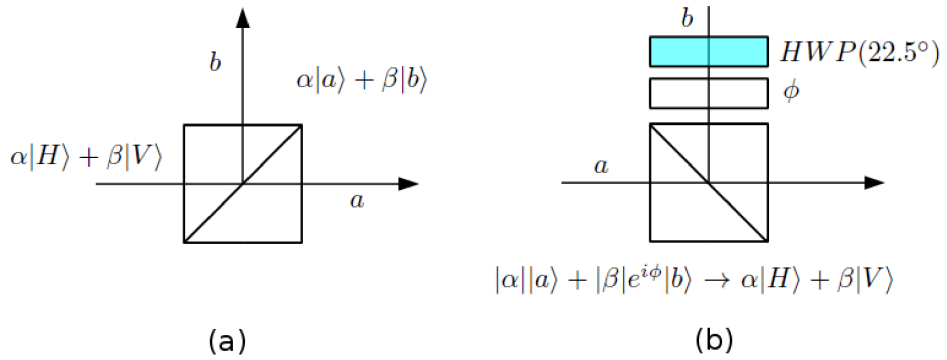

Figure 3.6 (a) Polarization to path conversion: A polarization encoded photon enters a PBS, at output ports its polarization state changes to path encoding. (b) Path to polarization conversion: assume both paths before the PBS carry photons that are horizontally polarized. A $HWP(22.5°)$ flips the polarization of the photon in one arm to vertical. The phase relation between the two paths is set by ϕ. Paths a and b ending at PBS should be balanced. Output qubit from PBS is polarization encoded.

3.2.2 Manipulation and Measurement of Path Qubits

A major optical tool for manipulation of path qubits is a 50 : 50 beam splitter (BS). When a beam of light arrives at a BS, half of its energy gets transmitted and the other half gets reflected. A photon, by its definition, is the smallest unit of energy and cannot be divided into smaller units. When a photon arrives at a BS, it either gets transmitted or reflected with equal probability. The equations governing this behavior are (Gerry et Knight, 2004)

$$\hat{a}_0^\dagger = (\hat{a}_1^\dagger + \hat{b}_1^\dagger)/\sqrt{2}$$

$$\hat{b}_0^\dagger = (\hat{a}_1^\dagger - \hat{b}_1^\dagger)/\sqrt{2},$$

where $\hat{a}^\dagger$ and $\hat{b}^\dagger$ are creation operators that add one photon to the field, such that $\hat{a}^\dagger|n\rangle = \sqrt{n+1}|n+1\rangle$ and $|n\rangle$ represents a state that has n photons in it. The subscripts for these operators correspond to input and output ports of the BS (Fig. 3.7).

Note that the notation for number states $|0\rangle$ and $|1\rangle$, which signify the existence of no photons and only one photon, is an unfortunate coincidence with that of quantum logical 0 and 1. To prevent any confusion for these notations, we use in this section the notation $|a\rangle$ and $|b\rangle$ to respectively represent the logical 0 and 1. The subscripts in this notation clarify which path is referred to. Hence, in this section, we reserve the notations $|0\rangle$ and $|1\rangle$ for number states.

If a qubit is in a path state $\alpha|a_0\rangle + \beta|b_0\rangle$, a Hadamard operation should take it to state

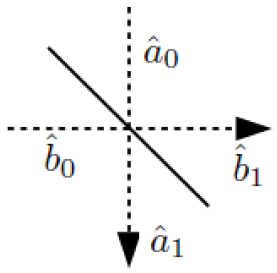

Figure 3.7 A 50 : 50 beam splitter with its associated creation operators.

$(\frac{\alpha+\beta}{\sqrt{2}})|a_1\rangle + (\frac{\alpha-\beta}{\sqrt{2}})|b_1\rangle$, where a_0 and a_1 represent logical qubit 0 and b_0 and b_1 represent logical qubit 1. One can easily see that the effect of a beam splitter on a photon is the same as the Hadamard. We assume the photon is entering the beam splitter from port $\hat{a}_0$. This corresponds to having one photon in this port, shown by the ket $|1\rangle_{a0}$ and having zero photons in port $\hat{b}_0$, shown by the ket $|0\rangle_{b0}$ in the following calculation.

$$\begin{aligned} |a_0\rangle = |1\rangle_{a0}|0\rangle_{b0} = \hat{a}_0|0\rangle_{a0}|0\rangle_{b0} \quad &\rightarrow \quad \frac{\hat{a}_1^\dagger + \hat{b}_1^\dagger}{\sqrt{2}}|0\rangle|0\rangle) \\ &= \quad ((|1\rangle_{a_1}|0\rangle_{b_1} + |0\rangle_{a_1}|1\rangle_{b_1})/\sqrt{2}) \\ &= \quad (|a_1\rangle + |b_1\rangle)/\sqrt{2} \end{aligned}$$

and

$$\begin{aligned} |b_0\rangle = |0\rangle_{a0}|1\rangle_{b0} \quad &\rightarrow \quad (\frac{\hat{a}_1^\dagger - \hat{b}_1^\dagger}{\sqrt{2}})|0\rangle|0\rangle \\ &= \quad (|1\rangle_{a_1}|0\rangle_{b_1} - |0\rangle_{a_1}|1\rangle_{b_1})/\sqrt{2} \\ &= \quad (|a_1\rangle - |b_1\rangle)/\sqrt{2}. \end{aligned}$$

The linear combination of the two, with coefficients α and β, gives

$$\frac{\alpha(|a_1\rangle + |b_1\rangle) + \beta(|a_1\rangle - |b_1\rangle)}{\sqrt{2}} = \frac{\alpha+\beta}{\sqrt{2}}|a_1\rangle + \frac{\alpha-\beta}{\sqrt{2}}|b_1\rangle$$

In order to perform any unitary operation on path qubits, one should be able to change $|\alpha|$ and $|\beta|$ by any desired amount. This change can be done by an interferometer (Fig. 3.8).

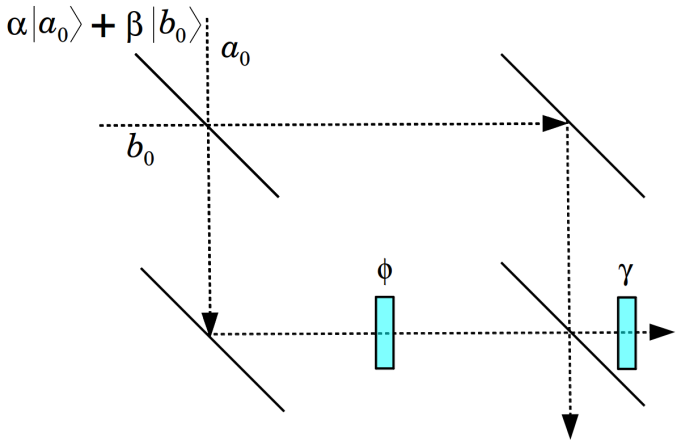

Figure 3.8 A variable beam splitter: by changing the phase ϕ of an interferometer, one can set the real part of the probability amplitudes at output ports to any desired value.

The action of the interferometer on the qubit is (Nielsen et Chuang, 2000)

$$\frac{1}{2}\begin{pmatrix} 1 & 1 \\ 1 & -1 \end{pmatrix}\begin{pmatrix} 1 & 0 \\ 0 & e^{i\phi} \end{pmatrix}\begin{pmatrix} 1 & -1 \\ 1 & 1 \end{pmatrix} = \begin{pmatrix} 1+e^{i\phi} & -1+e^{i\phi} \\ 1-e^{i\phi} & 1+e^{i\phi} \end{pmatrix}$$
$$= \begin{pmatrix} \cos(\phi/2) & -\sin(\phi/2) \\ \sin(\phi/2) & \cos(\phi/2) \end{pmatrix}.$$

In order to change the phase between paths, one adds an extra phase γ to the output arm that is representing logical 1. To measure the path qubit in bases $HR_z(\theta)$, one adds an extra optical path length corresponding to phase shift θ on path b, then one closes the paths on a beam splitter to apply a Hadamard (Fig.3.9). One can talk about the phase difference between two paths only when one brings these two paths together on a beam splitter. Hence, in practice, one combines phases γ and θ and incorporates them in the interferometer which is closed by the final Beam Splitter that is applying the Hadamard.

3.2.3 Creating Graph States using Path Qubits

In order to fuse the path qubits together to make a graph state, one should perform a parity check on the path state of photons. Fig. 3.10 shows fusion gates I and II for path qubits with the same success probability as the one of polarization. To see how this gate works, let's look at what happens when two photons arrive simultaneously at the beam splitter of fusion gate I, from ports b_1 and a_2. Without any photons, the state at all ports of the BS is

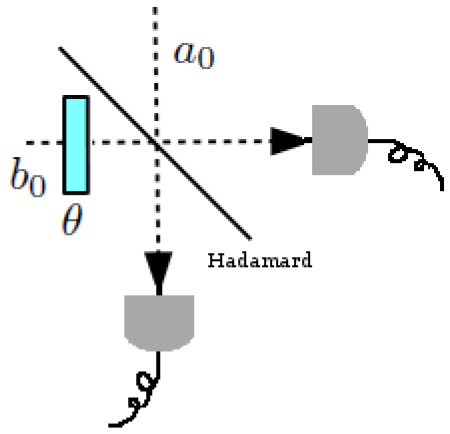

Figure 3.9 To measure a path qubit one needs to balance and close both paths in a beam splitter. Phase θ is the measurement angle of $HR_z(\theta)$ and is determined by the one-way computation.

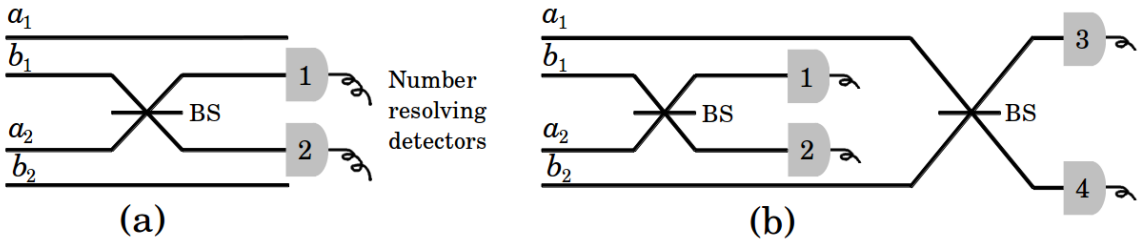

Figure 3.10 (a) Path fusion gate I: the beam splitter acts both as the PBS and the $HWP(22.5°)$. Gate is successful when one of the detectors detects only one photon. (b) Path fusion gate II: Gate is successful when detectors 1 and 2 collectively detect only one photon and detectors 3 and 4 detect the other one. The success probability for each gate is 1/2.

$|n\rangle = |0\rangle$, corresponding to vacuum. We have

$$\begin{aligned} |1\rangle_{b_1}|1\rangle_{a_2} &= \hat{a}^\dagger_{b_1}\hat{a}^\dagger_{a_2}|0\rangle_{b_1}|0\rangle_{a_2} \\ &\rightarrow \left(\frac{\hat{a}^\dagger_1 + i\hat{a}^\dagger_2}{\sqrt{2}}\right)\left(\frac{i\hat{a}^\dagger_1 + \hat{a}^\dagger_2}{\sqrt{2}}\right)|0\rangle_1|0\rangle_2 \\ &= \frac{i}{2}(\hat{a}^\dagger_1\hat{a}^\dagger_1 + \hat{a}^\dagger_2\hat{a}^\dagger_2)|0\rangle_1|0\rangle_2 \\ &= \frac{i}{\sqrt{2}}(|2\rangle_1|0\rangle_2 + |0\rangle_1|2\rangle_2). \end{aligned}$$

This means the two photons arriving at a beam splitter together from two different ports

exit it from the same port. So one of the number resolving detectors, 1 or 2, will detect two photons. This signals a failure for the fusion gate, as it signifies the photons having been in different logical modes a and b instead of both being in a or both in b. The gate is successful when one of the detectors detects only one photon. In this case, it is not clear if the detected photon was originally on path b_1 or a_2, hence no rotation equivalent to the action of a HWP is required. This is because the beam splitter alone acts as the PBS and this rotation at the same time.

Similarly, fusion gate II is constructed by closing the other two paths on a beam splitter (Fig. 3.10(b)). The gate is successful only when detectors 1 and 2 detect only one photons and detectors 3 and 4 detect the other photon.

Working with path qubits in practice requires interferometric stability. Recent advancements in the integrated wave-guide structure make this task easier and the wide usage of path qubits more promising.

In chapter 5 of this thesis, we show in detail, how one can realize path qubits in free space and perform single qubit operations and measurements on them.

3.3 Time-bin Qubits

In this section, we propose the realization of one-way quantum computing in optical fibre such that each photon is transmitted in its own fibre. The qubits are encoded using time-bin encoding (Brendel *et al.*, 1999). In this encoding, we divide the time line of the arrival of photons at detectors into a sequence of time slots, or bins, with alternating logical values (Fig. 3.11). The bins are labeled $|0\rangle = |s\rangle$ and $|1\rangle = |l\rangle$, where $s =$ short and $l =$ long.

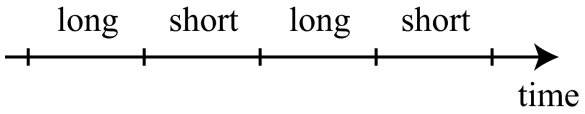

Figure 3.11 In time-bin encoding, the time of arrival of photons at the detector is divided to alternate between states $|s\rangle$ and $|l\rangle$.

Time-bin entanglement is experimentally proven to be robust against decoherence after transmission over more than 25 km of fibre (Marcikic *et al.*, 2004) which corresponds to a propagation time of the order of 10^{-4} seconds. On the other hand, it is shown that the decoherence rate of graph type entanglement does not depend on the size of the system (Dür et Briegel, 2004). This shows that, in principle, it is possible for a graph of entangled photons to keep its full entanglement in optical fibres long enough to allow the preparation of the

graph and the completion of the computation, including the feedforward of measurement results and setting the new measurement bases. By using electronic devices with 100 MHz bandwidth, these operations can be performed in the order of tens of nanoseconds.

In this section, fibre optical circuits for the production of graph states and their processing in the fully time-bin encoding scheme are presented. An alternative scheme, using a combination of time-bin and polarization encoding, is also presented. We finally briefly discuss experimental aspects of the proposed schemes.

3.3.1 Production of EPR pairs and processing

One can create an arbitrary $\alpha|s\rangle + \beta|l\rangle$ state by splitting a single-photon light pulse through a delay-line interferometer with adjustable splitting ratio and phase between the short and long delay lines. A 2-qubit graph can be generated by preparing a high-power optical light pulse in the state $(|s\rangle + |l\rangle)/\sqrt{2}$ and sending it through a parametric down-converter, resulting in an entangled photon pair in the state $(|ss\rangle + |ll\rangle)/\sqrt{2}$.

3.3.2 Processing in the fully time-bin based scheme

Our proposed reconfigurable gate shown in Fig. 3.12 applies a general single qubit operation to a time-bin encoded qubit (Soudagar *et al.*, 2007). One can adapt this general gate

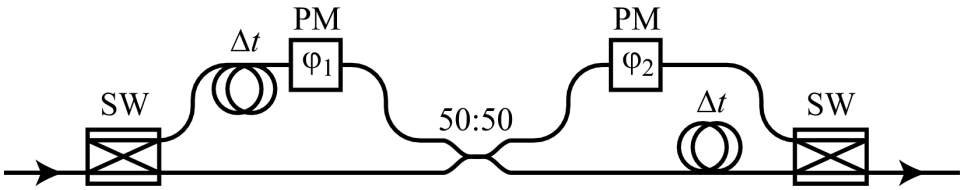

Figure 3.12 Reconfigurable time-bin one-qubit gate. SW: active switch; PM: phase modulator. This gate applies an $R_t(45^\circ)$ transformation to single qubits by setting φ_1 and φ_2 to appropriate values. The choice of $\phi_1 = 0$ and $\phi_2 = \pi$ applies a Hadamard transformation.

to any desired one by the appropriate choice of ϕ_1 and ϕ_2. To see how this gate works, one sends a photon in state $\alpha|s\rangle + \beta|l\rangle$ to the input rail of the gate. The first optical switch sends the state $|s\rangle$ to the upper (long) rail and the state $|l\rangle$ to the lower (short) one. The two states are synchronized before the $50:50$ beam splitter, while the one on the upper rail acquires an additional phase. The two states interfere at the beam splitter. Then the one on the upper rail experiences a phase shift and a delay to put the states back to different time-bins, before they are all transfered to the lower rail by the last switch.

A Hadamard can be done by choosing $\phi_1 = 0$ and $\phi_2 = \pi$. To perform the measurements required for one-way computation, one needs an $R_z(\pm\theta)$ followed by a Hadamard gate to the qubit before detection in the computational basis. For time-bin encoding, $R_z(\pm\theta)$ is performed with a time-varying phase modulator, which applies a phase $-\theta/2$ to state $|s\rangle$ and phase $\theta/2$ to state $|l\rangle$. Fig. 3.13 depicts the measurement scheme. To perform full

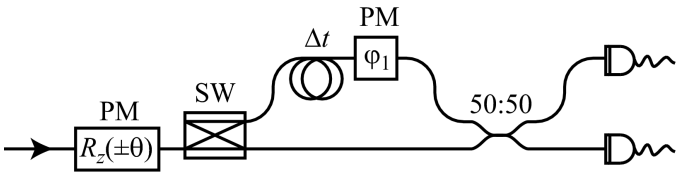

Figure 3.13 Detection in a desired basis using the time-bin scheme. The variable phase modulator before the first switch applies $R_z(\pm\theta)$, where the sign is determined according to the results of the previous sets of measurements. The rest of the circuit enables measurement in the Hadamard basis, and is based on the reconfigurable gate of Fig. 3.12 with the proper fixed φ_1.

computation, one has to wait for the results of the previous measurements to be fed-forward to the phase modulator to set the correct value of the angle $\pm\theta$. While this is happening, the graph of time-bin entangled photons are kept in optical fibre loops.

After all the processing is done, depending on the measurement results, one might need to apply single qubit corrections to the output. These corrections are only of two different kinds. One is a bit flip, which changes $|s\rangle$ to $|l\rangle$ and $|l\rangle$ to $|s\rangle$ and can be achieved using the circuit shown in Fig. 3.14a. The second one is a phase flip, which changes the $|1\rangle$ state to $-|1\rangle$ and leaves the $|0\rangle$ state unchanged. This can be achieved with a phase modulator as shown in Fig. 3.14b.

3.3.3 Graph production using the time-bin based scheme

In this section, we show the time-bin equivalent gate to the polarization fusion gate. The equivalent of the PBS for time-bin encoded qubits is an active, *e.g.*, electro-optic, switch. The switch has two inputs and can be set, at any given time, such that either both inputs continue on their original rail or they switch rails. Hence one can set it to allow qubits in the time slots corresponding to the short bin $|s\rangle$ to continue on their original rail, and those in the long time-bin $|l\rangle$ to switch rails.

Although $R(45^\circ)$ is very easy to implement for polarization encoding, its counterpart for

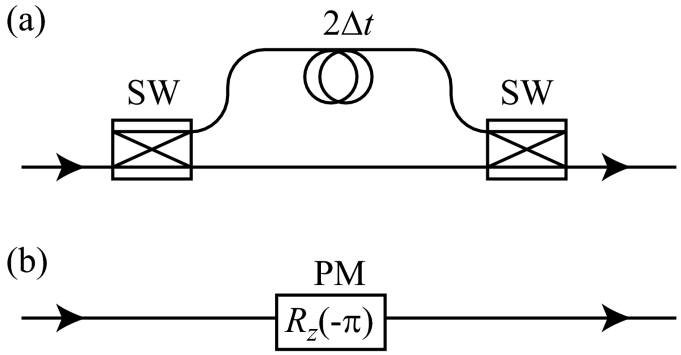

Figure 3.14 Circuits suitable for the 1-qubit corrections to the remaining qubits of the cluster. (a) Bit flip operation for time-bin qubits. The $|s\rangle$ state is delayed by $2\Delta t$, i.e. twice the delay between short and long bins. (b) Phase flip operation is equivalent to $R_z(-\pi)$ up to a global phase. It applies a π phase shift difference to $|s\rangle$ and $|l\rangle$.

time-bin encoding is not as simple. The $R(45°)$ gate applies the transformation

$$|0\rangle \to \frac{|0\rangle + |1\rangle}{\sqrt{2}}, \quad |1\rangle \to \frac{-|0\rangle + |1\rangle}{\sqrt{2}}$$

therefore

$$\frac{|0\rangle + |1\rangle}{\sqrt{2}} \to |1\rangle, \quad \frac{|0\rangle - |1\rangle}{\sqrt{2}} \to |0\rangle.$$

This transformation in a time-bin encoding can be done by choosing $\phi_1 = \phi_2 = \pi$ in the general gate of Fig. 3.12. We denote this adapted gate for time-bin as $R_t(45°)$.

Fig. 3.15 shows the complete fusion gate type I for time-bin encoding. One can show that the last switch and detector of the $R_t(45°)$ gate can be substituted by two detectors on each rail. This fusion gate succeeds if exactly one photon is detected. The probability of success of the gate is 1/2.

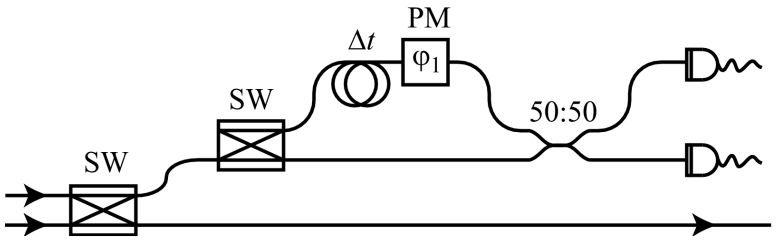

Figure 3.15 Fusion gate type I for time-bin encoded qubits. Fusion is successful if only one of the detectors detects exactly one photon.

The reconfigurable single qubit gate discussed above can be used for the implementation

of a fusion gate type II as shown in Fig. 3.16. Four $R_t(45°)$ gates are used before and after the optical switch that acts as the PBS. The gate is successful when both detectors fire and, as mentioned in Ref. (Browne et Rudolph, 2005), there is no need for photon counting detectors. This gate is successful with probability 1/2.

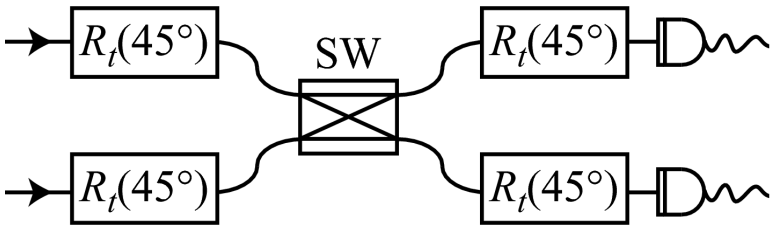

Figure 3.16 Fusion gate type II for time-bin encoded qubits. $R_t(45°)$ is the gate depicted in Fig. 3.12. Fusion is successful if both detectors fire.

3.3.4 Graph production using the polarization based scheme

Another way to implement fusion gates for time-bin encoding is to first convert the states of each photon from time-bin encoding to polarization encoding. In other words, one converts the state $|s\rangle$ to $|H\rangle$ and $|l\rangle$ to $|V\rangle$ with the circuit depicted in Fig. 3.17a. One can then use the polarization fusion gates to fuse time-bin graphs together. The fusion gate type I depicted in Fig. 3.18a requires a polarization beam splitter/combiner. A polarization controller is placed after one output to rotate the polarization by 45° before the polarization discriminating photon counting detection. The other output goes through the fibre optical circuit that converts the polarization state back to time-bin, namely $|H\rangle$ to $|s\rangle$ and $|V\rangle$ to $|l\rangle$, depicted in Fig. 3.17b. Fusion gate type II is similar to type I, except that it requires three more polarization controllers. Also, one does not require to convert the qubits back to time-bin encoding before detection. The setup is shown in Fig. 3.18b.

3.3.5 Processing in the polarization based scheme

In the processing stage, to carry on the measurement in any desired bases, one converts the time-bin qubits to be measured to polarization qubits and, using the usual devices for polarization manipulation, one applies the required rotation before detection. Fig. 3.19 shows the proper setup to achieve this goal. The eventual single qubit corrections to the output, a bit-flip and phase-flip, can be applied using waveplates.

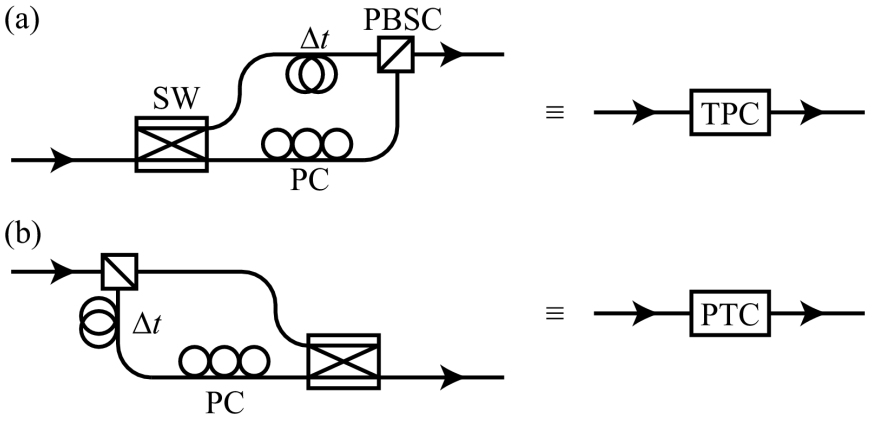

Figure 3.17 Encoding converters: PC is a polarization controller and PBS is a polarization beam splitter/combiner. The labels TPC and PTC stand for time-bin to polarization converter and polarization to time-bin converter. (a) This setup converts time-bin encoding to polarization encoding. One can set the switch and the polarization controller such that state $|s\rangle$ is converted to $|H\rangle$ and state $|l\rangle$ to $|V\rangle$. (b) Using this setup, polarization encoding is converted to time-bin encoding.

3.3.6 Discussion

The proposed experimental setups can be implemented using currently available optical technology. All-fibre components, such as couplers (the equivalent of beam splitters) and polarization controllers have very low insertion loss. Fiber-pigtailed bulk components, such as polarization beam splitter/combiners, also have low optical loss. Active electro-optic components, such as the switches and phase modulators, are readily available with high bandwidths of 10 GHz or more, allowing for sub-100 ps switching. Such active components currently impose significant excess loss of the order of 30–60%. The amount of photon loss through several electro-optic devices limits the proposed schemes to small graphs. However, it is worth mentioning that the optical losses of current electro-optic components constitute a purely technological problem which can be expected to be mitigated over the next few years, as typically happens with standard optical telecommunication devices.

The delay introduced to distinguish between the two times, short and long, needs to be longer than coherence length of the photons. In practice, however, this delay is determined by the time-jitter of the detectors.

One difficulty in the realization of this scheme is the phase stabilization required by the interferometers. We believe this is the main reason this method is not yet implemented for the propose of quantum computing. With the new progress made in integrated waveguides, however, one can imagine a combination of the use of optical fibers whenever a delay line is required with the interferometers written in waveguides, which are passively stable for up to

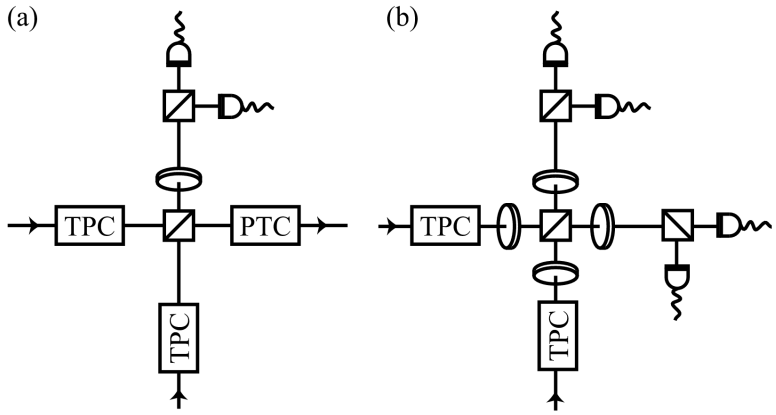

Figure 3.18 (a) Fusion gate type I. Time-bin encoded qubits are converted to polarization encoding before they go through the gate. The output is converted back to time-bin encoding. The gate is successful, with probability 1/2, when one of the detectors detects one photon. (b) Fusion gate type II: This gate is successful, with probability 1/2, when one detector fires after each PBS.

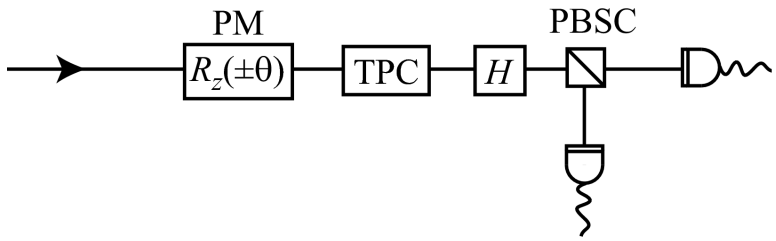

Figure 3.19 Detection in a desired basis using the polarization based scheme. A Hadamard gate is applied in polarization encoding by using a half-wave plate.

a few hours (Jeremy L. O'Brien, 2009). Hence, the state of the technology is growing and reaching a level that the implementation of this scheme can become a reality.

The three DOFs of photons discussed in this chapter are the most readily available and convenient for the realization of a photonic quantum computer. In this chapter, all the neccessary gates and elements for the realization of a one-way quantum computer using each of these DOFs were thoroughly discussed and clarified.

Due to the difficulties in creating polarization entangled photon pairs, it is desirable to increase the available number of qubits per photon by using more than one DOF for the physical implementation of the logical 0 and 1. Also, performing two qubit operations between different DOFs on the same photon are much easier than performing them among the DOFs of different photons. For these reasons, we have chosen the polarization and path DOFs of two photons for the experimental implementation of a 4-qubit graph state. The theoretical background for this proposed graph is explained in the next chapter.

Chapter 4

Theoretical Background for the Loop Graph

This chapter introduces the theoretical background necessary for understanding the motivation for the experimental realization of the 4-qubit loop graph. Note that the purpose of this theoretical background is only to provide a general understanding of the key concepts and not to provide a precise mathematical understanding of them.

This section addresses the following questions: Given a graph, how does one find out the computation pattern? Or equivalenly, how does one know which qubits to measure and to which qubits apply corrections? Furthermore, if one finds a computation pattern, what is the computation that is being done? Or equivalently, how does one find the circuit equivalent of a computation pattern?

In order to understand the answer to all these questions, we need to understand the concept of *stabilizers*. Using stabilizers, we show how one can find which qubits to measure first and which qubits receive information or flow from the measured qubits. Qubits that receive flow are the ones that need to be corrected. A precise description of the concept of flow and its generalized form is provided. It is demonstrated how the 4-qubit loop graph, with a particular choice of inputs, is the smallest graph that has a generalized flow and no flow.

The last section discusses a very interesting side effect of the one-way model of quantum computation, we will explain how this model gives rise to closed time-like curves and how this concept relates to our 4-qubit loop graph.

4.1 Pauli Operators as Graph Stabilizers

Pauli operators are the set of matrices $\{I, \sigma_x, \sigma_y, \sigma_z\}$, where I is the identity matrix and

$$\sigma_x = \begin{pmatrix} 0 & 1 \\ 1 & 0 \end{pmatrix}, \sigma_y = \begin{pmatrix} 0 & -i \\ i & 0 \end{pmatrix}, \sigma_z = \begin{pmatrix} 1 & 0 \\ 0 & -1 \end{pmatrix}.$$

In a graph, the set of vertices $\{k\}$ that are connected by a controlled-Z to a vertex i is said to be the *neighbourhood* of i and is denoted by $N(i)$. When the state of a graph, $|G\rangle$, is acted upon by the set of operators in the form $\sigma_x^i \otimes \sigma_z^k$, for all $k \in N(i)$, the remaining state is still the same graph, with a possible global phase change, $\pm|G\rangle$. If one applies σ_x on qubit i and σ_z to all qubits that are connected to i by a controlled-Z, the graph does not change. Mathematically speaking,

$$\hat{S} = \sigma_x^i \otimes_{k \in N(i)} \sigma_z^k |G\rangle = \pm|G\rangle$$

and the state $|G\rangle$ is the eigenstate of the operator $\hat{S}$ with eigenvalues ± 1. We say this special combination of the Pauli operators is the *stabilizer* of graph states (Hein *et al.*, 2006). The stabilizer of the graph state is the main concept that allows one to figure out if a graph, with certain sets of its qubits as inputs and outputs, can perform a deterministic computation and, if it can, what that computation is.

4.2 Deterministic Computation by a Graph: Concepts of *Flow* and *Generalized Flow*

A graph suitable for quantum computing consists of some qubits that are considered the inputs. These qubits are generally in states of the form $\alpha|0\rangle + \beta|1\rangle$, which includes $|+\rangle$ as one of its many possiblities. Some qubits are the output, which means they will not be measured. The rest of the qubits in the graph are auxilary qubits and help with processing by being measured.

Given a graph, one knows which qubits are the inputs, since input qubits can be in any arbitrary state $|\psi\rangle$ and not just in state $|+\rangle$. Once one determines which ones are going to be the outputs, one has introduced enough constraints to search for the computation that can be done using this graph, if any (Danos et Kashefi, 2006). For example, in the graph of Fig. 4.1, qubits 1 and 2 are inputs in some arbitrary states $|\psi_1\rangle$ and $|\psi_2\rangle$. We choose qubits 5, 6 and 7 to be the outputs. This should allow us to search for a pattern of qubit measurements and subsequent corrections that allowing a deterministic computation. To better understand what is meant by this sentence, take into account the fact that after measuring each qubit, there are two possible outcomes, 0 or 1. Say we measure qubit 1 of this graph of Fig. 4.1. If the answer is 0, some information is transfered to another qubit and if it is 1, some other information is transfered to this other qubit. Now this qubit is measured and the result is either 0 or 1, and depending on this result some information is transfered to another qubit. This continues until we measure the last qubit. At the end, we have many different possiblities about what information has traveled through the graph, which can be shown by a tree as

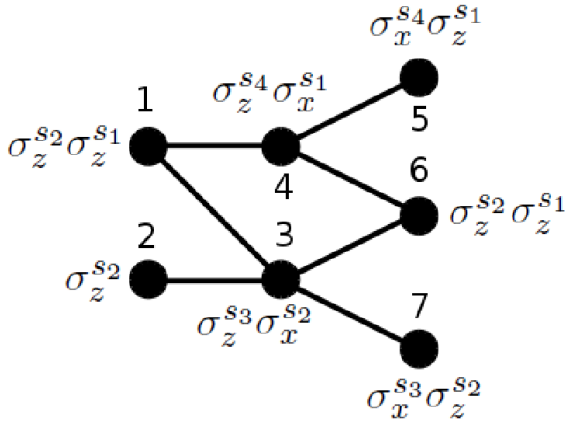

Figure 4.1 An example to show how to find a flow on a graph. Qubits 1 and 2 are inputs, which means they are in some arbitrary state $|\phi_1\rangle$ and $|\phi_1\rangle$. Qubits 5, 6 and 7 are the outputs. One measures all qubits except the output qubits. The application of subsequent stabilizers, as shown, allows for finding a flow on the graph, which in turn corresponds to finding a computation that one can perform using this graph with these given inputs and outputs.

depicted in Fig. 4.2. To guarantee a deterministic computation, one should make sure to stay

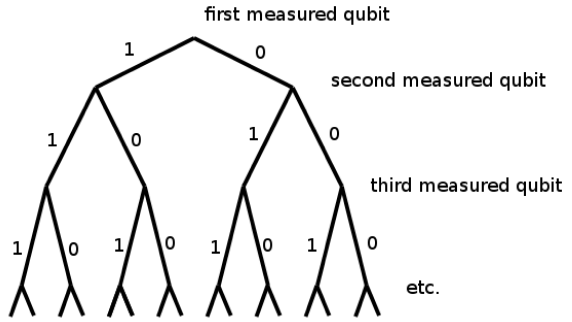

Figure 4.2 Each measurement can result into either 0 or 1. For each result different information is transfered to another qubit in the graph, hence each measurement result gives a different possible computation. In order to assure a deterministic computation, one should make sure one is always following only the branch that corresponds to measurement results all being 0.

on only one branch of the tree. It is convenient to choose the branch where all measurement results are 0. This is done adjusting the measurement bases as the computation progresses. Whenever we mention some qubits receiving corrections, it is, in fact, these adjustment we are refering to.

The first step comes in when we measure the first qubit. If the measurement result is 0, we do not need to do anything, as the computation is already on the correct branch. If the

measurement result is 1, however, we need to force it back to the branch where the result would have been 0. But how does one do it? Note that the measurement is done in basis $HR(\theta) = |0\rangle \pm e^{i\theta}|1\rangle$. When we measure 0, the state was $|0\rangle + e^{i\theta}|1\rangle$. When we measure 1, the state was $|0\rangle - e^{i\theta}|1\rangle$, which equals $\sigma_z(|0\rangle + e^{i\theta}|1\rangle)$. So to force the computation back to the correct branch, we need to apply σ_z to this qubit, if the result of its measurement is 1. But, of course, one cannot apply a gate on a qubit that is already measured. The key to finding out a runnable pattern is in solving this problem.

To resolve this issue, we apply a stabilizer, $\hat{S}$, to a qubit that is a neighbour to the one that is to be measured, if the measurement result is 1. This assures that σ_z is applied to a qubit that needs to be measured, without changing the graph properties. If one can find a way to apply stabilizers to a graph in a non-conflicting order, such that one ends up with an equivalent graph with σ_z applied to qubits that are to be measured, one has found a way to perform a definite deterministic computation using the graph. We say one has found a *flow pattern*. The flow pattern thus refers to the order of measurement of qubits and finding out which qubit receives corrections after each measurement.

As we mentioned in the introductory chapter, when qubits are connected to each other, measuring one of them does not cause the loss of the information contained in the measured qubit. Instead the information gets transfered or flows to another qubit. The qubit that is receiving the flow will also need to recieve a correction, if the result of the measurement is 1. The correction is either σ_x or σ_z. It is worth mentioning that the flow pattern for a graph with a fixed set of inputs and outputs is not unique, however, the computation is.

To clarify what was explained in the previous paragraph, let's try to find a set of stabilizers for the graph of Fig. 4.1. Qubits 1, 2, 3 and 4 are the ones that are measured. Let's start with qubit 1. It should see a σ_z, so we apply the stabilizer to qubit 4 as its neighbor, conditioned on s_1, which is the result of measuring qubit 1. We do the same for qubits 2, 3 and 4. We denote the results of measurement of qubit i by s_i. It seems there is no conflict in applying the stabilizers as we have chosen to do. Qubit 2 can be measured first. Then qubits 1 and 3 receive *corrections* based on the result of this measurement. Qubits 1 and 3 are measured next. This results into corrections on qubits 4 and 7. Now qubit 4 is measured. Qubit 5 receives correction and completes the computation. For this example, we ended up with three different time steps to complete the computation. One says the computation has a *depth complexity* of 3.

Kashefi *et al.* have shown (Danos et Kashefi, 2006) that the method described above leads to the following algorithm to find the flow pattern on a graph:

1. Fix which qubits are inputs and outputs.
2. The qubit receiving the flow should be measured after the one sending the flow, if it is

to be measured at all.

3. All neighbours of the flow recipient qubit should be measured after the flow generating qubit, if they are to be measured at all.

Now lets find the equivalent circuit to the graph of our example. To do so, we look at the succession of flow, shown by arrows in Fig. 4.3(a). There is an arrow from qubit 1 to 4 and

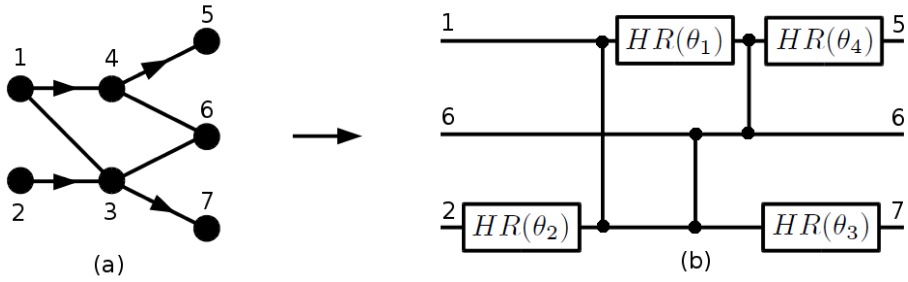

Figure 4.3 An example of how to translate a flow pattern into a circuit. (a) After each qubit is measured, following the arrows, the information flows from that qubit to another one. (b) Following the arrows on a graph and applying a $HR(\theta)$ gate for each measurement allows one to follow the evolution of a logical qubit and subsequently find an equivalent circuit.

from 4 to 5. This shows the evolution of a logical qubit, hence constitutes a line of a circuit, which is the upper line of circuit shown in Fig. 4.3(b). This evolution is as follows: the logical qubit, or information, on this line first sees a controlled-Z with qubit 3. Hence, we drop a cZ from the upper line. Then, qubit 1 is measured with some angle θ, hence a gate $HR(\theta_1)$ is applied to the logical qubit. We add this to the line. At this point, the information has flown from qubit 1 to 4, where it sees a controlled-Z with qubit 6. A vertical line connecting the upper and middle line signifies this cZ. The measurement of qubit 4 applies $HR(\theta_2)$ to the logical qubit, we add this gate to the line and conclude the evolution of this logical qubit. There are arrows from qubit 2 to 3 and from 3 to 7, which correspond to the evolution of a second logical qubit, that makes up the lower line of the circuit. Qubit 6 has no flow going from it or to it. It alone constitues the middle line of the circuit. At this point, we have the full circuit equivalent of the graph.

4.3 Flow and Loop Graph: Concept of Generalized Flow

It is very interesting to consider the particular graph depicted in Fig. 4.4(a), where qubit 1 is input in an arbitrary state $|\psi\rangle$ and qubits 3 and 4 are outputs. When looking for a flow

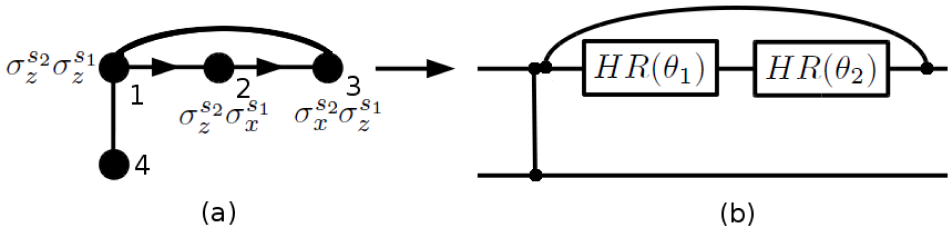

Figure 4.4 A graph that does not have a flow. (a) One tries to find a set of stabilizers that allow deterministic computation on this graph. However, as qubit 1 is a neighbour of qubit 3, it should receive $\sigma_z^{s_2}$ after it is already measured, which is not possible. (b) A circuit equivalent to the graph. The logical qubit on the upper line applies a controlled-Z to itself in the past, hence the circuit does not respect proper time ordering and is not runnable.

on this graph, we first want to measure the only input qubit that is to be measured, namely qubit 1 and then measure qubit 2. Hence, we need to apply two stabilizers: one to qubit 2, as the qubit that receives flow from qubit 1, and another one to qubit 3, as the qubit that receives flow from qubit 2. However, the application of the stabilizer on qubit 3 applies a σ_z correction on qubit 1, conditioned on the result of measuring qubit 2. The sequence of stabilizers is shown in Fig. 4.4(a). According to the third condition of the algorithm to find a flow, qubit 1, that is a neighbour of qubit 3, should be measured after qubit 2. But this qubit is already measured! This means one may not find a flow pattern on the loop graph.

It is still instructive, however, to continue and write out the equivalent circuit to the graph with the flow pattern we tried to define on it. Let us take the two arrows to define the evolution of a logical qubit, which will be the upper line of the circuit (Fig. 4.4(b)). Qubit 4 is the lower line. First, there is a cZ between the logical qubit of the upper line and qubit 4 or the lower line. Measuring qubit 1 applies the gate $HR(\theta_1)$ to it. Measuring qubit 2 applies $HR(\theta_2)$ to it. At this point, depending on the result of measurement of qubit 2, qubit 1 should receive a σ_z correction. This correction is equivalent to the application of a controlled-Z operation between qubits 3 and 1. In the circuit, this is equivalent to the logical qubit of the upper line undergoing a controlled-Z at the time its state is determined by qubit 1 to the time it is being determined by qubit 3. Hence, this qubit is undergoing a controlled-Z to its own past or future! It seems that we have managed to make a closed time-like curve in our circuit. Is it possible to find a circuit equivalent to the loop graph that is runnable, *i.e.*, respects the time ordering for computation? The answer is yes. One can find a runnable circuit by extending the concept of flow.

The extension to the concept of flow is the generalized flow, where one applies the stabilizer to a set of qubits that are the neighbours of the measured one (Browne *et al.*, 2007). It is possible for a graph to have a generalized flow and not a flow. It is worth mentioning that the

generalized flow in general reduces the depth complexity of the computation. The algorithm to find a generalized flow on a graph is the following.

1. Fix which qubits are the inputs and outputs.
2. The qubits receiving flows, collectively called $g(i)$, should be measured after the one sending the flows (i), if they are to be measured at all.
3. The measured qubit i should have an odd number of connections to the qubits $g(i)$ that are receiving the flow.
4. All qubits with an odd number of connections to $g(i)$ should be measured after the flow generating qubit i, if they are to be measured at all.

The generalized flow of the loop graph is shown in Fig. 4.5(a). Qubit 1 is measured first. For

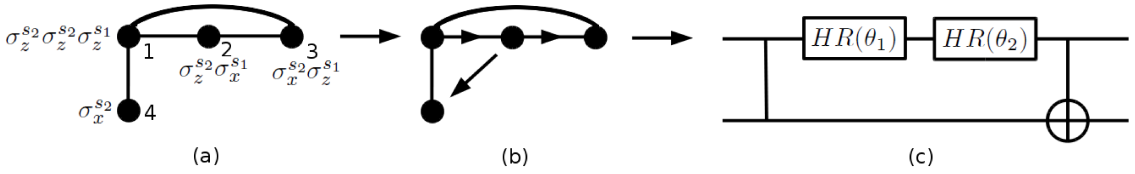

Figure 4.5 Generalized flow on the 4-qubit loop graph. (a) The sequence of stabilizers that allows a deterministic computation. (b) Generalized flow is marked by arrows on the graph. The qubits at the tip of the arrows should receive a correction if the qubits at the beginning of the arrows are measured to be 1. (c) The circuit equivalent to the generalized flow defined on the 4-qubit loop graph.

it to have seen a σ_z before it is measured, we apply a stabilizer conditioned on the outcome of measuring qubit 1, s_1, to qubit 2. Now we need a σ_z for qubit 2, since it is about to be measured. So we apply a stabilizer to qubit 3 conditioned on s_2. According to the algorithm, for qubit 1 to be measured before qubit 2, it should have an even number of connections to the qubits receiving flow from qubit 2. So far, qubit 3 is the only qubit we have designated to receive correction from qubit 2, and qubit 1 has one connection to it, which is an odd number of connections. At this point, we are still at the same dead-end as when we were trying to find a flow. To fix this, we apply another stabilizer conditioned on s_2 on qubit 4. This applies another $\sigma_z^{s_2}$ on qubit 1, which cancels the first one. Now we have satisfied the condition for qubit 1 to have an even number of connections to the qubits recieving flow from qubit 2 and have the generalized flow of Fig. 4.5(b).

Looking at this graph, one finds the circuit shown in Fig. 4.5(c) as its equivalent circuit. The last 2-qubit gate in this circuit is a controlled-NOT ($cNOT$), which means the qubit on the lower line receives a σ_x operation if the qubit on the upper line has logical value 1. This

$cNOT$ operation comes from the σ_x correction of qubit 4, conditioned on the measurement result of qubit 2.

Using the generalized flow, we have found a runnable circuit equivalent to the loop graph. One can say we have found an operational meaning to the closed time-like curve (CTC) of the first circuit.

4.4 Loop Graph and the Notion of Time

Recently, da Silva, Galvao and Kashefi (SGK) (Dias da Silva *et al.*, 2011), showed the CTCs arising in the one-way model are equivalent to those proposed by Bennett, Schumacher and Svetlichny (BSS) (Bennett et Schumacher, 2004, 2002; Svetlichny, 2009, 2011). To understand their argument, we will first describe the proposal of BSS. Then following the logic of SGK, we will show how our 4-qubit loop graph is related to the proposal of BSS.

BSS argued that one can simulate a CTC using quantum teleportation. The goal of quantum teleportation is to send a quantum state from one party, Alice, to another, Bob, without sending a physical carrier for that state through a channel from Alice to Bob. Amazingly enough, this task can be accomplished if Alice and Bob have shared an EPR pair, say $(|00\rangle + |11\rangle)/\sqrt{2}$, so that they each hold one of the qubits in this pair. This pair can be created by the circuit shown in Fig. 4.6(a). The inputs qubits are in state $|+\rangle$. After the

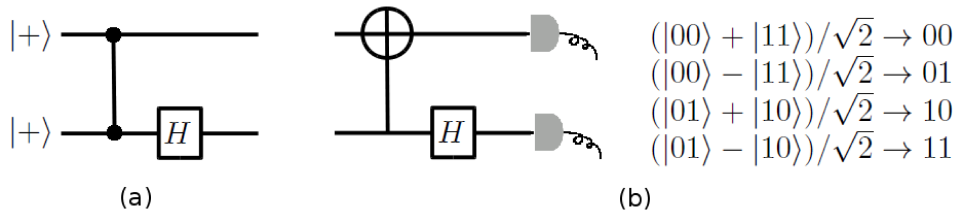

Figure 4.6 Creation of the EPR pair and measurement in Bell basis as necessary steps for quantum teleportation. (a) The inputs $|+\rangle|+\rangle$ to this circuit result into output $|00\rangle + |11\rangle)/\sqrt{2}$. (b) Sending two qubits to this circuit effectively projects them into the Bell basis, because each Bell state that goes through this circuit is transformed to give a unique result at the detectors, shown on the right of the figure.

controled-Z operation, they become

$$\frac{1}{2}(|00\rangle + |01\rangle + |10\rangle - |11\rangle)$$

and the Hadamard gate changes this state to

$$\frac{1}{\sqrt{2}}(|00\rangle + |11\rangle).$$

Alice wants to send the state $|\psi\rangle = \alpha|0\rangle + \beta|1\rangle$ to Bob. For that, she projects the state $|\psi\rangle$ and the qubit that is her share of the EPR pair into one of the following four states:

$$\frac{1}{\sqrt{2}}(|00\rangle + |11\rangle) \tag{4.1a}$$

$$\frac{1}{\sqrt{2}}(|00\rangle - |11\rangle) \tag{4.1b}$$

$$\frac{1}{\sqrt{2}}(|01\rangle + |10\rangle) \tag{4.1c}$$

$$\frac{1}{\sqrt{2}}(|01\rangle - |10\rangle) \tag{4.1d}$$

These states are collectively called the Bell states. The circuit that projects a state into a Bell state is shown in Fig. 4.6(b). This circuit generates the following two bits as outputs:

$$\frac{1}{\sqrt{2}}(|00\rangle + |11\rangle) \rightarrow 00$$
$$\frac{1}{\sqrt{2}}(|00\rangle - |11\rangle) \rightarrow 10$$
$$\frac{1}{\sqrt{2}}(|01\rangle + |10\rangle) \rightarrow 01$$
$$\frac{1}{\sqrt{2}}(|01\rangle - |10\rangle) \rightarrow 11$$

Fig. 4.7(a) shows the complete circuit for teleporting a state. A Bell pair is created and is shared between Alice and Bob. Alice then applies a projection into a Bell state between the state that is to be teleported and her share of the Bell pair. Depending on what Alice measures on her detectors, Bob might need to apply single qubit unitary operators on the quantum state on his side to recover the state $|\psi\rangle$. To clarify how teleportation works, the evolution of the qubit in the circuit is shown in Fig. 4.7(b), which is equivalent to that of Fig. 4.7(a). The input to the circuit is

$$\left(\frac{|0\rangle + |1\rangle}{\sqrt{2}}\right) \otimes \left(\frac{|0\rangle + |1\rangle}{\sqrt{2}}\right) \otimes (\alpha|0\rangle + \beta|1\rangle)$$

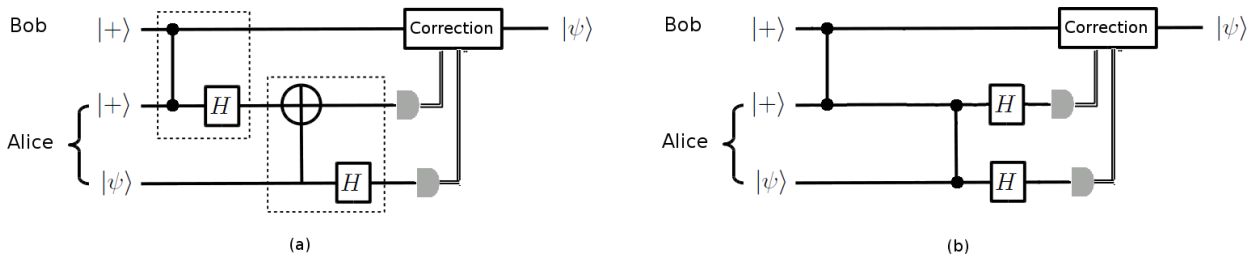

Figure 4.7 Teleportation circuit. (a) Alice and Bob share an EPR pair. Alice projects the state $|\psi\rangle$ to be teleported with her share of the EPR pair onto the Bell Basis. Bob might need to apply corrections on his qubit to recover $|\psi\rangle$. (b) Substituting the cNOT gate with its equivalent combination of Hadamard, cZ, Hadamard gives this equivalent circuit for quantum teleportation.

The step by step evolution of this input as it goes through the circuit is described bellow.

$$cZ_{1,2} \rightarrow \frac{(|00\rangle + |01\rangle + |10\rangle - |11\rangle)}{2} \otimes (\alpha|0\rangle + \beta|1\rangle)$$

$$cZ_{2,3} \rightarrow \frac{1}{2}(\alpha|000\rangle + \alpha|010\rangle + \alpha|100\rangle - \alpha|110\rangle + \beta|001\rangle - \beta|011\rangle + \beta|101\rangle + \beta|111\rangle)$$

$$\begin{aligned} H_2 \rightarrow (&\alpha|000\rangle + \alpha|010\rangle + \alpha|000\rangle - \alpha|010\rangle \\ &+ \alpha|100\rangle + \alpha|110\rangle - \alpha|100\rangle + \alpha|110\rangle \\ &+ \beta|001\rangle + \beta|011\rangle - \beta|001\rangle + \beta|011\rangle \\ &+ \beta|101\rangle + \beta|111\rangle + \beta|101\rangle - \beta|111\rangle)/(2\sqrt{2}) \\ = (&\alpha|000\rangle + \alpha|110\rangle + \beta|011\rangle + \beta|101\rangle)/\sqrt{2} \end{aligned}$$

$$\begin{aligned} H_3 \rightarrow (&\alpha|000\rangle + \alpha|001\rangle + \alpha|110\rangle + \alpha|111\rangle \\ &+\beta|010\rangle - \beta|011\rangle + \beta|100\rangle - \beta|101\rangle)/2 \\ = &[(\alpha|0\rangle + \beta|1\rangle)|00\rangle + (\alpha|0\rangle - \beta|1\rangle)|01\rangle]/2 \\ &+ [(\alpha|1\rangle + \beta|0\rangle)|10\rangle + (\alpha|1\rangle - \beta|0\rangle)|11\rangle]/2 \end{aligned}$$

When Alice measures 0 in both detectors, the state of qubit on Bob's side is already $|\psi\rangle = \alpha|0\rangle + \beta|1\rangle$, without the need for further correction. If Alice meausures 0 on detector 1 and 1 on detector 2, Bob has the state $\alpha|0\rangle - \beta|1\rangle$, which he changes to $|\psi\rangle$ by applying σ_z to it.

If Alice measures 1 in detector 1 and 0 in detector 2, Bob has the state $\alpha|1\rangle + \beta|0\rangle$, which he changes to $|\psi\rangle$ by applying σ_x to it, and, finally, if Alice detects 1 in both detectors, Bob has the state $\alpha|1\rangle - \beta|0\rangle$, which he changes to $|\psi\rangle$ by applying σ_x followed by σ_z to it. Note that as Alice has to notify Bob about her measurement results, Bob is not receiving information faster than the speed of light.

BSS proposed the idea that if one post-selects on both detectors measuring 0, which is the situation when Bob doesn't need to apply any corrections to his state to obtain $|\psi\rangle$, then it is as if Bob has received $|\psi\rangle$ even before Alice applies the Bell measurement. This scenario can simulate a CTC as depicted in Fig. 4.8(a). Qubit $|\psi\rangle_{in}$ enters the closed time-

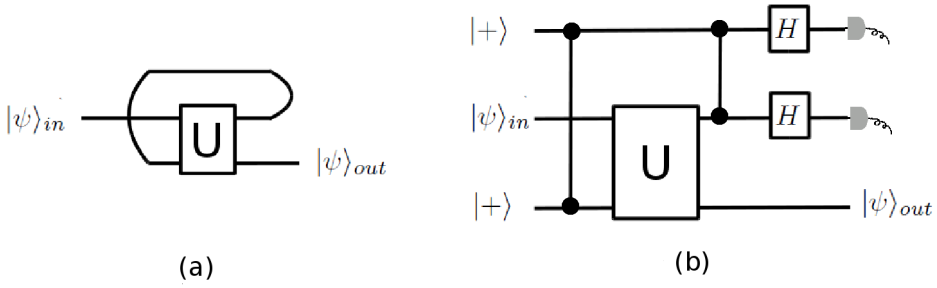

Figure 4.8 The circuit of the time-like curve as proposed by Bennett, Schumacher and Svetlichny. (a) The qubit enters the circuit, then it goes into a time-like curve and interacts with itself in the future (or itself in the past) through the unitary U, then it exits the curve. (b) This circuit can simulate the circuit with time-like curve, if one measures 0 in both detectors. This is because one can simulate the CTCs with quantum teleportation. The cZ gate between the first and third lines of this circuit corresponds to the creation of an EPR pair and the cZ and Hadamards on the first and second lines correspond to a projection on the Bell basis. Measuring 0 in both detectors corresponds to successful teleportation with no necessary corrections.

like curve, which is shown as a curved line in this figure and follows it. The qubit interacts with its future self through unitary U, goes backward in time, then again goes forward in time, interacts with its past self and exits the CTC. Fig. 4.8(b), which is the rearranged teleportation circuit, simulates the CTC circuit of Fig. 4.8(a), when post-selection on both detectors measuring 0 succeeds.

Going back to our circuit of Fig. 4.4(b), the circuit is rewritten in terms of its equivalent BSS circuit as shown in Fig. 4.9.

In Fig. 4.9(b) we have simply redrawn the time-like loop of the circuit of Fig. 4.9(a) in the form of BSS. In Fig. 4.9(c) is the results of substituting the circuit equivalents of the EPR pair creation and Bell measurement. We have previously shown that the circuits of Figs. 4.9(a) and 4.9(d) are equivalent. Here we are claiming that the circuit of Fig. 4.9(d)

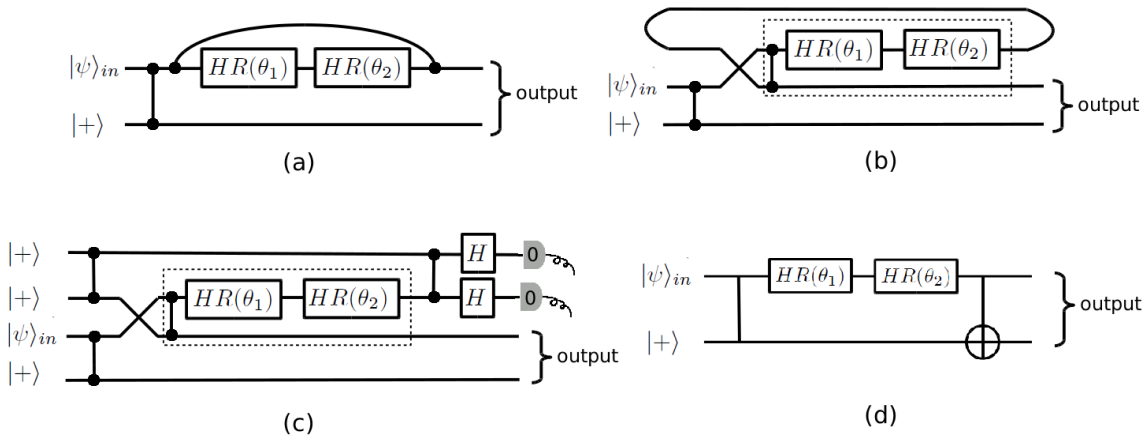

Figure 4.9 The relation of our 4-qubit loop graph and time-like curves. (a) The circuit with a time-like loop that is associated with the loop graph. (b) One can rewrite the time-like curve of the circuit in the form of the circuit of BSS. (c) The time-like curve is translated into the circuit of quantum teleportation. The time traveling is successful when both detectors detect 0. (d) The runnable circuit that is equivalent to the computation done by the loop graph and also is equivalent to the circuit of part (c), given both detectors have detected 0.

is equivalent to the BSS circuit of Fig. 4.9(c), given the post-selection on both detectors measuring 0 have succeeded. Indeed, Appendix A contains the calculations showing that the outputs from both circuits do agree with each other and are equal to

$$\frac{1}{2}\begin{pmatrix} (1+e^{i\theta_2})\alpha + (e^{i\theta_1}(1-e^{i}(\theta_2)\beta \\ (1+e^{i\theta_2})\alpha - (e^{i\theta_1}(1-e^{i}(\theta_2)\beta \\ (1-e^{i\theta_2})\alpha - (e^{i\theta_1}(1+e^{i}(\theta_2)\beta \\ (1-e^{i\theta_2})\alpha + (e^{i\theta_1}(1+e^{i}(\theta_2)\beta \end{pmatrix}.$$

Thus we have shown that our 4-qubit loop graph is equivalent to the circuit proposed by Bennett-Schumacher-Svetlichny, when the post-selection on this circuit has succeeded. Our graph is simulating a closed time-like curve in a deterministic manner.

Another very interesting point to observe is that the both output qubits of our circuit are affected by the events that have happened in the closed time-like curve. Depending on the choice of angles θ_1 and θ_2, they can even be entangled to each other. In other words, the qubit that has gone back in time and has interacted with its own past is also interacting with the qubit that is carried on the lower line of circuit of Fig. 4.9(d), and its actions in the closed time-like curve have affected this qubit, which was following the normal passage of time. We believe this interesting dynamics opens up new ways of thinking about the closed time-like curves.

The next chapter presents a novel method for the experimental realization of this 4-qubit loop graph. A detailed explanation of the simulation of the circuit using Maple V is also provided.

Chapter 5

Experimental Method

The 4-qubit loop graph with input and output qubits, defined in the previous chapter, is the smallest graph that has a generalized flow and no flow. In addition, it is a system that simulates a closed time-like curve without post selection. These characteristics were our motivation for an experimental realization of this graph.

This chapter presents a novel method for the experimental implementation of the loop graph. Quantum state tomography is overviewed as the means of characterization of the created state. The concepts of *purity* and *fidelity* are presented as the standard measures used to quantify the quality of the experiment. It ends with a description of the simulations of the experimental line and an analysis of the effects of errors from various optical elements on the final experimental result.

5.1 The Implementation Method

We use the polarization and path degrees of freedom of photons to physically implement the logical qubits, so that $|H\rangle = |0\rangle$, $|V\rangle = |1\rangle$, $|t\rangle = |0\rangle$ and $|r\rangle = |1\rangle$, where H and V stand for *Horizontal* and *Vertical* polarization and t and r represent the *transmitted* and *reflected* paths of photons after going through $50:50$ beam splitters.

To create the polarization entangled pair of photons, we use spontaneous parametric down conversion with collinear phase matching type II, using a PPKTP crystal in a cavity (Wolfgramm *et al.*, 2008). The details of the source are shown in Fig. 5.1 as a courtesy of the authors of reference (Wolfgramm *et al.*, 2008). As the phase matching is type II, a horizontally polarized pump photon is annihilated and a signal and idler photon are created, where one of them is vertically polarized and the other one is horizontally polarized. The two photons, due to collinear phase matching, are in the same spatial path. To separate them from each other, we send them to a $50:50$ beam splitter. The photons exit this beam splitter (BS) at separate output ports with probability $1/2$. We name one output port of this BS A and the other B. Subsequently, we refer to the photon that exits from port A as photon A and the one that exits from port B as photon B. We post-select on the events where there is only one photon in A and one in B by looking at the coincidence detections

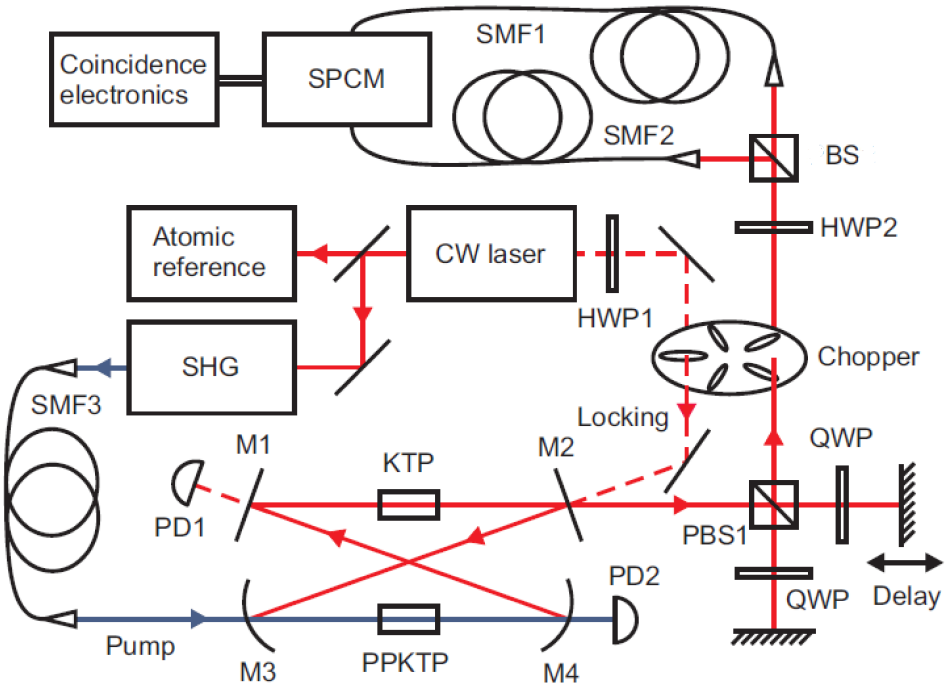

Figure 5.1 The source of entangled photons. PPKTP: periodically poled potassium titanyl phosphate, the down converting crystal, KTP: potassium titanyl phosphate compensation crystal, M1-4: cavity mirrors, PBS: polarization beam splitter, HWP: half-wave plate, QWP: quarter-wave plate, SMF: single-mode fiber, PD: photodiode. Figure is the courtesy of the groups of Aephraim Steinberg at the University of Toronto and Morgan Mitchel at ICFO, Barcelona, who have developed the source.

from the two detectors at the end of paths A and B. When the photons separate from each other, it is not clear whether the photon in an output port is the horizontally polarized one or the vertically polarized one. This fundamental lack of information gives rise to the entangled state $(|HV\rangle + |VH\rangle)/\sqrt{2}$, where the first qubit in each ket is the polarization state of photon A and the second qubit is that of photon B. We collect the photons into fibers and transfer them to the setup that creates the 4-qubit loop graph shown in Fig. 5.2. At the output, we flip the polarization of one of the photons to obtain $(|HH\rangle + |VV\rangle)/\sqrt{2}$.

To add the path DOF in state $(|t\rangle + |r\rangle)/\sqrt{2}$ to each photon, we send them through $50:50$ beam splitters. The path state of each photon after the beam splitters is $(|t\rangle + |r\rangle)/\sqrt{2}$. We add the labeling A and B to the states in the kets to clarify which photon is carrying which qubit. The state of the photons at this stage is

$$\frac{(|H_A H_B\rangle + |V_A V_B\rangle)}{\sqrt{2}} \frac{(|t_A\rangle + |r_A\rangle)}{\sqrt{2}} \frac{(|t_B\rangle + |r_B\rangle)}{\sqrt{2}}. \tag{5.1}$$

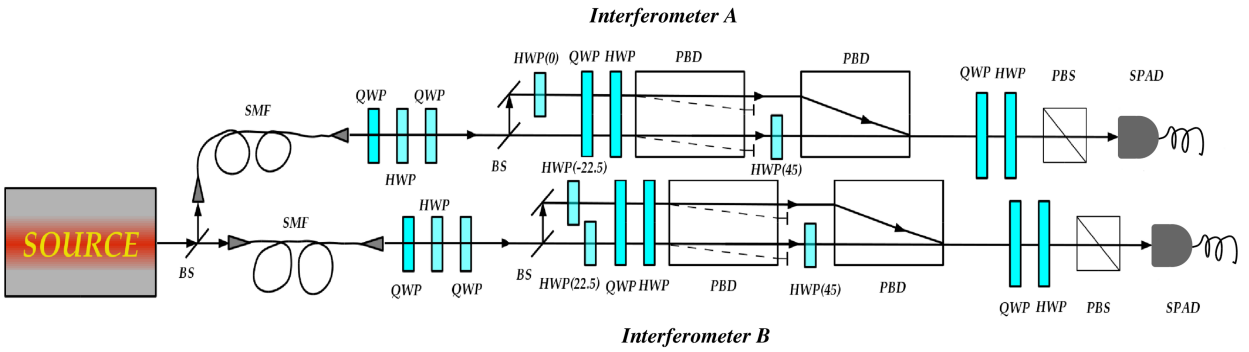

Figure 5.2 Schematic representation of the experimental setup. BS: 50 : 50 beam splitter, SMF: single-mode fiber, HWP: half-wave plate, QWP: quarter-wave plate, PBD: polarization beam displacer, PBS: polarization beam splitter, SPAD: single photon avalanche diode.

Now we add a half-wave plate (HWP) on the reflected path of the photon A. This applies a controlled-Z operation between the polarization and path qubits of this photon. The state becomes

$$\left[\frac{|H_A H_B\rangle}{\sqrt{2}}\frac{(|t_A\rangle+|r_A\rangle)}{\sqrt{2}}+\frac{|V_A V_B\rangle}{\sqrt{2}}\frac{(|t_A\rangle-|r_A\rangle)}{\sqrt{2}}\right]\frac{|t_B\rangle+|r_B\rangle}{\sqrt{2}}. \tag{5.2}$$

It is worth noting that since the polarization qubits of the two photons have the same logical value in each ket, at this point one cannot know if the cZ was applied between the polarization of photon A and its path or the polarization of photon B and the path qubit on photon A. Applying a Hadamard operation on the polarization qubit of photon A, using a HWP rotated 22.5° breaks the similarity between polarization states of photons A and B and yields the state

$$\left[\frac{|H_A H_B\rangle+|V_A H_B\rangle}{\sqrt{2}}\frac{|t_A\rangle+|r_A\rangle}{\sqrt{2}}+\frac{|H_A V_B\rangle-|V_A V_B\rangle}{\sqrt{2}}\frac{|t_A\rangle-|r_A\rangle}{\sqrt{2}}\right]\frac{|t_B\rangle+|r_B\rangle}{\sqrt{2}}.$$

Hence, the controlled-Z operation is now between the polarization of photon A and the path of the other one. The application of the controlled-Z and Hadamard in this order, so as to implement a deterministic two-photon gate without real two-photon interactions, is the novel method that creates the loop. At this point, the graph of Fig. 5.3(a) is obtained. Two other HWPs, placed in the reflected paths of the two photons, complete the graph by applying the controlled-Z between the polarization and path qubits carried on the same photon (Fig. 5.3(b)). These settings of HWPs amount to the presence of the $HWP(0)$ in the reflected arm of interferometer A, plus $HWP(-22.5)$ and $HWP(22.5)$ in the reflected and transmitted arms of interferometer B as shown in Fig. 5.2.

At this point, the 4-qubit loop graph is succesfully created. We write the state of this graph by ordering the qubits in the kets as $|P_A K_A P_B K_B\rangle$, where P_A and K_A are polarization

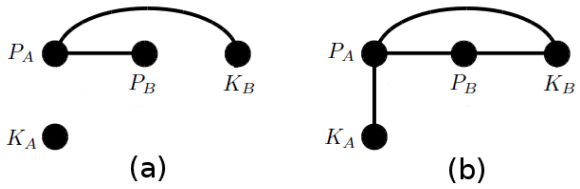

Figure 5.3 The creation of the loop graph. (a) The state after the application of a $HWP(0°)$ on the reflected path of photon B and a Hadamard on polarization qubit of photon B. (b) The state after the completion of all controlled-Z gates.

and path qubits carried on photon A and P_B and K_B are polarization and path qubits carried on photon B. The state of the graph is

$$\begin{aligned}&(|HtHt\rangle + |HtHr\rangle + |HtVt\rangle - |HtVr\rangle\\ &+|HrHt\rangle + |HrHr\rangle + |HrVt\rangle - |HrVr\rangle\\ &+|VtHt\rangle + |VtHr\rangle - |VtVt\rangle - |VtVr\rangle\\ &-|VrHt\rangle + |VrHr\rangle + |VrVt\rangle + |VrVr\rangle)/4.\end{aligned}$$

What remains to be done is to show how to confirm experimentally that this state is actually created and how to perform computation with it.

5.2 Quantum State Tomography

A real physical system is very different from the theoretical construct we explained above, as no optical element is perfect. This means, depending on the performance of each of the optical elements in the setup, that a state is created which is not exactly the same as the theoretical prediction. Quantum state tomography can determine what this created state is. It should be emphasized that tomography requires multiple copies of the state or an ensemble of identical states. These copies are readily available in our experimental setup. We will work with the coincidence between the two detectors at the ends of lines A and B. There are some properties of the setup that limit the measurement time, which are discussed in detail in the next chapter.

Using the language of qubits, we follow (James *et al.*, 2001) and (Altepeter *et al.*, 2010) to explain the concept behind quantum state tomography. Starting with just one qubit, imagine an arbitrary 1-qubit state, $|\psi\rangle$ that is represented by a point on or in the Bloch sphere. The quantum state is said to be pure only if it is on the sphere, otherwise it is partially pure or fully mixed. Although the concept of state tomography applies to all physical implementations

of qubits, it is explained here using polarization of photons as qubits. The density matrix corresponding to state $|\psi\rangle$ is $\hat{\rho} = |\psi\rangle\langle\psi|$. The goal of state tomography is to somehow reconstruct this density matrix. Any 2×2 density matrix can be written as

$$\hat{\rho} = \frac{1}{2}\sum_{i=0}^{3} \frac{S_i}{S_0}\hat{\sigma}_i, \tag{5.3}$$

where $\hat{\sigma}_i$ are the Pauli matrices and S_i are the coefficients to be determined. These coefficients are called the *Stokes parameters* and are the probability of finding the state $\hat{\rho}$ in $\hat{\sigma}_i$ upon measurement. The Stokes parameters corresponding to a state provide enough information to fully determine that state. The following explains how one can find the values S_i.

If one measures $\hat{\rho}$ in some basis $|\Phi\rangle$, the probability of finding $\hat{\rho}$ in $|\Phi\rangle$ is

$$P_\Phi = \langle\Phi|\hat{\rho}|\Phi\rangle \tag{5.4}$$

$$= \mathrm{Tr}\{|\Phi\rangle\langle\Phi|\hat{\rho}\}. \tag{5.5}$$

If we consider $|\Phi\rangle\langle\Phi|$ to be the Pauli bases, then S_i which are the probability of finding $\hat{\rho}$ in $\hat{\sigma}_i$ become

$$S_i = \mathrm{Tr}\{\hat{\sigma}_i\hat{\rho}\}. \tag{5.6}$$

In practice, the probability of measurement of various bases does not depend only on the state $\hat{\rho}$, but also on the efficiency of collection of photons and the detectors. Hence, a parameter η is added to take these practical efficiencies into account and write

$$S_i = \eta\,\mathrm{Tr}\{\hat{\sigma}_i\hat{\rho}\}. \tag{5.7}$$

We know that

$$\hat{\sigma_0} = |H\rangle\langle H| + |V\rangle\langle V| \tag{5.8a}$$

$$\hat{\sigma_1} = |H\rangle\langle H| - |V\rangle\langle V| = 2|H\rangle\langle H| - \hat{\sigma_0} \tag{5.8b}$$

$$\hat{\sigma_2} = |H\rangle\langle V| + |V\rangle\langle H| = 2|D\rangle\langle D| - \hat{\sigma_0} \tag{5.8c}$$

$$\hat{\sigma_3} = i|H\rangle\langle V| - i|V\rangle\langle H| = 2|R\rangle\langle R| - \hat{\sigma_0}. \tag{5.8d}$$

Substituting these in equation 5.7, one obtains

$$S_0 = \eta \,\mathrm{Tr}\{\hat{\sigma_0}\hat{\rho}\} = \eta(\langle H|\hat{\rho}|H\rangle + \langle V|\hat{\rho}|V\rangle) \tag{5.9a}$$

$$S_1 = \eta \,\mathrm{Tr}\{\hat{\sigma_1}\hat{\rho}\} = 2\eta\langle H|\hat{\rho}|H\rangle - S_0 \tag{5.9b}$$

$$S_2 = \eta \,\mathrm{Tr}\{\hat{\sigma_2}\hat{\rho}\} = 2\eta\langle D|\hat{\rho}|D\rangle - S_0 \tag{5.9c}$$

$$S_3 = \eta \,\mathrm{Tr}\{\hat{\sigma_3}\hat{\rho}\} = 2\eta\langle R|\hat{\rho}|R\rangle - S_0 \tag{5.9d}$$

Given these relations for S_i, one can relate them to experimental results. S_0 is the total number of counts per second, n_0. One can find this number by measuring the state in two orthogonal bases, $|H\rangle\langle H|$ and $|V\rangle\langle V|$, and add the counts. As $\eta\langle H|\hat{\rho}|H\rangle$ is the number of counts in $|H\rangle$ basis, n_1, S_1 equals $2n_1 - n_0$. Given $\eta\langle D|\hat{\rho}|D\rangle = n_2$ and $\eta\langle R|\hat{\rho}|R\rangle = n_3$, $S_2 = 2n_2 - n_0$ and $S_3 = 2n_3 - n_0$. By measuring n_0, n_1, n_2 and n_3, the values of S_i are determined and, using Eq. (5.3), $\hat{\rho}$ can be reconstructed.

This method can be generalized to the reconstruction of an m-qubit state, $\hat{\rho}_m$:

$$\hat{\rho}_m = \frac{1}{2^m} \sum_{i,j,\ldots,m=0}^{3} S_{i,j,\ldots,m} \hat{\sigma}_i \hat{\sigma}_j \ldots \hat{\sigma}_m. \tag{5.10}$$

The measurement bases chosen in practice are any combination of $\mu_0 = |H\rangle\langle H|$, $\mu_1 = |V\rangle\langle V|$, $\mu_2 = |D\rangle\langle D|$ and $\mu_3 = |R\rangle\langle R|$, ..., which are linearly independent. The measurement results are

$$n_{\kappa_i,\kappa_j,\ldots,\kappa_m} = Tr(\rho)\hat{m}(\mu_{\kappa_i} \otimes \mu_{\kappa_j} \otimes \ldots \mu_{\kappa_m}). \tag{5.11}$$

Substituting for $\hat{\rho}$ from Eq. 5.10, one obtains

$$n_{\kappa_i,\kappa_j,\ldots,\kappa_m} = \frac{\eta}{2^m} \sum_{i,j,\ldots,m=0}^{3} S_{i,j,\ldots,m} Tr(\hat{\sigma}_i \mu_{\kappa_i}) Tr(\hat{\sigma}_j \mu_{\kappa_j}) \ldots Tr(\hat{\sigma}_m \mu_{\kappa_m}). \tag{5.12}$$

This is a system of equations that relates the measured values, n, to the coefficients S and can be written in the matrix form as $N = M \cdot S$. Inverting this system of equations yields $S = M^{-1}N$. Solving for S allows the reconstruction of the state ρ_m. This method is called linear inversion. In practice, the method of linear inversion does not guarantee a physical density matrix for ρ_m. Another method called Maximum Likelihood is used that guarantees a physical result.

For a density matrix to be physical, it should be positive definite, meaning it should satisfy the relation $\langle\phi|\hat{\rho}|\phi\rangle \geq 0$ for all ϕ. (James *et al.*, 2001) showed that writing out ρ in the form $\hat{T}^\dagger\hat{T}/\,\mathrm{Tr}\{\hat{T}^\dagger\hat{T}\}$ results in a positive definite matrix for $\hat{\rho}$. For reconstructing the density matrix for an m-qubit state, T is a $2^m \times 2^m$ matrix and has $2^m \times 2^m - 1$ independent real

parameters. Hence, to have enough information to reconstruct the density matrix, $2^m \times 2^m$ measurements in linearly independent bases are required. It is computationally more efficient to devise T in the form of a lower triangular matrix

$$T = \begin{pmatrix} t_1 & 0 & 0 & \dots & 0 \\ t_{(2^m+1)} + it_{(2^m+2)} & t_2 & 0 & \dots & 0 \\ \vdots & & \ddots & & 0 \\ t_{(2^m \times 2^m-1)} + it_{(2^m \times 2^m)} & t_{(2^m \times 2^m-3)} + it_{(2^m \times 2^m-2)} & \dots & & t_{2^m} \end{pmatrix}.$$

Theoretically, if we measure ρ_m, that is now a function of parameters t_i, in each basis $|\phi_\kappa\rangle$, where $\kappa = 0 \dots 2^m \times 2^m$, we expect to obtain $\bar{n}_\kappa = \eta\langle\phi_\kappa|\hat{\rho}_m|\phi_\kappa\rangle$ photons per second for this basis. The Maximum Likelihood method, in essence, is finding the physical $\hat{\rho}_m$ that is maximally likely to give n_κ, which are the actual experimental number of photons per second. This amounts to finding $\hat{\rho}_m$ that results into $\bar{n}_\kappa$ that are as close to n_κ as possible. So one should find the parameters t_i that minimize this function:

$$\Gamma(t_1, t_2, \dots, t_{2^m}) = \sum_{\kappa}^{2^m} \frac{\eta\langle\phi_\kappa|\hat{\rho}_m|\phi_\kappa\rangle - n_\kappa}{2\eta\langle\phi_\kappa|\hat{\rho}_m|\phi_\kappa\rangle - n_\kappa}. \tag{5.13}$$

To reconstruct the 2-qubit states, we have used the methods of Linear Inversion and also the Maximum Likelihood, using Matlab. For Maximum Likelihood, we used the routine `fminsearch` for optimization for two qubits. `fminsearch` finds the minimum of a scalar multi-variable function from an initial guess. For four qubits, this method is too slow. Thus, the results of the experiment are reported in terms of the 2-qubit density matrices associated to each measurement basis for polarization. The next section clarifies what measurement bases have been chosen and how the measurements were performed.

In order to quantify the quality of the experimental data, the purity of each experimentally created state and its fidelity with the target state are reported. A state is pure if it can be represented by a ket, $|\psi\rangle$, or sum of kets, $\sum_i |\psi_i\rangle$. If a state has to be described as a statistical mixture of various kets, then it is not pure. For example, it is possible to have a state that includes 50% of $(|HH\rangle + |VV\rangle)/\sqrt{2}$, 25% of $|HH\rangle$ and 25% of $|VV\rangle$. This state cannot be written as a superposition of different kets, hence it is not a pure state. The purity of a state ρ is determined by $\mathrm{Tr}\{\rho^2\}$.

The state created in our experiment is a pure state and the results of the computation should also be pure, which means they should ideally have purity of 1.

Fidelity is a measure of overlap between the experimental state created and the theoretical one, the target state. As the theoretical state is pure, the overlap of the theoretical result

$\rho = |\psi\rangle\langle\psi|$ and the experimental result σ can be calculated as $\langle\psi|\sigma|\psi\rangle$, and the fidelity is calculated by $\mathrm{Tr}\{\rho\sigma\}$.

5.3 Measurements for Tomography of the 4-qubit Loop Graph

For the 4-qubit graph, 16 measurements are needed on polarization qubits and, for each of these measurements, 16 measurements are needed for path qubits.

Measurements on polarization qubits are performed using a QWP followed by a HWP before a polarization beam displacer (PBD). The combination of Quarter and Half-wave plate allows us to choose any desired measurement basis. We have chosen combinations of Pauli matrices, which are explicitly enumerated in the simulation chapter. The PBD is aligned such that it allows horizontally polarized light continue on its original path and displaces the vertically polarized light so that it can be discarded.

After the PBD, the polarization of both reflected and transmitted paths are horizontal. Using a $HWP(45^\circ)$ in the transmitted arm, the polarization of photon is flipped to vertical. Hence, if the qubit in path encoding was $\alpha|t\rangle + \beta|r\rangle$ after the PBD, this HWP changes it to $\alpha|V\rangle + \beta|H\rangle$. After this change of path to polarization encoding is done,the set of QWP, HWP and PBS performs tomography on the path qubit. However, prior to these measurements, the phase of the interferometers have to be set correctly. The next section details how this is done.

5.3.1 Setting the Phase of Interferometers for Measuring Path Qubits

Here it is first explained how to set the phase of an interferometer using the visibility of fringes. Then the specifics of the set up are discussed and the method to set the phases within the interferometers is explained.

In the interferometer of Fig. 5.4, the intensity of light exiting output port 1 depends on the fields coming from each arm and the phase difference between these arms, denoted by ϕ, such that

$$I = |E_1 + e^{i\phi}E_2|^2 = |E_1|^2 + |E_2|^2 + e^{-i\phi}E_1E_2^* + e^{i\phi}E_1^*E_2.$$

Assuming E_1 and E_2 are real, the output of the interferometer in port 1 becomes $I_{total} = I_1 + I_2 + 2\cos(\phi)E_1E_2$. Changing phase ϕ from 0 to π causes I_{total} to vary from a maximum $I_1 + I_2 + 2E_1E_2$ to a minimum $I_1 + I_2 - 2E_1E_2$. If the fields in both arms have the same

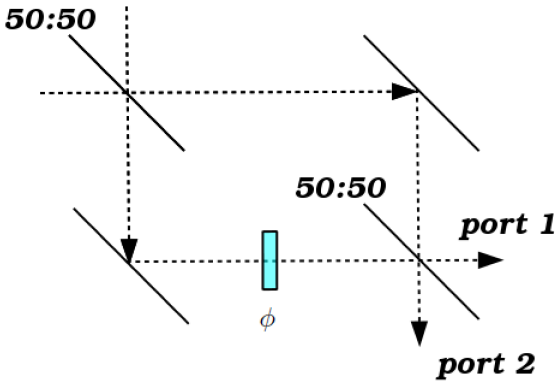

Figure 5.4 The intensity of light exiting the interferometer from port 1 provides complete information about the phase difference between the two arms of the interferometer, ϕ.

value, then varying ϕ takes the output from $4I$ to 0. Hence the amount of light exiting this output port gives us complete information about the phase ϕ, which we refer to as the phase of the interferometer.

To see how this logic works for the interferometers in the setup, let's take a close look at them. One starts with interferometer A shown in Fig. 5.5. The interferometer starts at

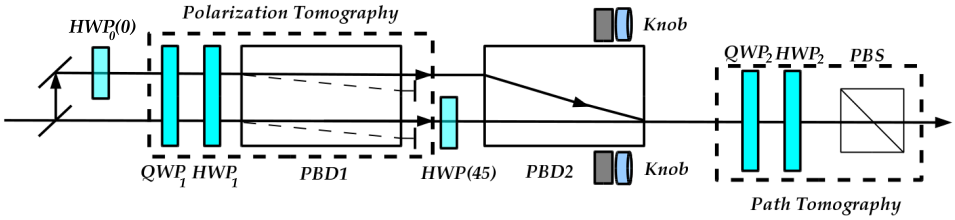

Figure 5.5 The components of one of the interferometers of the experiment. The phase of the interferometer is changed using any of the knobs on the standard mirror mount used for $PBD2$. Similar knobs are used to set the phase of the other interferometer to any desired value.

the 50 : 50 beam splitter, after which the path of the photon splits into two possibilities, transmitted and reflected. The reflected path sees the HWP that performs a cZ required as a part of the graph state preparation. This waveplate applies a π phase shift between the horizontal and vertical polarized light in the reflected arm. Then both arms see the quarter and half-wave plate for polarization tomography, followed by $PBD1$, which separates the horizontal and vertical components of light by displacing the vertical component and allowing the horizontal component to continue on its original path. After this PBD, one is working only with one polarization, namely horizontal. If the interferometer is closed at this point, given the optical path difference between the two arms is less than the coherence

length of photons and assuming the BS is perfectly 50 : 50, the state of the photon will be $(e^{i\phi_1}|t\rangle + |r\rangle)/\sqrt{2}$. Instead, one flips the polarization of the transmitted arm to vertical, then closes the interferometer by sending the two arms into $PBD2$, that is rotated by 90° with respect to $PBD1$, so it displaces the horizontally polarized light of the reflected arm to overlap with the vertically polarized light of the transmitted arm. This gives the state $e^{i\phi_A}(|V\rangle + |H\rangle)/\sqrt{2}$ after $PBD2$. $PBD2$ is mounted in a standard optical mirror mount with two adjusting knobs. Turning any of these knobs changes the phase of the interferometer ϕ_B. A similar situation applies also to interferometer B. The question now is what setting should one choose for ϕ_A and ϕ_B in the experiment?

If one keeps the angle of the fast axis of QWP_1 and HWP_1 at 0, HWP_0, in interferometer A, is the only optical element that introduces a definite amount of phase shift to the light. If the input light to the interferometer is horizontally polarized, this HWP does not introduce any phase shift, hence we want the phase of the interferometer to be such that for horizontal input the phase ϕ_A is 0 and the output in terms of path qubits is $(|t\rangle + |r\rangle)/\sqrt{2}$, which after conversion to polarization qubit corresponds to $(|H\rangle + |V\rangle)/\sqrt{2}$. This choice of ϕ_A is consistent with the vertically polarized input, because for that input the effect of the HWP_0 is to create the path qubit $(|t\rangle - |r\rangle)/\sqrt{2}$, which corresponds to $(|H\rangle - |V\rangle)/\sqrt{2}$, which corresponds to the choice of $\phi_A = 0$. The procedure to set this phase to 0 is as follows: we make sure the input photons to the interferometer are horizontally polarized. Just before QWP_2 and HWP_2, the state of each photon is $(|H\rangle + e^{i\phi_A}|V\rangle)/\sqrt{2}$. We set QWP_2 and HWP_2 to correspond to measuring in $\bar{D}/D$ basis. If the state of photon is $|D\rangle = (|H\rangle + |V\rangle)/\sqrt{2}$, this setting of waveplates rotates it to $|H\rangle$ and the photon is transmitted through the PBS and goes to the detector. If the state is $|\bar{D}\rangle = (|H\rangle - |V\rangle)/\sqrt{2}$, it gets rotated to $|V\rangle$ and reflected at the PBS, hence the detector at transmission does not detect it. Since $|H\rangle = \frac{\sqrt{2}}{2}(|D\rangle + |\bar{D}\rangle)$ and $|V\rangle = \frac{\sqrt{2}}{2}(|D\rangle - |\bar{D}\rangle)$, the state $(|H\rangle + e^{i\phi_A}|V\rangle)/\sqrt{2}$ in terms of $|D\rangle$ and $|\bar{D}\rangle$ becomes $\frac{1+e^{i\phi_A}}{2}|D\rangle + \frac{1-e^{i\phi_A}}{2}|\bar{D}\rangle$. This means maximizing the output for waveplate settings corresponding to measuring $|D\rangle$ or minimizing the output for the waveplate settings corresponding to measuring $|\bar{D}\rangle$ guarantees $\phi = 0$. In practice, as the maximum or minimum do not have the highest sensitivity to phase variations, after minimizing on $|\bar{D}\rangle$, we change the setting of waveplates to measure in R/L basis and make sure the photon count per second is half of its maximum.

A similar reasoning applies to interferometer B. It turns out that for horizontaly polarized input, the path qubit should correspond to $|D\rangle$. The phase ϕ_B is set to 0 with the exact same method as was used for interferometer A.

After the phases of the interferometers are set properly, the QWP, HWP and PBS will carry on the required measurements for tomography on the path qubits.

5.4 Simulation of the Circuit equivalent to Graph

The goal in this section is to simulate the circuit equivalent to the graph and compare the results of the calculation from the circuit to that of the graph. Maple V is used for this purpose. The complete Maple code is in Appendix B. Here the steps of the simulation are explained in detail.

Maple V does not have a built-in function for tensor product between matrices, hence one starts by a subroutine to define the command $Kron(A, B)$ that calculates the tensor product $A \otimes B$ for matrices A and B. This subroutine is available online and is also detailed in the Appendix.

In all simulations, the state $|0\rangle$ is represented by the vector $[1, 0]$ and the state $|1\rangle$ by the the vector $[0, 1]$. Hence an arbitrary qubit $\alpha|0\rangle + \beta|1\rangle$ is given by

$$\psi = \begin{pmatrix} \alpha \\ \beta \end{pmatrix}$$

N-qubit states can be constructed by taking the tensor products of n single qubits. In order to simulate the circuit, one defines the unitary operations involved in the circuit. These are, in order, identity, controlled-Z, controlled-NOT, Hadamard, single qubit $R_z(\theta)$, and $J(\theta)$, which equals $HR(\theta)$:

$$Id = \begin{pmatrix} 1 & 0 \\ 0 & 1 \end{pmatrix}$$

$$cZ = \begin{pmatrix} 1 & 0 & 0 & 0 \\ 0 & 1 & 0 & 0 \\ 0 & 0 & 1 & 0 \\ 0 & 0 & 0 & -1 \end{pmatrix}$$

$$cNOT = \begin{pmatrix} 1 & 0 & 0 & 0 \\ 0 & 1 & 0 & 0 \\ 0 & 0 & 0 & 1 \\ 0 & 0 & 1 & 0 \end{pmatrix}$$

$$Hadamard = \frac{1}{2\sqrt{2}} \begin{pmatrix} 1 & 1 \\ 1 & -1 \end{pmatrix}$$

$$R(\theta) = \begin{pmatrix} 1 & 0 \\ 0 & \mathrm{e}^{i\theta} \end{pmatrix}$$

$$J(\theta) = \frac{1}{2\sqrt{2}} \begin{pmatrix} 1 & \mathrm{e}^{i\theta} \\ 1 & -\mathrm{e}^{i\theta} \end{pmatrix}$$

To construct the unitary matrix corresponding to the circuit, one takes into account the correct ordering of the gates as they are applied to the inputs. First cZ is applied, which is a 2-qubit gate. Then $HR(\theta_1)$ and $HR(\theta_2)$ are applied to the upper qubit, while the identity is applied to the lower one. The tensor product, between $HR(\theta_2)HR(\theta_1)$ and the Identity, performed by the command *Kron*, combines these single qubit gates to the suitable format so that they can be applied to two qubits. A $cNOT$ concludes the two qubit unitary, which is the unitary operation equivalent to the circuit. I call it the *TwoQubitUnitary*:

$$\frac{1}{2} \begin{pmatrix} 1 + 1\,\mathrm{e}^{i\theta_2} & 0 & \mathrm{e}^{i\theta_1} - \mathrm{e}^{i\theta_2}\mathrm{e}^{i\theta_1} & 0 \\ 0 & 1 + \mathrm{e}^{i\theta_2} & 0 & -\mathrm{e}^{i\theta_1} + \mathrm{e}^{i\theta_2}\mathrm{e}^{i\theta_1} \\ 0 & 1 - \mathrm{e}^{i\theta_2} & 0 & -\mathrm{e}^{i\theta_1} - \mathrm{e}^{i\theta_2}\mathrm{e}^{i\theta_1} \\ 1 - \mathrm{e}^{i\theta_2} & 0 & \mathrm{e}^{i\theta_1} + \mathrm{e}^{i\theta_2}\mathrm{e}^{i\theta_1} & 0 \end{pmatrix}$$

The state $|\psi\rangle$ is prepared to be the input to the upper line of the quantum circuit and $|+\rangle$, the input to the lower line. To be able to apply the 2-qubit unitary on these inputs at once, one takes the tensor product between them and call it *Input*.

$$\psi = \begin{pmatrix} \alpha \\ \beta \end{pmatrix}$$

$$plus = \frac{1}{\sqrt{2}} \begin{pmatrix} 1 \\ 1 \end{pmatrix}$$

$$Input = \frac{1}{\sqrt{2}} \begin{pmatrix} \alpha \\ \alpha \\ \beta \\ \beta \end{pmatrix}$$

The application of the *TwoQubitUnitary* on the *Input* results into the following state as the

output of the circuit

$$\frac{\sqrt{2}}{4}\begin{pmatrix} \left(1+e^{i\theta_2}\right)\alpha+\left(e^{i\theta_1}-e^{i\theta_2}e^{i\theta_1}\right)\beta \\ \left(1+e^{i\theta_2}\right)\alpha+\left(-e^{i\theta_1}+e^{i\theta_2}e^{i\theta_1}\right)\beta \\ \left(1-e^{i\theta_2}\right)\alpha+\left(-e^{i\theta_1}-e^{i\theta_2}e^{i\theta_1}\right)\beta \\ \left(1-e^{i\theta_2}\right)\alpha+\left(e^{i\theta_1}+e^{i\theta_2}e^{i\theta_1}\right)\beta \end{pmatrix} \tag{5.14}$$

The next section contains the simulation of the creation of the 4-qubit graph state. The output of the computation performed on the graph by measuring the polarization qubits with angles θ_1 and θ_2 is compared with the results obtained in the present section.

5.5 Simulation of Graph

This section explains how the experiment is simulated. Some portions of the code are recreated here. The complete Maple V code can be found in Appendix C.

In this simulation, the physical carriers of the logical qubits in the kets are organized in the order $|P_A K_A P_B K_B\rangle$, where P_A and K_A are the qubits carried on polarization and path DOFs of photon A and P_B and K_B are the qubits carried on polarization and path DOFs of photon B. The convention that is used is $|H\rangle = |0\rangle$, $|V\rangle = |1\rangle$, $|t\rangle = |0\rangle$ and $|r\rangle = |1\rangle$. The order of kets is the same as counting from 0 to 15 in binary and determines the meaning of the entries in the vector representing the 4-qubit state. For example, the first vector element is the coefficient of $|0000\rangle$, where 0000 is the binary 0. The second vector element is the coefficient of $|0001\rangle$, where 0001 equals 1 and the last vector element is the coefficient of $|1111\rangle$, where 1111 is the binary 15.

One starts by defining single qubit and 2-qubit operators. The operators for higher number of qubits are reconstructed by the tensor products of single qubit and 2-qubit operators.

5.5.1 Operator Definitions

Operator BS is defined as a general beam splitter. One can choose it to be a 50 : 50 beam splitter by choosing α_2 and β_2 equal to $1/\sqrt{2}$.

$$BS = \begin{pmatrix} \alpha_2 & \beta_2 \\ \beta_2 & -\alpha_2 \end{pmatrix}$$

A half-wave plate rotated by an angle θ is defined as:

$$HWP(\theta) = \begin{pmatrix} \cos(\theta)^2\, i - \sin(\theta)^2\, i & 2\, i \cos(\theta) \sin(\theta) \\ 2\, i \cos(\theta) \sin(\theta) & \sin(\theta)^2\, i - \cos(\theta)^2\, i \end{pmatrix}$$

Quarter-wave plate at angle θ is defined as:

$$\begin{pmatrix} \cos(\theta)^2 \left(\frac{\sqrt{2}}{2} + \frac{1}{2}\, i\, \sqrt{2}\right) - \sin(\theta)^2 \left(\frac{\sqrt{2}}{2} + \frac{1}{2}\, i\, \sqrt{2}\right) i & \cos(\theta) \left(\frac{\sqrt{2}}{2} + \frac{1}{2}\, i\, \sqrt{2}\right) \sin(\theta) + \sin(\theta) \left(\frac{\sqrt{2}}{2} + \frac{1}{2}\, i\, \sqrt{2}\right) \cos(\theta)\, i \\ \cos(\theta) \left(\frac{\sqrt{2}}{2} + \frac{1}{2}\, i\, \sqrt{2}\right) \sin(\theta) + \sin(\theta) \left(\frac{\sqrt{2}}{2} + \frac{1}{2}\, i\, \sqrt{2}\right) \cos(\theta)\, i & \sin(\theta)^2 \left(\frac{\sqrt{2}}{2} + \frac{1}{2}\, i\, \sqrt{2}\right) - \cos(\theta)^2 \left(\frac{\sqrt{2}}{2} + \frac{1}{2}\, i\, \sqrt{2}\right) i \end{pmatrix}$$

A set of controlled-HWP are defined for different qubits acting as target and control. These operations essentially apply the required controlled-Z and Hadamard to polarization and path qubits to form the loop graph.

$CHWP(\theta)$ is defined such that the control is qubit 1, logical 1 and the target is qubit 2.

$$CHWP(\theta) = \begin{pmatrix} 1 & 0 & 0 & 0 \\ 0 & 1 & 0 & 0 \\ 0 & 0 & \cos(\theta)^2\, i - \sin(\theta)^2\, i & 2\, i \cos(\theta) \sin(\theta) \\ 0 & 0 & 2\, i \cos(\theta) \sin(\theta) & \sin(\theta)^2\, i - \cos(\theta)^2\, i \end{pmatrix}$$

$ZCHWP(\theta)$ is defined such that the control is qubit 1, logical 0 and the target is qubit 2.

$$ZCHWP(\theta) = \begin{pmatrix} \cos(\theta)^2\, i - \sin(\theta)^2\, i & 2\, i \cos(\theta) \sin(\theta) & 0 & 0 \\ 2\, i \cos(\theta) \sin(\theta) & \sin(\theta)^2\, i - \cos(\theta)^2\, i & 0 & 0 \\ 0 & 0 & 1 & 0 \\ 0 & 0 & 0 & 1 \end{pmatrix}$$

$NCHWP(\theta)$ is defined such that the control is qubit 2, logical 1 and the target is qubit 1.

$$NCHWP(\theta) = \begin{pmatrix} 1 & 0 & 0 & 0 \\ 0 & \cos(\theta)^2\, i - \sin(\theta)^2\, i & 0 & 2\, i \cos(\theta) \sin(\theta) \\ 0 & 0 & 1 & 0 \\ 0 & 2\, i \cos(\theta) \sin(\theta) & 0 & \sin(\theta)^2\, i - \cos(\theta)^2\, i \end{pmatrix}$$

And finally, $NZCHWP(\theta)$ is defined such that the control is qubit 2, logical 0 and the target is qubit 1.

$$NZCHWP(\theta) = \begin{pmatrix} \cos(\theta)^2\, i - \sin(\theta)^2\, i & 0 & 2\, i \cos(\theta)\sin(\theta) & 0 \\ 0 & 1 & 0 & 0 \\ 2\, i \cos(\theta)\sin(\theta) & 0 & \sin(\theta)^2\, i - \cos(\theta)^2\, i & 0 \\ 0 & 0 & 0 & 1 \end{pmatrix}$$

An operator A is defined to apply the beam splitters to the path qubit of each photon, while applying Identity to the polarization qubits so that $A(a,b) = Id \otimes BS(a,b)$. Both photons should go through beam splitters, hence operator A should be applied to both path qubits. Also, as beam splitters are at the beginning of interferometers, one introduces ϕ_A and ϕ_B as the phases of interferometers that can be set to any desired value. This gives the operator $BSBS = A(\frac{1}{\sqrt{2}}e^{i\phi_A}, \frac{1}{\sqrt{2}}) \otimes A(\frac{1}{\sqrt{2}}e^{i\phi_B}, \frac{1}{\sqrt{2}})$.

Now one constructs the particular controlled operators to the loop graph. HWP_1 corresponds to a HWP at 22.5° at the transmitted arm of photon B. In the simulation, the target is qubit 3 and the control is qubit 4, logical 0, so $HWP_1 = Id \otimes Id \otimes NZCHWP(\frac{22.5\cdot\pi}{180})$.

HWP_2 corresponds to HWP at $-22.5°$ at the reflected arm of photon B. The target is qubit 3 and the control is qubit 4, logical 1, so $HWP_2 = Id \otimes Id \otimes NCHWP(\frac{-22.5\cdot\pi}{180})$.

HWP_3 corresponds to a HWP at 0° on the reflected arm of photon A. The target is qubit 1 and the control is qubit 2, logical 1, so $HWP_3 = NHWP(\frac{\pi}{2}) \otimes Id \otimes Id$.

The 4-qubit unitary operation that prepares the graph, GP, is constructed by consecutive application of the operators defined above to the input and is given by $GP = HWP_3 \cdot HWP_2 \cdot HWP_1 \cdot BSBS$.

The input is $\alpha_1|HtHt\rangle + \beta_1|VtVt\rangle$. The ket $|HtHt\rangle$ equals $|0000\rangle$, hence its coefficient α_1 is the first entry in the vector representation the input and the ket $|VtVt\rangle$ equals $|1010\rangle$, that is 10 in binary, hence its coefficient β_1 is the 11th entry of the vector called *input*

$$input = Vector(alpha1, 0, 0, 0, 0, 0, 0, 0, 0, 0, 0, beta1, 0, 0, 0, 0, 0)$$

The graph is then constructed by applying GP to the input, such that $graph = GP \cdot input$.

It turns out that choosing $\phi_A = \frac{3\pi}{2}$ and $\phi_B = 0$ correspond to maximizing both interferometers on D. The density matrix of the graph state, CD, is constructed by $CD = graph.HermitianTranspose(graph)$.

General formulae for measurement rotations

For measuring the polarization qubits, P_1 and P_2, in our experiment, the detectors are set at the output ports of the PBSs that see horizontal polarization. This output port is simulated by matrix H. *MHH* defines the application of PBSs to polarization of both photons:

$$H = \begin{pmatrix} 1 & 0 \\ 0 & 0 \end{pmatrix}$$

and $MHH = \frac{2}{\sqrt{2}} H \otimes Id \otimes H \otimes Id$.

In order to carry on the quantum computation, P_1 is measured by angle θ_1 and P_2 by angle θ_2. $J(\theta)$ is the operation applied to these qubits before they go through PBSs:

$$J(\theta) = \begin{pmatrix} \frac{\sqrt{2}}{2} & \frac{1}{2}\sqrt{2}\, e^{(\theta\, I)} \\ \frac{\sqrt{2}}{2} & -\frac{1}{2}\sqrt{2}\, e^{(\theta\, I)} \end{pmatrix}.$$

Jtheta1Jtheta2 is the 4-qubit operator that applies $J(\theta_1)$ and $J(\theta_2)$ to P_1 and P_2 and is constructed by $Jtheta1Jtheta2(\theta_1, \theta_2) = J(\theta_1) \otimes Id \otimes J(\theta_2) \otimes Id$.

Measuring the polarization qubits consists of applying the J operators, followed by PBSs. The combination of *MHH* and *Jtheta1Jtheta2* does this job: $JJHG = 2 \cdot MHH \cdot Jtheta1Jtheta2(\theta_1, \theta_2) \cdot graph$. The result of the computation, which is the state of the two path qubits, is

$$Result = \frac{\sqrt{2}}{4} \begin{pmatrix} -\beta_1 e^{i(\theta_1+\theta_2)} + \alpha_1 + e^{i\theta_2}\alpha_1 + e^{i\theta_1}\beta_1 \\ -\beta_1 e^{i(\theta_1+\theta_2)} + \alpha_1 - e^{i\theta_2}\alpha_1 - e^{i\theta_1}\beta_1 \\ \beta_1 e^{i(\theta_1+\theta_2)} + \alpha_1 + e^{i\theta_2}\alpha_1 - e^{i\theta_1}\beta_1 \\ \beta_1 e^{i(\theta_1+\theta_2)} + \alpha_1 - e^{i\theta_2}\alpha_1 + e^{i\theta_1}\beta_1 \end{pmatrix}.$$

It matches the result from the circuit model shown in equation 5.14 when one takes into account the order of qubits. Here, the first qubit in the ket is K_1 and the second is K_2, while for the results of the circuit, this order is reversed. Thus, to be able to compare these two results, one should exchange the second and third entries in the vector. Doing this, we see that the results are identical.

Tomography Results for Path Qubits

After the preparation of the graph, it is desirable to know what state of path qubits are expected from the setup for each setting of tomography basis for polarization qubits. One

first defines the combination of QWP and HWP for each tomography setting, then continues to study the effect of these measurements on the graph.

To compare the results of the simulation with the experiment, the same input in the simulation as the experiment is used, which is the state $|+\rangle$. So α_1 and β_1 are set, accordingly, to $1/\sqrt{2}$.

The measurement bases are as follows. The rotation that takes H to H is

$$RHH = HWP(\frac{0 \cdot \pi}{180}) \cdot QWP(\frac{0 \cdot \pi}{180})$$

The rotation that takes V to H is

$$RVH = HWP(\frac{45 \cdot \pi}{180}) \cdot QWP(\frac{0 \cdot \pi}{180})$$

The rotation that takes D to H is

$$RDH = HWP(\frac{22.5 \cdot \pi}{180}) \cdot QWP(\frac{45 \cdot \pi}{180})$$

The rotation that takes A to H is

$$RAH = HWP(\frac{67.5 \cdot \pi}{180}) \cdot QWP(\frac{45 \cdot \pi}{180})$$

The rotation that takes L to H is

$$RLH = HWP(\frac{67.5 \cdot \pi}{180}) \cdot QWP(\frac{0 \cdot \pi}{180})$$

The rotation that takes R to H is

$$RRH = HWP(\frac{22.5 \cdot \pi}{180}) \cdot QWP(\frac{0 \cdot \pi}{180})$$

Measurement Results of Graph with No Errors

We have performed the experiment by post-selecting on the results of measurements of qubits 1 and 2, which are the polarization qubits, to be 0. The post-selection, in our experiment, replaces the implementation of the feed-forward mechanism. The only reason we could make such replacement is that we are using a small graph, which does not give rise to a very high cost of computation. It is worth mentioning that this post-selection has nothing to do with the required post-selection for simulating time-like curves using the Bennett, Schumacher and Svetlichny method. Their post-selection is an inevitable consequence of using quantum teleportation, while the post-selection in our experiment is to force the one-way

computation to a deterministic pattern. We could have avoided post-selection by applying the feed-forward.

In the following, one first measures the polarization qubits in various bases that are used for state tomography. One then finds the 2-qubit density matrix of the state of path qubits associated to each setting of polarization qubits.

In order to measure the polarization qubits in *HH* basis, one should apply the rotation that takes H to H on these qubits. *HH16* is the 4-qubit operator that performs this transformation and is constructed by $HH16 = RHH \otimes Id \otimes RHH \otimes Id$.

The polarization qubits are measured by applying the complete measurement operator, with proper normalization, to the graph density matrix (Nielsen et Chuang, 2000), which is given by

$$HHCD = \frac{MHH \cdot HH16 \cdot CD \cdot HermitianTranspose(HH16) \cdot HermitianTranspose(MHH)}{Trace(HermitianTranspose(MHH) \cdot HermitianTranspose(HH16) \cdot CD \cdot HH16 \cdot MHH)}.$$

One applies the similarly constructed operators for other measurement bases. The results for various measurement bases and the complete Maple code is in Appendix C. In Appendix **??**, these results are summarized and compared with the results from the experiment.

The expected results of three different computations using the loop graph are also simulated. Each computation corresponds to a different choice of measurement angles of qubits 1 and 2. These choices are $\theta_1 = \theta_2 = 0$, $\theta_1 = \theta_2 = \frac{\pi}{2}$ and $\theta_1 = 0$, $\theta_2 = \frac{\pi}{2}$. The results of these computations and their comparison with the experimental results are also given in Appendix **??**.

5.5.2 Error analysis arising from state preparation

This section presents the effects of errors originating from three different sources, namely, inaccurate setting of waveplate angles in state preparation, error in retardance of these waveplates and inaccuracy in the phase setting of the interferometer.

To carry on this error analysis, one uses the general formulas for waveplates and define all gates using these formulas. The code is detailed in Appendix D.

There are three waveplates (WP) that prepare the state. One of these WPs should be set at $0°$, one at $22.5°$ and the third one at $-22.5°$. The effect of having $\pm 2°$ error in each of these waveplates is studied. One calculates the purity and the fidelity of the created state with that of the target state, which is the state of the perfect 4-qubit loop graph, for each waveplate settings. The calculations show that the purity of the state is not affected by these errors. However, the fidelity changes with the error, as is shown in the graph of Fig. 5.6.

We have chosen $\pm 2°$ as the maximum possible error in these angles due to the practical

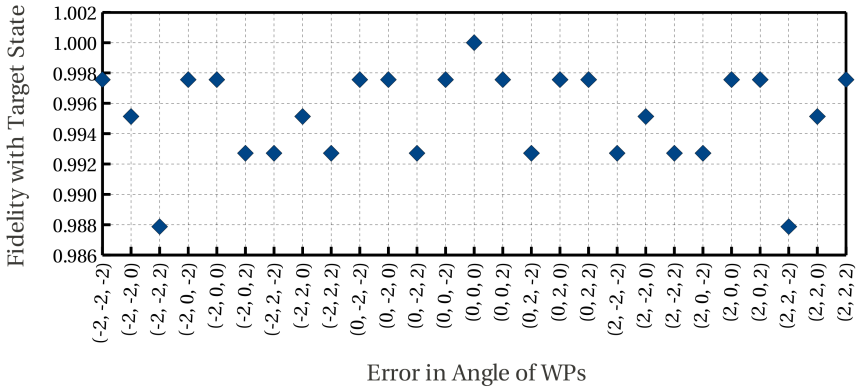

Figure 5.6 The effect of WP angle error on the created state. The triplets on the x axis correspond to $(\Delta\theta_1, \Delta\theta_2, \Delta\theta_3)$, where $\Delta\theta_1$ is the error in the angle of $HWP(22.5)$ of Fig. 5.2, $\Delta\theta_2$ is the error in the angle of $HWP(-22.5)$ and $\Delta\theta_3$ is the error in the angle of $HWP(0)$.

precision that could be obtained experimentally, given the waveplate mounts that were used. These mounts have $\pm 2^\circ$ uncertainty. One can see that even the worst case does not reduce the fidelity of the state by much more than 1%.

The WPs from various companies can have an error of up to a few percent in their retardance. Upon calibration of our WPs, we realized that the maximum error in their retardance is 2%. Again, the calculations showed that these errors do not reduce the purity of the state. Fig. 5.7 shows the fidelity of the created state with that of the target state.

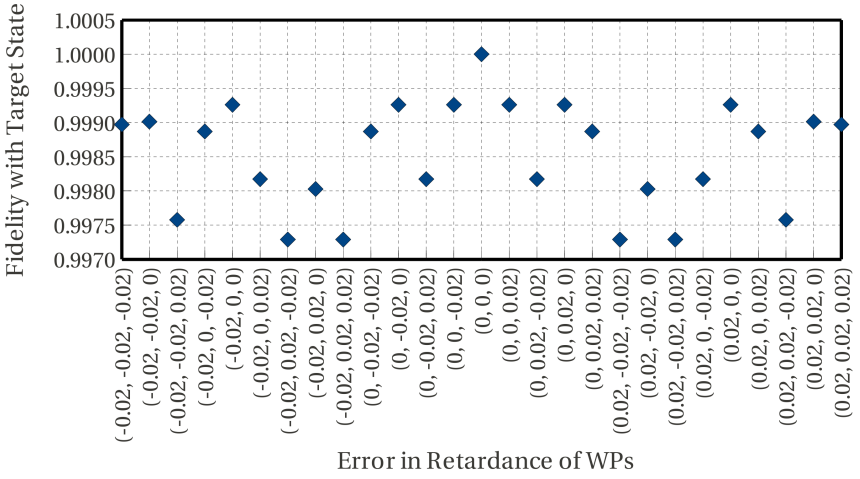

Figure 5.7 The effect of WP retardance error on the created state. The triplets on the x axis correspond to $(\Delta\phi_1, \Delta\phi_2, \Delta\phi_3)$, where $\Delta\phi_1$ is the percentage error of the retardance of $HWP(22.5)$ of Fig. 5.2, $\Delta\phi_2$ is that of $HWP(-22.5)$ and $\Delta\phi_3$ is the percentage error in retardance of $HWP(0)$.

This data shows that the error in the retardances of our WPs introduce only a negligible

amount of error in the created state, as the fidelity with the target state remains at 99%.

In previous sections, we explained how set the phase of the interferometers were set to the correct value. However, various factors give rise to errors in setting this phase. As it was explained before, we first minimize the output number of photons from one port of the interferometer, while the QWP and HWP of path tomography (encased in a dashed box in Fig. 5.5) are set to measure in $\bar{D}$ basis. Then we change the basis to R/L and try to set the number of photons to half of their maximum count per second. However, the fluctuations in the number of photons make it hard to determine the exact count of photons. Also, the possible errors in the setting of the QWP and HWP mean that the marking at half of the maximum counts could be adjusted for the wrong basis. The error in the waveplates can give rise to up to 10% error in the value of the phase we try to set. This value is found by setting the phase of each interferometer to maximize on basis D, such that one would expect horizontally polarized input light to exit the interferometer at state $(|t\rangle +^{\phi} |r\rangle)/\sqrt{2}$, with $\phi = 0$. We then sent a classical beam through each interferometer and performed single qubit tomography on the output path qubit. It was found that ϕ can have up to about 10% error from the expected value. In these simulations $\pm 10\%$ error is introduced to obtain the upper bound of error introduced in state preparation from the wrong value for the phases of both interferometers. It is found that these errors do not change the purity of the state. Fig. 5.8 shows the fidelity of the created state with that of the target state. It is interesting

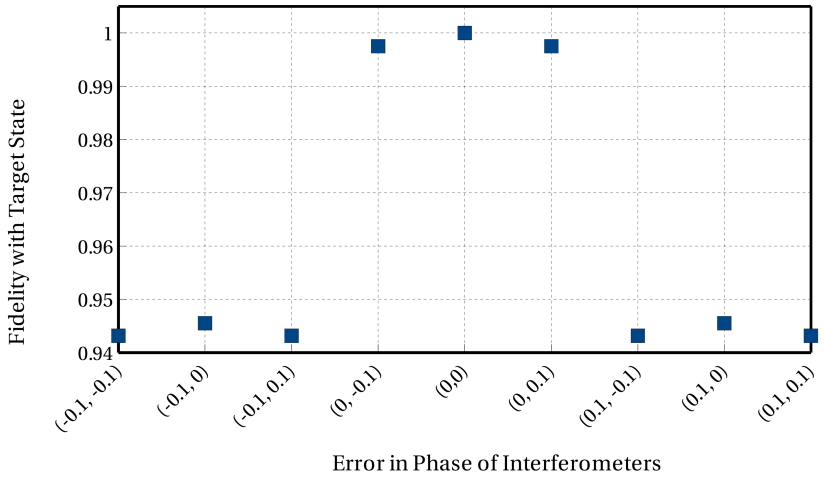

Figure 5.8 The effect of a wrong setting of phases of both interferometers on the created state. The doublets on the x axis correspond to $(\Delta\eta_1, \Delta\eta_2)$, where $\Delta\eta_1$ is the percentage error of the phase of interferometer A and $\Delta\eta_2$ is that of interferometer B.

to see that the phase errors of both interferometers induce the same amount of error in the fidelity of the created state and it is not the case that the state is more sensitive to the phase

of one interferometer than the other. Also, the error in these phases seems to be a major cause of fidelity loss with the target state, as the fidelity can go as low as 94%.

We have performed the calculations combining the effects of all these errors. The maximum amount of the combined errors reduces the fidelity of the created state with the target state to 93%.

In the next chapter, we go through the details of the properties of our experimental setup and the results.

Chapter 6

Experimental Setup: Details and Results

In this chapter, the details of the experimental setup and its properties are explained. We begin by explaining the source of polarization entangled photons, then talk about polarization correction of photons, which is required due to their travelling in single mode fibers. The procedure to align the interferometers and the optical elements therein is presented. The interferometers are characterized in terms of their stabilities, visibilities and losses. The methods for calibrating waveplates and state tomography are clarified. The final section reports on the results of the experiment.

6.1 Source of Entangled Photons

The source of entangled photons consists of a periodically-poled potassium titanyl phosphate (PPKTP) crystal in a cavity (Fig. 5.1). The pump beam for spontaneous down-conversion (SPDC), which is at 390 nm wavelength, is produced using Second Harmonic Generation (SHG) in a PPLN crystal in a cavity. The pump for SHG is a Toptica laser at 780 nm wavelength, locked to the F3 to F4 transition line of Rubidium 85 atoms. The down-conversion is done through collinear degenerate phase matching type II. There is a KTP crystal in the cavity to compensate for the temporal walk-off due to group birefringence of the PPKTP crystal. A Michelson interferometer outside the cavity provides further compensation for this temporal walk-off. This interferometer separates the two polarizations into two different paths by a polarizing beam-splitter (PBS). A mirror on a translation stage at the end of each path retro-reflects the light back on its ingoing path. A quarter-wave plate (QWP) at each path flips the polarizations such that the reflected beams can recombine into one spatial mode through the same PBS that separated them from each other. This way, the optical path for each polarization can be adjusted independently using the mirrors on translation stage. The photons continue on this spatial path until they are separated into two paths using a beam splitter. As the phase matching is of type II, the polarization state of the photons, once they are separated into two spatial paths, is $(|HV\rangle + |VH\rangle)/\sqrt{2}$.

Altogether, in this source, there are two cavities which are actively stabilized, one for SHG and one for SPDC. The locking of these cavities is very sensitive to temperature, hence it is difficult to keep a stable lock for long periods of time. For the data reported here, the lock of the SPDC cavity had to be adjusted about every 15 minutes, while the lock of the SHG had to be adjusted every few hours. In addition, there are three different temperature controllers for the three crystals: the PPLN, the KTP and the PPKTP. The drift in the temperature of the PPKTP and KTP reduces the purity of the polarization entangled pairs of photons. Hence, those temperature had to be adjusted every few hours. Note that for the experiment we are reporting here, such a sophisticated source is not a necessity. The source is designed for light-atom interaction experiments. In this experiment, we take advantage of the relatively long coherence length of the photons, which is about 2mm.

The photons from this source were collected into two single mode optical fibers (SMF) and transfered to another optical table which contained the setup for the loop graph experiment. The SMFs apply a random unitary operation on the polarization of each photon, it therefore is necessary to apply corrections on the polarization states of photons exiting these fibers. The correction is done by a series of QWP, half-wave plate (HWP), QWP located after the output of SMFs. Two silver mirrors on flip mounts pick up the light exiting the fibers and send them to a setup for polarization tomography, shown in Fig. 6.1. In order to do the

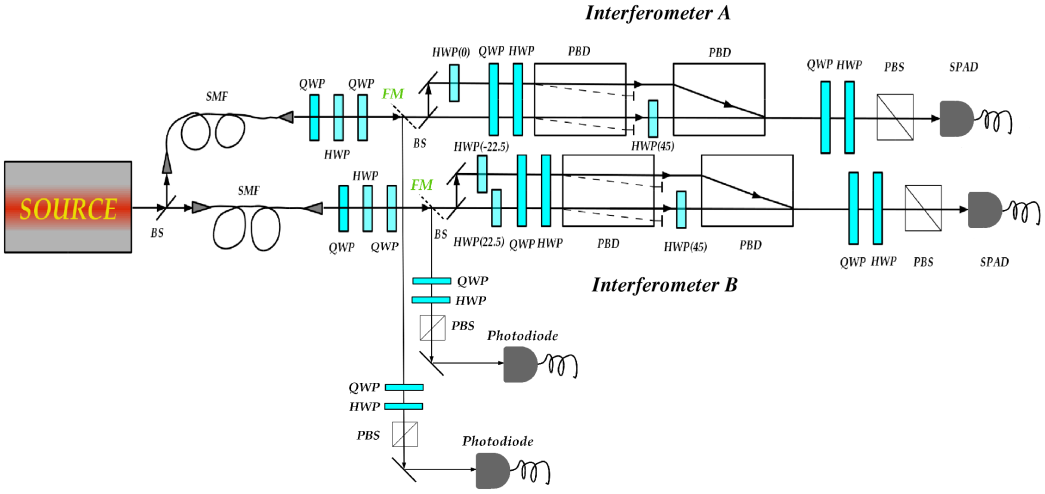

Figure 6.1 Schematic view of the experimental setup. The silver mirrors labeled FM are mounted on flip mounts such that the beams can be picked out before entering the setup, sending them to a tomography setup for polarization correction of fibers and two qubit tomography of the polarization state of photons from the source.

polarization correction, we treat each optical fiber separately and use laser beams, not single photons, to perform the necessary measurements. The SMF applies a single qubit unitary

operation on the polarization state of the light entering it. This operation is described by a 2×2 matrix with three parameters to be determined. Two different input states are alternatively injected into the fiber. Single qubit tomography is performed for each state, as was described in chapter 5.2, to reconstruct the state of the output light. The chosen input states are horizontal and right-circular polarized light. This way, one has two equations

$$J_{\mathrm{OUT_H}} = U J_{\mathrm{H}}$$
$$J_{\mathrm{OUT_R}} = U J_{\mathrm{R}}$$

that completely determine the unitary matrix U, where J_{H} and J_{R} are Jones vectors representing the two input states used. To identify the polarization correction, the inverse matrix U^{-1} is written as a combination of waveplates (QWP-HWP-QWP), each with a specified rotation, providing the three parameters required.

In practice, the locking beam for the SPDC cavity is used as an input to the SMFs. The horizontally polarized beam is prepared by simply blocking one arm of the polarization Michelson interferometer and allowing only horizontal polarization to get through to the SMFs. To prepare the right circular polarized state, a QWP and a HWP in motorized mounts are used. At the output, a QWP and a HWP followed by a PBS perform the single qubit tomography. The polarization state of the beam is measured in H/V, A/D and R/L bases. One important aspect to keep in mind is the effect of the mirrors that pick up the beam after SMFs. We need the polarization state of photons after the SMFs, without the presence of these mirrors, to be $(|HH\rangle + |VV\rangle)/\sqrt{2}$. The mirror effectively applies a π phase shift between the vertical and horizontal components because of the change of direction of the $\vec{k}$ vector after the beam is reflected off the mirror. The mirror does not change the state if it is horizontal or vertical but right-circular changes to left-circular after the mirror. For one of the SMFs, the unitary operation is corrected such that it takes a horizontal input to a horizontal output and a right-circular input to a left-circular output. For the second SMF, the correction is such that it takes a horizontal input to a vertical output and a right-circular input to a right-circular output. This is done so that the input state to the SMFs $(|HV\rangle + |VH\rangle)/\sqrt{2}$ becomes $(|HH\rangle + |VV\rangle)/\sqrt{2}$ at the output. The path of the second SMF applies a bit-flip; a bit flip on right-circular polarization, gives a left-circular polarized beam, which becomes right-circular after it is reflected off the flip mirror to the polarization measurement setup.

After the polarization correction is completed, quantum state tomography is performed on photons created by the source. The entangled state $(|HH\rangle + |VV\rangle)/\sqrt{2}$ should remain unchanged after reflection by both flip mirrors. It was found that this was not the case when

dielectric mirrors were first used. After much investigation, it was realized that dielectric mirrors affect the polarization state in unwanted ways. By the way they are fabricated, they may apply a significant phase shift between the H and V polarization states. Changing those them to silver mirrors resolved the issue.

Depending on the temperature conditions of the source, we obtain different results. The density matrix corresponding to the target state is

$$\text{Source}_{\text{Target}} = \begin{pmatrix} 0.5 & 0 & 0 & 0.5 \\ 0 & 0 & 0 & 0 \\ 0 & 0 & 0 & 0 \\ 0.5 & 0 & 0 & 0.5 \end{pmatrix}. \tag{6.1}$$

The state emitted by the source, measured after the SMFs and on the same night as quantum state tomography data, is found to have a purity of 0.88 and to be described by the following density matrix by using the method of Linear Inversion

$$\text{Source}_{\text{LI}} = \begin{pmatrix} 0.5467 & -0.0227+0.0270i & -0.0601-0.0421i & 0.4073-0.1698i \\ -0.0227-0.0270i & 0.0118 & -0.0321-0.0054i & -0.0037+0.0042i \\ -0.0601+0.0421i & -0.0321+0.0054i & 0.0239 & 0.0308+0.0138i \\ 0.4073+0.1698i & -0.0037-0.0042i & 0.0308-0.0138i & 0.4176 \end{pmatrix}. \tag{6.2}$$

Reconstructing the density matrix using the method of Maximum Likelihood results into

$$\text{Source}_{\text{MLH}} = \begin{pmatrix} 0.5395 & -0.0235+0.0229i & -0.0458-0.0361i & 0.3919-0.1710i \\ -0.0235-0.0229i & 0.0111 & 0.0042+0.0160i & -0.0026+0.0084i \\ -0.0458+0.0361i & 0.0042-0.0160i & 0.0249 & 0.0112+0.0184i \\ 0.3919+0.1710i & -0.0026-0.0084i & 0.0112-0.0184i & 0.4245 \end{pmatrix}. \tag{6.3}$$

The real and imaginary parts of this density matrix are plotted in Fig. 6.2. This result has a

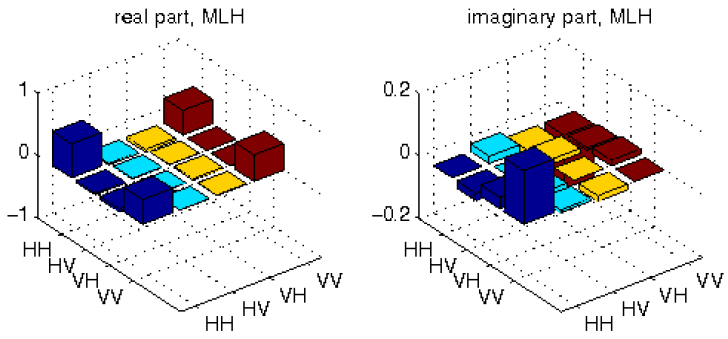

Figure 6.2 The real and imaginary parts of the reconstructed density matrix using Maximum Likelihood. The density matrix corresponds to the state of the photons after single mode fibers, with purity 0.85 and fidelity of 0.87.

purity of 0.85 and a fidelity of 0.87 with the target state. Appendix E presents a simulation of

the creation of the 4-qubit state when the input is this density matrix instead of the perfect target state.

The state emitted from the source, measured on the same night as data for quantum computation, using the method of Linear Inversion, has purity of 0.87 and is

$$\text{Source}_{\text{LI}} = \begin{pmatrix} 0.5288 & -0.0232 - 0.0245i & -0.0399 + 0.0281i & 0.4271 + 0.0266i \\ -0.0232 + 0.0245i & 0.0192 & -0.0392 - 0.0117i & 0.0116 + 0.0081i \\ -0.0399 - 0.0281i & -0.0392 + 0.0117i & 0.0000 & 0.0214 - 0.0516i \\ 0.4271 - 0.0266i & 0.0116 - 0.0081i & 0.0214 + 0.0516i & 0.4520 \end{pmatrix}. \tag{6.4}$$

Reconstructing the density matrix using the method of Maximum Likelihood results into

$$\text{Source}_{\text{MLH}} = \begin{pmatrix} 0.5082 & -0.0148 - 0.0403i & -0.0130 + 0.0334i & 0.4238 + 0.0250i \\ -0.0148 + 0.0403i & 0.0189 & 0.0000 - 0.0018i & -0.0024 + 0.0059i \\ -0.0130 - 0.0334i & 0.0000 + 0.0018i & 0.0032 & -0.0064 - 0.0370i \\ 0.4238 - 0.0250i & -0.0024 - 0.0059i & -0.0064 + 0.0370i & 0.4697 \end{pmatrix}. \tag{6.5}$$

The real and imaginary parts of this density matrix are plotted in Fig. 6.3. This result has

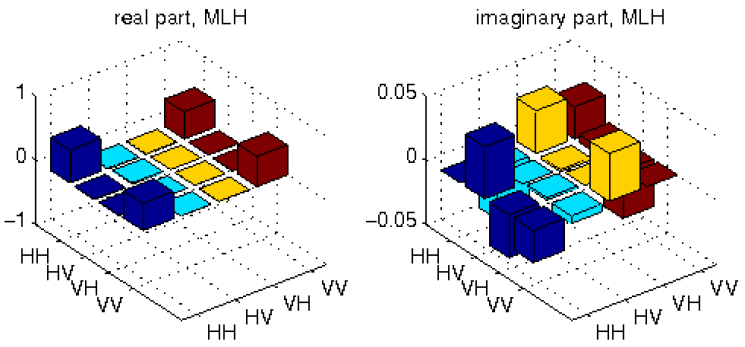

Figure 6.3 The real and imaginary parts of the reconstructed density matrix using Maximum Likelihood. The density matrix corresponds to the state of the photons after single mode fibers, with purity 0.85 and fidelity of 0.91

a purity of 0.85 and a fidelity of 0.91 with the target state.

6.2 Four-Qubit State Tomography

Tomography requires careful calibration of the waveplates. This is to find out the location of the fast axis in the rotating mount and also the accuracy of the retardance of each waveplate. The calibration is done by sandwiching the waveplate that is to be calibrated between two polarization beam splitters that are aligned with the optical table to transmit horizontal polarization, as shown in Fig. 6.4. The PBSs are aligned such that the beam leaving the reflection port is parallel to the optical table, and the reflection from the first face of the PBS goes falls back on the same path the incoming beam took. This alignment procedure assures

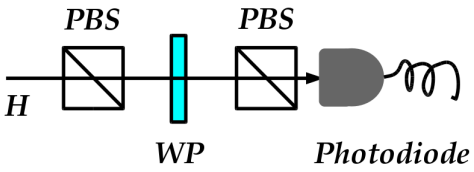

Figure 6.4 The setup for calibration of waveplates. The waveplate that is to be calibrated is sandwiched between two polarization beam splitters. Inputing horizontally polarized light and rotate the waveplate gives rise to a sinusoidal curve at the output of the second PBS. In general, the location of maximum of this curve determines where the fast or slow axis is, and its amplitude determines the retardance of the waveplate. We have measured the distance between maximums, which is 45° in the ideal case, to determine the proper amount of rotation for each basis setting for tomography.

the practical definition of *horizontal* with respect to the optical table. The waveplates used for state tomography on the source are the same as the ones used for path tomography and are mounted in motorized mounts. Each is rotated by 180 degrees and the intensity of light that gets transmitted through the second PBS is recorded, which is a sinusoidal curve. Using Origin, we fit this curve to the function

$$y = y_0 + A \sin\left[\frac{\pi(x - x_c)}{w}\right]$$

and from there we obtain the location of the fast or slow axis using

$$\theta_{FS} = \frac{w}{2} + x_c$$

and the exact amount of rotation it takes to go from one maximum to another, which equals the value of w. For a perfect waveplate, this value is 45°, we find values that are different by about 1%. Also, be measuring the amplitude of these curves we find the retardance of waveplates is accurate within 1% of what they should be.

For a HWP, the effect of fast and also slow axis are the same, hence finding one of those is sufficient, however for QWPs it is important to make the distinction between fast and slow axis. To do so, each QWP is compared with one whose location of fast axis was marked from the company. Both QWPs are sandwiched inbetween two PBSs such that the location of the fast or slow axis that is found on the waveplate being calibrated is parallel to the fast axis of the waveplate from the company. If the axis of the WP under going calibration is the fast axis, then along with the other QWP, they act like a HWP, and rotating both of them together gives a sinusoidal curve as output. If the axis of the WP being calibrated is the slow axis, then it cancels the effect of the known WP and upon rotation of both WPs together

one obtains a straight line as output. The correct position of the fast axis of each QWP is marked properly using this method.

The waveplates that are used for doing state tomography on polarization qubits, two of which are marked in Fig 5.5, are mounted in regular Thorlabs rotation mounts and are set by hand. The location of the fast or slow axis of these waveplates is found by determining the two angles θ_1 and θ_2 that fall on two sides of the angle that corresponds to the maximum transmission of light through the second PBS as shown in Fig. 6.5, hence is the fast or slow axis. The location of this axis is thus found from the formula $\theta_{\text{fast/slow}} = \theta_1 + \frac{\theta_2 - \theta 1}{2}$.

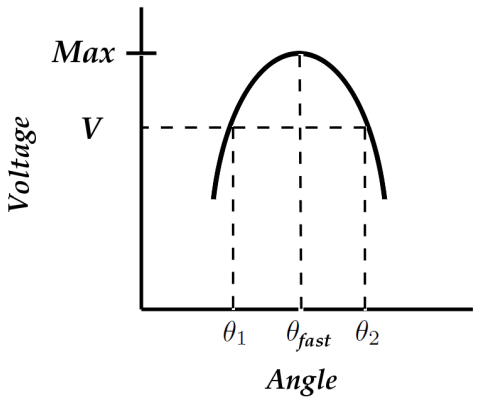

Figure 6.5 Determining the position of the fast or slow axis of waveplates in a manual rotation mount. One finds two angles θ_1 and θ_2 that are on two sides of the maximum output and correspond to the same intensity of light, which is marked as voltage here, since the photo diodes output voltage. The fast or slow axis is then found by the formula described in the text.

6.2.1 Interferometer Alignment, Stability and Visibility

The polarization beam displacers (PBDs) that are used for the setup that creates and measures the loop graph are from Thorlabs and they displace the extraordinary beam at 780 nm by about 4 millimeters. The first PBD is aligned to displace vertically polarized light. When a beam with some polarization other than H or V enters the interferometer it becomes two parallel beams, one that gets transmitted through the beam splitter (BS) and the other one that is reflected by the BS and the mirror. When these two beams enter the PBD, the extraordinary beam gets displaced down, so one sees four bright spots after the PBD. By making sure these four spots make a perfect square, one guarantees that the extraordinary beam corresponds to vertically polarized light within acceptable experimental limitations.

The second PBD that closes the interferometer is aligned with the PBS that is used for path tomography. The PBSs themselves are aligned in the same way that the PBSs for waveplate calibrations were aligned. To align the PBD with the PBS coming after it, one should make sure they both see the same definition of horizontally polarized light. So the transmitted arm of the interferometers are blocked to allow only horizontally polarized light to reach the second PBD and the PBD is rotated to allow maximum transmission from the PBS which is after it. This means the PBD is displacing almost all of the light to the correct path that goes to the PBS, hence it is at an orientation at which it sees the horizontally polarized light as extraordinary, which is the orientation desired for this PBD to properly close the interferometer.

The setup of the loop graph is set on an aluminum plate, since it includes two interferometers. The plate is connected to the optical table by five solid bases. The optical table is not floating. Using 3 and 4 connections to the table were tried, but at the end 5 connections at odd places resulted into the most stable interferometers, which are passively stabilized.

The stabilities of both interferometers were measured over many hours by setting their phases at the most steep part of the fringe, which is the most sensitive to phase changes, using the method described in chapter 5.3.1. Figures 6.6 and 6.7 show the results for about 10 minutes using single photons. The phase drift over longer times that 10 minutes follows the same trend. The amplitude of the visibility fringe of interferometer A is $12000 - 700 = 11300$,

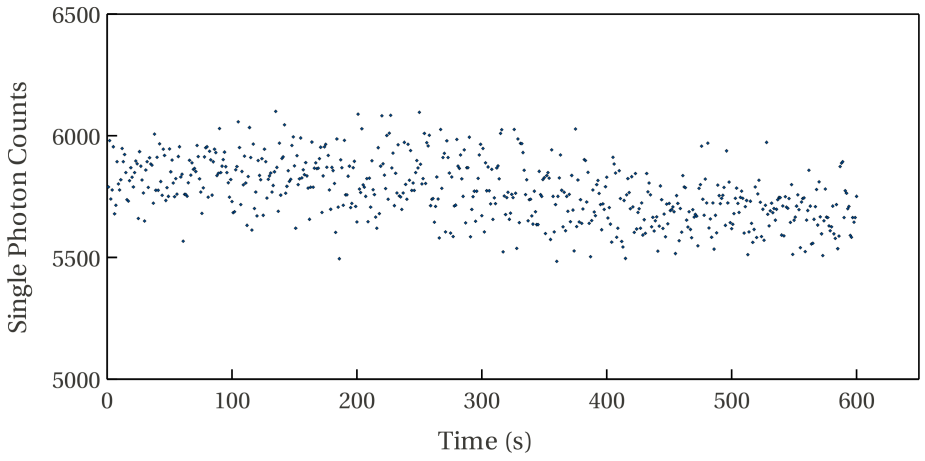

Figure 6.6 The stability of interferometer A in 10 minutes. The total fluctuation is by 5.3% of a half a fringe or π.

where 12000 counts per second is the maximum of the fringe and 700 counts per second is the minimum. The change of counts in 10 minutes is from 5484 to 6084. The change in half a fringe or in π can thus be approximated by $\frac{6084-5484}{12000-700} = 0.053$. The amplitude of the visibility

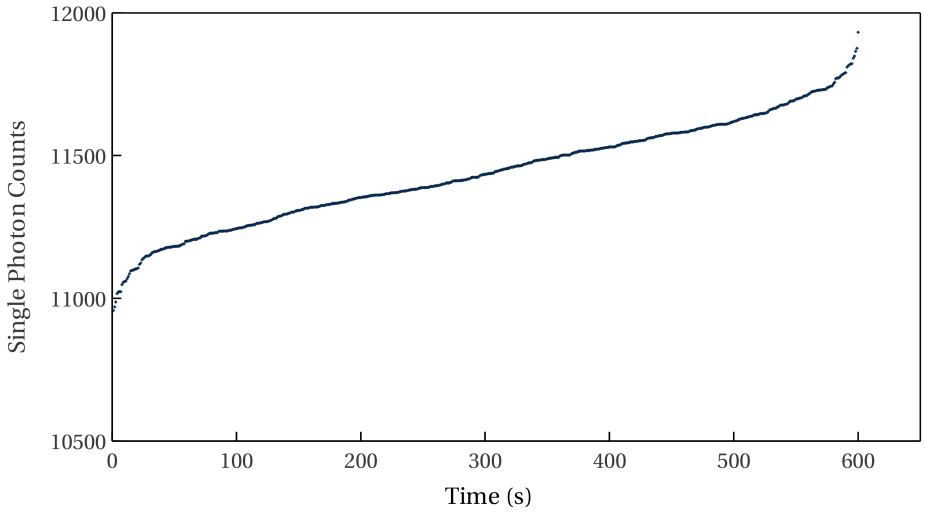

Figure 6.7 The stability of interferometer B in 10 minutes. The total fluctuation is by 4.9% of a half a fringe or π.

fringe of interferometer B is $21000 - 1250 = 19750$, where 21000 counts per second is the maximum of the fringe and 1250 counts per second is the minimum. The change of counts in 10 minutes is from 10957 to 11932. The change in half a fringe or in π is approximated to be $\frac{11932-10957}{21000-1250} = 0.049$. It takes about 10 minutes to take the 16 necessary measurements of the path qubits for each setting of polarization qubits. The phase of the interferometers are manually adjusted at about every 20 minutes or more frequently, as was needed.

The interferometers were first aligned to maximize the visibility of fringes for horizontally polarized laser beams. However, the coherence length of the laser beam is longer than the coherence length of single photons. Microscope slides and microscope slide cover glasses are used to balance the paths for single photons. The thickness of glass that was added to the paths was different for each interferometer and was essentially found by trial and error. At the end, the visibility of the interferometers for the laser beam was about 96% to 98% and for single photons was about 93% to 95%. The visibility being lower than the perfect 100% by 5% to 7% reduces the purity of output density matrices by the amount shown in simulations of Appendix E. Every time, before taking data and every couple of hours through taking data the visibility of interferometers for single photons are checked as sometimes one of the interferometers suddenly lost its high visibility and needed to be realigned.

To check the visibility of single photons, one should be sure that the ingoing photons are horizontally polarized by blocking one arm of the Michelson interferometer. If the arm is not blocked, the visibility seen for a single photon for interferometer B is reduced to almost zero, because the waveplates that create the graph state in this interferometer are set at

22.5° and −22.5°, hence rotate the horizontal and vertical portions of the polarization of each photon to diagonal and anti-diagonal. The polarization beam displacer then picks up the horizontal components of these polarizations, but as the phase of the interferometer changes, the fringe resulting from the horizontal component coming from horizontal portion of the photon have the opposite phase of the fringe resulting from the horizontal components coming from vertical portion of the photon, hence they cancel each other and give a fringe visibility of zero.

Imperfect beam splitter and the presence of different optical elements, especially the microscopes slides introduce different losses in different arms of each interferometer. In the ideal case, the outputs from each arm would have exactly the same intensity, which would equal 50% of the total intensity. This would give the perfect path qubit, in state $(|t\rangle+|r\rangle)/\sqrt{2}$. In practice, the transmitted arm of interferometer A transmits 40% of the power and its reflected arm, 60% of it. In interferometer B, the transmitted arm transmits 46% of the power and the reflected arm 54% of it. In Appendix E, the effect of this unbalanced loss in the interferometers on the created state, when the input state to the interferometers is the realistic density matrix obtained for the source from the method of Maximum Likelihood is simulated. The fidelities of these simulated results with the target states are reported in Fig. 6.12.

6.2.2 Measurement and Accidentals Subtraction

In order to perform tomography on all 4 qubits, one first sets the measurement basis for polarization qubits by the waveplates that are mounted in manual rotation mounts to certain basis, for example HH. Then perform the 16 measurements necessary for state tomography on path qubits. Then change the measurement of polarization qubit and repeat the 16 measurements on path qubits. This way 16×16 measurements are performed. These measurement settings are required because only two single photon detecting modules are being used, as the data is being collected only from one output port of each of the two PBDs and two PBSs. The need for interferometric stability and the inconsistency in the output of the source, due to the sensitivity of its various cavity locks to temperature, limits the time one can collect data to 15 seconds per measurement basis. The number of coincidence counts per second from a SPDC source follows a Poisson distribution and has an error of $\frac{\sqrt{N}}{N}$, where N is the total number of coincidence counts for each basis setting. For this experiment, one has an average of 300 coincidence counts in 15 seconds, which gives an error of about 6% in the coincidence counts for each basis setting. This error is inherent is all results reported here.

In order to construct the density matrices, one should subtract the accidental counts from

the coincidence counts. The accidental coincidences are the counts that come from higher number states and back ground photons in the lab, which are the inevitable result of the SPDC process. The accidentals are found by

$$\text{Accidentals} = \frac{S_1 \times S_2 \times \tau \times 4 \times 0.96}{t} \tag{6.6}$$

where S_1 is the singles count in detector 1, S_2 is the singles count in detector 2, τ is the coincidence window, *i.e.* the length of time the electronics looks for a coincidence count and t is the total time of collecting data. The coincidence window in our setup is set at 190 ns, to allow for both photons of the pair to complete their cavity round trips and exit the cavity.

The source uses a chopper before the SPDC cavity to actively lock this cavity. At the moments the chopper is allowing the laser beam to go through the cavity to adjust the lock, it blocks the path of the SPDC result to prevent the laser beam to enter the single photon detectors. So when we count the singles per second, in fact we are not counting for the whole second, but we are counting for the duration of the time that the chopper is allowing the result of SPDC to get to the detectors during each second. This duration is determined by the duty cycle of the chopper, which is about 1/4, hence τ is multiplied by 4. To determine the duty cycle more accurately an electronic delay line is used to experimentally measure the value of the accidentals. The delay line introduces a delay to one photon and should be more than 190 ns, in this case it is more than 250 ns. This delay guarantees that any coincidences that are measured cannot be from the correlated pair of photons generated from SPDC and are accidental coincidences. To incorporate it, a combination of electronic delay generators and about 30 meters of coaxial cables are used, which were added between one of the single photon detectors and the coincidence-count-time-tagging FPGA. The data is shown in Fig. 6.8. The first and second columns are the single's counts, the third column is the measured coincidence counts. The adjustment to the duty cycle is then estimated by making sure that one obtains accidental values which are close to the measured experimental values, by minimizing the average of the difference between the calculated accidentals and the measured ones, as shown at the bottom of the last column. This gives the value of 0.96, which is multiplied to 4τ.

6.3 Simulation Results to Put the Experimental Results in Perspective

In Appendix E we studies, through simulations, the quality of results we expect to obtain from the experiment, given the realistic errors in the setup. These errors are the imperfect

Singles A	Singles B	Measured Accidental Coincidences	Calculate Accidentals = S1*S2*190*10^(-9)*4*0.96/10	Calculated Accidentals minus Measured Accidentals
195154	174037	2399	2478.01465828608	79.0146582860803
192232	162936	2308	2285.21759956992	-22.7824004300796
159044	188898	2183	2191.94410263552	8.94410263551981
161524	142073	1607	1674.30061742592	67.3006174259201
161525	303139	3519	3572.451888096	53.4518880959999
161049	17288	170	203.13633457152	33.13633457152
158818	170712	1983	1978.10161883136	-4.89838116864007
159031	159113	1803	1846.17250773888	43.1725077388801
171884	185316	2361	2323.98432589824	-37.0156741017599
169867	138303	1777	1714.05772154496	-62.94227845504
169343	293140	3740	3621.8224641792	-118.1775358208
169443	17007	160	210.25007968896	50.25007968896
169684	168203	2098	2082.37746888192	-15.6225311180797
169786	154126	1945	1909.24916614656	-35.7508338534401
172270	181722	2345	2284.0309626624	-60.9690373376002
172066	137626	1704	1727.74790785536	23.7479078553599
172205	291968	3771	3668.3083751424	-102.6916248576
173423	18261	183	231.05537532288	48.05537532288
172812	169235	2121	2133.7764003072	12.7764003071998
172582	153595	1921	1934.0041478784	13.0041478783999
179729	182659	2494	2395.21255222656	-98.7874477734399
179467	137861	1808	1805.13984634752	-2.86015365248022
176844	287771	3770	3712.97633186304	-57.0236681369597
176824	18489	221	238.52805037056	17.52805037056
175890	167245	2179	2146.244113728	-32.7558862720002
174467	147570	1847	1878.4351050624	31.4351050624002
158983	177272	2088	2056.24878007296	-31.75121992704
159087	133589	1481	1550.56585580928	69.56585580928
158147	282918	3373	3264.42249974016	-108.57750025984
158885	18703	191	216.8098442688	25.8098442688
158182	167343	1904	1931.29865508096	27.2986550809601
158506	146135	1662	1689.9924936576	27.9924936576001
			SUM(L10:L41)/31 =	-5.16523061640255

Figure 6.8 Accidentals subtraction

fidelity and purity of the polarization EPR pair entering the loop graph setup, the unbalanced losses in the arms of the interferometers and the imperfect visibility of interferometers.

It is worth going through the details of how the effect of the imperfect visibility of interferometers on purity and fidelity of the final state are taken into account. In our setup, we have converted the path qubits to polarization qubits before measurement. The 93% visibility of interferometers means that the polarization state of 7% of the photons that arrive at the tomography wave plates are incoherent, hence upon their arrival at the polarization beam splitter before the detector they behave randomly, as a mixes state does. This means the state after measurement is a mixture of pure and mixed states such that it can be written as $\rho = \gamma|\psi_{pure}\rangle\langle\psi_{pure}| + (1-\gamma)Identity$, where ψ_{pure} is the expected pure state if the visibilities were perfect and γ is the visibility of interferometers. Having written the density matrix of the state this one, one can use the usual formulas for purity and fidelity and find these relations as a function of a γ, as is done in Appendix E.

In the previous chapter and this one we have talked about various sources of error in our setup. Figure 6.9 summarizes these, their magnitude and if they effect only the fidelity or both the fidelity and the purity of the results.

Cause of Error	Magnitude of Error	Affects	By Amount
Source of polarization EPR pairs	Fidelity is 0.85, instead of 1	Fidelity and purity of the loop graph	Simulated
visibility of interferometers	94% (±1%)	Fidelity and purity of the loop graph	Simulated
Unbalanced losses in arms of interferometers	A = 40:60, B = 46:54, instead of 50:50	Fidelity and purity of the loop graph	Simulated
Phase drift of interferometers	2% of π in 10 minutes	Fidelity and purity of the loop graph	Negligible
Inaccurate setting of phases of interferometers	Calculated for up to 10% error	Fidelity only	Up to 6%
Error in the retardance of waveplates that create the graph state	Calculated for up to 2% error	Fidelity only	Negligible
Error in the angle waveplates that create the graph state	Calculated for up to ±2° error	Fidelity only	Up to 1.5%

Figure 6.9 Summary of errors in the setup, their magnitude and their effect on fidelity and purity.

Figure 6.10 shows the expected result of state tomography on path qubits, for given settings of measurement on polarization qubits. The first column in the table shows the setting for the measurement of polarization qubits. The path qubits remain in a certain state if the polarization qubits happen to be measured in these basis. The second column shows the purity of this state of path qubits. The purity is calculated by the formula $Purity = \rho_{simulation}\dot{\rho}_{simulation}$. The third column shows the fidelity of the state of path qubits with the

target state and is calculated by $Fidelity = rho_{simulation}\dot{\rho}_{target}$. In the third column, the errors resulting from inaccurate settings of wave plates that create the state and phase of interferometers are added to the simulated fidelities in quadrature, which equals an additional 6%.

Basis for polarisation qubits	Purity	Fidelity	Taking all errors into account Fidelity can go down by another 6%
HH	0.86	0.91	0.85
HV	0.86	0.92	0.86
VH	0.80	0.88	0.82
VV	0.80	0.88	0.82
RV	0.75	0.82	0.76
RH	0.76	0.81	0.75
DV	0.75	0.81	0.75
DH	0.76	0.80	0.74
DR	0.82	0.80	0.74
DD	0.76	0.81	0.75
RD	0.75	0.82	0.76
HD	0.86	0.91	0.85
VD	0.81	0.89	0.83
VL	0.89	0.93	0.87
HL	0.89	0.93	0.87
RL	0.80	0.87	0.81

Figure 6.10 Effects of errors in the setup on fidelity and purity of the state of path qubits for each measurement setting o f polarization qubits as simulated in Appendix E.

Figure 6.11 shows the simulated effects on the output of quantum computation using the graph for three different choices of computations.

6.4 Experimental Results

In this section, we start by listing the detailed results of the experiment. These results constitute the reconstructed density matrix corresponding to the state of the path qubits, given the polarization qubits are measured in the named basis. The reconstruction is done using the methods of Linear Inversion and Maximum Likelihood.

The results for three different choices of quantum computation are also detailed.

We then summarize all these results in tables and give an analysis of them.

Measurement angles	Purity	Fidelity	All Errors taken into account
0, 0	0.76	0.81	0.75
0, $\pi/2$	0.81	0.80	0.74
$\pi/2$, $\pi/2$	0.77	0.79	0.73

Figure 6.11 Effects of errors in the setup on fidelity and purity of the state of path qubits for each measurement setting of polarization qubits as simulated in Appendix E.

6.4.1 Tomography Results on the Source for 4-qubit State Tomography

The polarization entangled photons coming from the source, after single mode fibers give the following results. The eigenvalues of the density matrix reconstructed by the method of Linear Inversion (Eig-Linear) and Maximum Likelihood (Eig-MLH), and their corresponding purities are

Eig-Linear	Eig-MLH
-0.0503	0.0000
0.0267	0.0000
0.0911	0.0827
0.9326	0.9173
Purity-Linear	Purity-MLH
0.8812	0.8483

The density matrix reconstructed by Linear Inversion is

$$\rho = \begin{pmatrix} 0.5467 & -0.0227+0.0270i & -0.0601-0.0421i & 0.4073-0.1698i \\ -0.0227-0.0270i & 0.0118 & -0.0321-0.0054i & -0.0037+0.0042i \\ -0.0601+0.0421i & -0.0321+0.0054i & 0.0239 & 0.0308+0.0138i \\ 0.4073+0.1698i & -0.0037-0.0042i & 0.0308-0.0138i & 0.4176 \end{pmatrix}.$$

The density matrix reconstructed by Maximum Likelihood is

$$\rho_{mlh} = \begin{pmatrix} 0.5395 & -0.0235+0.0229i & -0.0458-0.0361i & 0.3919-0.1710i \\ -0.0235-0.0229i & 0.0111 & 0.0042+0.0160i & -0.0026+0.0084i \\ -0.0458+0.0361i & 0.0042-0.0160i & 0.0249 & 0.0112+0.0184i \\ 0.3919+0.1710i & -0.0026-0.0084i & 0.0112-0.0184i & 0.4245 \end{pmatrix}.$$

The theoretical, target state is

$$T = \begin{pmatrix} 0.5 & 0 & 0 & 0.5 \\ 0 & 0 & 0 & 0 \\ 0 & 0 & 0 & 0 \\ 0.5 & 0 & 0 & 0.5 \end{pmatrix}.$$

The fidelity is calculated using $sum(diag(rho_m lh * T))$ and it equals 0.87.

6.4.2 Tomography Results on the Path Qubits for Polarization HH

Tomography on path qubits, when polarization qubits are measured to be HH, give the following results. The eigenvalues of the density matrix reconstructed by the method of Linear Inversion (Eig-Linear) and Maximum Likelihood (Eig-MLH), and their corresponding purities are

Eig-Linear	Eig-MLH
-0.0422	0.0000
0.0623	0.0000
0.1115	0.1269
0.8684	0.8731
Purity-Linear	Purity-MLH
0.7722	0.7783

The density matrix reconstructed by Linear Inversion is

$$\rho = \begin{pmatrix} 0.0.2891 & 0.2225 + 0.0506i & 0.2187 - 0.0396i & 0.1858 + 0.0490i \\ 0.2225 - 0.0506i & 0.1754 & 0.1808 - 0.0420i & 0.1497 - 0.0513i \\ 0.2187 + 0.0396i & 0.1808 + 0.0420i & 0.3124 & 0.2303 + 0.0657i \\ 0.1858 - 0.0490i & 0.1497 + 0.0513i & 0.2303 - 0.0657i & 0.2230 \end{pmatrix}.$$

The density matrix reconstructed by Maximum Likelihood is

$$\rho_{mlh} = \begin{pmatrix} 00.2940 & 0.2188 + 0.0576i & 0.2131 - 0.0324i & 0.1790 + 0.0056i \\ 0.2188 - 0.0576i & 0.1784 & 0.1709 - 0.0836i & 0.1538 - 0.0400i \\ 0.2131 + 0.0324i & 0.1709 + 0.0836i & 0.3117 & 0.2506 + 0.0645i \\ 0.1790 - 0.0056i & 0.1538 + 0.0400i & 0.2506 - 0.0645i & 0.2159 \end{pmatrix}.$$

The theoretical, target state is

$$T = \frac{1}{4}\begin{pmatrix} 1 & 1 & 1 & 1 \\ 1 & 1 & 1 & 1 \\ 1 & 1 & 1 & 1 \\ 1 & 1 & 1 & 1 \end{pmatrix}.$$

The fidelity of experiment with theory is 0.84.

6.4.3 Tomography Results on the Path Qubits for Polarization HV

Tomography on path qubits, when polarization qubits are measured to be HV, give the following results. The eigenvalues of the density matrix reconstructed by the method of Linear Inversion (Eig-Linear) and Maximum Likelihood (Eig-MLH), and their corresponding purities are

Eig-Linear	Eig-MLH
-0.0415	-0.0000
0.0256	0.0000
0.1260	0.1707
0.8898	0.8293
Purity-Linear	Purity-MLH
0.8100	0.7168

The density matrix reconstructed by Linear Inversion is

$$\rho = \begin{pmatrix} 0.2500 & -0.2399 - 0.0165i & 0.1642 - 0.0271i & -0.1913 - 0.0264i \\ -0.2399 + 0.0165i & 0.2431 & -0.1894 + 0.1177i & 0.2010 - 0.0132i \\ 0.1642 + 0.0271i & -0.1894 - 0.1177i & 0.2236 & -0.2447 - 0.0784i \\ -0.1913 + 0.0264i & 0.2010 + 0.0132i & -0.2447 + 0.0784i & 0.2834 \end{pmatrix}.$$

The density matrix reconstructed by Maximum Likelihood is

$$\rho_{mlh} = \begin{pmatrix} 0.2542 & -0.2372 - 0.0118i & 0.1299 - 0.0504i & -0.1474 + 0.0046i \\ -0.2372 + 0.0118i & 0.2422 & -0.1759 + 0.0567i & 0.1955 + 0.0053i \\ 0.1299 + 0.0504i & -0.1759 - 0.0567i & 0.2375 & -0.2371 - 0.0836i \\ -0.1474 - 0.0046i & 0.1955 - 0.0053i & -0.2371 + 0.0836i & 0.2660 \end{pmatrix}.$$

The theoretical, target state is

$$T = \frac{1}{4}\begin{pmatrix} 1 & -1 & 1 & -1 \\ -1 & 1 & -1 & 1 \\ 1 & -1 & 1 & -1 \\ -1 & 1 & -1 & 1 \end{pmatrix}.$$

The fidelity of experiment with theory is 0.81.

6.4.4 Tomography Results on the Path Qubits for Polarization VH

Tomography on path qubits, when polarization qubits are measured to be VH, give the following results. The eigenvalues of the density matrix reconstructed by the method of Linear Inversion (Eig-Linear) and Maximum Likelihood (Eig-MLH), and their corresponding purities are

Eig-Linear	Eig-MLH
-0.1036	-0.0000
-0.0353	0.0000
0.0678	0.0134
1.0711	0.9866
Purity-Linear	Purity-MLH
1.1638	0.9736

The density matrix reconstructed by Linear Inversion is

$$\rho = \begin{pmatrix} 0.2414 & -0.2955+0.0948i & -0.1951-0.0833i & 0.3422+0.0303i \\ -0.2955-0.0948i & 0.3496 & 0.1421+0.1770i & -0.3049-0.0675i \\ -0.1951+0.0833i & 0.1421-0.1770i & 0.1488 & -0.1889+0.0519i \\ 0.3422-0.0303i & -0.3049+0.0675i & -0.1889-0.0519i & 0.2602 \end{pmatrix}.$$

The density matrix reconstructed by Maximum Likelihood is

$$\rho_{mlh} = \begin{pmatrix} 0.2206 & -0.2649+0.0384i & -0.1848-0.0451i & 0.2407-0.0144i \\ -0.2649-0.0384i & 0.3382 & 0.2113+0.0894i & -0.3039-0.0212i \\ -0.1848+0.0451i & 0.2113-0.0894i & 0.1654 & -0.1954+0.0634i \\ 0.2407+0.0144i & -0.3039+0.0212i & -0.1954-0.0634i & 0.2758 \end{pmatrix}.$$

The theoretical, target state is

$$T = \frac{1}{4}\begin{pmatrix} 1 & -1 & -1 & 1 \\ -1 & 1 & 1 & -1 \\ -1 & 1 & 1 & -1 \\ 1 & -1 & -1 & 1 \end{pmatrix}.$$

The fidelity of experiment with theory is 0.95.

6.4.5 Tomography Results on the Path Qubits for Polarization VV

Tomography on path qubits, when polarization qubits are measured to be VV, give the following results. The eigenvalues of the density matrix reconstructed by the method of Linear Inversion (Eig-Linear) and Maximum Likelihood (Eig-MLH), and their corresponding purities are

Eig-Linear	Eig-MLH
-0.2054	0.0000
-0.0236	0.0000
0.0827	0.0003
1.1463	0.9997
Purity-Linear	Purity-MLH
1.3637	0.9995

The density matrix reconstructed by Linear Inversion is

$$\rho = \begin{pmatrix} 0.4699 & 0.2960+0.0645i & -0.4147-0.0462i & -0.3653-0.0484i \\ 0.2960-0.0645i & 0.1429 & -0.1584+0.0031i & -0.0853+0.0114i \\ -0.4147+0.0462i & -0.1584-0.0031i & 0.3594 & 0.2486-0.0130i \\ -0.3653+0.0484i & -0.0853-0.0114i & 0.2486+0.0130i & 0.0277 \end{pmatrix}.$$

The density matrix reconstructed by Maximum Likelihood is

$$\rho_{mlh} = \begin{pmatrix} 0.4489 & 0.2320+0.0644i & -0.3922-0.0296i & -0.1790-0.0499i \\ 0.2320-0.0644i & 0.1293 & -0.2069+0.0411i & -0.0997-0.0001i \\ -0.3922+0.0296i & -0.2069-0.0411i & 0.3449 & 0.1598+0.0319i \\ -0.1790+0.0499i & -0.0997+0.0001i & 0.1598-0.0319i & 0.0770 \end{pmatrix}.$$

The theoretical, target state is

$$T = \frac{1}{4}\begin{pmatrix} 1 & 1 & -1 & -1 \\ 1 & 1 & -1 & -1 \\ -1 & -1 & 1 & 1 \\ -1 & -1 & 1 & 1 \end{pmatrix}.$$

The fidelity of experiment with theory is 0.88.

6.4.6 Tomography Results on the Path Qubits for Polarization RH

Tomography on path qubits, when polarization qubits are measured to be RH, give the following results. The eigenvalues of the density matrix reconstructed by the method of Linear Inversion (Eig-Linear) and Maximum Likelihood (Eig-MLH), and their corresponding purities are

Eig-Linear	Eig-MLH
-0.1342	0.0000
-0.0335	0.0000
0.1685	0.0875
0.9991	0.9125
Purity-Linear	Purity-MLH
1.0458	0.8404

The density matrix reconstructed by Linear Inversion is

$$\rho = \begin{pmatrix} 0.2007 & -0.1103+0.2597i & 0.0066+0.1970i & 0.1717+0.0772i \\ -0.1103-0.2597i & 0.4090 & 0.4053-0.0625i & -0.1015-0.1103i \\ 0.0066-0.1970i & 0.4053+0.0625i & 0.3662 & -0.0103-0.0846i \\ 0.1717-0.0772i & -0.1015+0.1103i & -0.0103+0.0846i & 0.0241 \end{pmatrix}.$$

The density matrix reconstructed by Maximum Likelihood is

$$\rho_{mlh} = \begin{pmatrix} 0.2031 & -0.0754+0.2467i & 0.0132+0.2085i & 0.0743-0.0123i \\ -0.0754-0.2467i & 0.3824 & 0.3409-0.0651i & -0.0494-0.0852i \\ 0.0132-0.2085i & 0.3409+0.0651i & 0.3857 & -0.0191-0.0727i \\ 0.0743+0.0123i & -0.0494+0.0852i & -0.0191+0.0727i & 0.0288 \end{pmatrix}.$$

The theoretical, target state is

$$T = \frac{1}{4}\begin{pmatrix} 1 & i & i & 1 \\ -i & 1 & 1 & -i \\ -i & 1 & 1 & -i \\ 1 & i & i & 1 \end{pmatrix}.$$

The fidelity of experiment with theory is 0.76.

6.4.7 Tomography Results on the Path Qubits for Polarization RV

Tomography on path qubits, when polarization qubits are measured to be RV, give the following results. The eigenvalues of the density matrix reconstructed by the method of Linear Inversion (Eig-Linear) and Maximum Likelihood (Eig-MLH), and their corresponding purities are

Eig-Linear	Eig-MLH
-0.0800	-0.0000
-0.0115	0.0000
0.1529	0.0949
0.9386	0.9051
Purity-Linear	Purity-MLH
0.9108	0.8282

The density matrix reconstructed by Linear Inversion is

$$\rho = \begin{pmatrix} 0.5198 & -0.1935+0.1132i & -0.0337-0.2210i & -0.2205-0.2353i \\ -0.1935-0.1132i & 0.0647 & -0.0100+0.1330i & 0.0456+0.1002i \\ -0.0337+0.2210i & -0.0100-0.1330i & 0.0712 & 0.0648-0.1346i \\ -0.2205+0.2353i & 0.0456-0.1002i & 0.0648+0.1346i & 0.3443 \end{pmatrix}.$$

The density matrix reconstructed by Maximum Likelihood is

$$\rho_{mlh} = \begin{pmatrix} 0.4820 & -0.1597+0.0724i & -0.0199-0.1934i & -0.2551-0.2450i \\ -0.1597-0.0724i & 0.0721 & -0.0136+0.0697i & 0.0283+0.0988i \\ -0.0199+0.1934i & -0.0136-0.0697i & 0.0887 & 0.0816-0.1083i \\ -0.2551+0.2450i & 0.0283-0.0988i & 0.0816+0.1083i & 0.3572 \end{pmatrix}.$$

The theoretical, target state is

$$T = \frac{1}{4}\begin{pmatrix} 1 & i & -i & -1 \\ -i & 1 & -1 & i \\ i & -1 & 1 & -i \\ -1 & -i & i & 1 \end{pmatrix}.$$

The fidelity of experiment with theory is 0.62.

6.4.8 Tomography Results on the Path Qubits for Polarization DV

Tomography on path qubits, when polarization qubits are measured to be DV, give the following results. The eigenvalues of the density matrix reconstructed by the method of Linear Inversion (Eig-Linear) and Maximum Likelihood (Eig-MLH), and their corresponding purities are

Eig-Linear	Eig-MLH
-0.0555	-0.0000
0.0466	0.0002
0.1444	0.1568
0.8644	0.8430
Purity-Linear	Purity-MLH
0.7733	0.7353

The density matrix reconstructed by Linear Inversion is

$$\rho = \begin{pmatrix} 0.0574 & -0.0276+0.0477i & 0.0829-0.1570i & -0.0925-0.0558i \\ -0.0276-0.0477i & 0.2935 & -0.2713+0.0983i & 0.0150+0.1815i \\ 0.0829+0.1570i & -0.2713-0.0983i & 0.4962 & -0.0366-0.2076i \\ -0.0925+0.0558i & 0.0150-0.1815i & -0.0366+0.2076i & 0.1530 \end{pmatrix}.$$

The density matrix reconstructed by Maximum Likelihood is

$$\rho_{mlh} = \begin{pmatrix} 0.0608 & -0.0410+0.0540i & 0.0733-0.1490i & -0.0815-0.0136i \\ -0.0410-0.0540i & 0.3026 & -0.2472+0.0875i & 0.0040+0.1681i \\ 0.0733+0.1490i & -0.2472-0.0875i & 0.4846 & -0.0338-0.2321i \\ -0.0815+0.0136i & 0.0040-0.1681i & -0.0338+0.2321i & 0.1520 \end{pmatrix}.$$

The theoretical, target state is

$$T = \begin{pmatrix} 0 & 0 & 0 & 0 \\ 0 & 0.5 & -0.5 & 0 \\ 0 & -0.5 & 0.5 & 0 \\ 0 & 0 & 0 & 0 \end{pmatrix}.$$

The fidelity of experiment with theory is 0.64.

6.4.9 Tomography Results on the Path Qubits for Polarization DH

Tomography on path qubits, when polarization qubits are measured to be DH, give the following results. The eigenvalues of the density matrix reconstructed by the method of Linear Inversion (Eig-Linear) and Maximum Likelihood (Eig-MLH), and their corresponding purities are

Eig-Linear	Eig-MLH
-0.1468	-0.0000
0.0341	0.0000
0.1823	0.0619
0.9304	0.9381
Purity-Linear	Purity-MLH
0.9215	0.8839

The density matrix reconstructed by Linear Inversion is

$$\rho = \begin{pmatrix} 0.5279 & -0.0929 + 0.1760i & 0.0340 + 0.1569i & 0.3131 + 0.0748i \\ -0.0929 - 0.1760i & 0.0802 & -0.0387 - 0.1085i & 0.0424 - 0.1933i \\ 0.0340 - 0.1569i & -0.0387 + 0.1085i & 0.0470 & 0.1784 - 0.0662i \\ 0.3131 - 0.0748i & 0.0424 + 0.1933i & 0.1784 + 0.0662i & 0.3448 \end{pmatrix}.$$

The density matrix reconstructed by Maximum Likelihood is

$$\rho_{mlh} = \begin{pmatrix} 0.5003 & -0.0927 + 0.1673i & 0.0668 + 0.1334i & 0.3223 + 0.1719i \\ -0.0927 - 0.1673i & 0.0973 & 0.0450 - 0.0593i & 0.0060 - 0.1824i \\ 0.0668 - 0.1334i & 0.0450 + 0.0593i & 0.0575 & 0.1149 - 0.0814i \\ 0.3223 - 0.1719i & 0.0060 + 0.1824i & 0.1149 + 0.0814i & 0.3449 \end{pmatrix}.$$

The theoretical, target state is

$$T = \begin{pmatrix} 0.5 & 0 & 0 & 0.5 \\ 0 & 0 & 0 & 0 \\ 0 & 0 & 0 & 0 \\ 0.5 & 0 & 0 & 0.5 \end{pmatrix}.$$

The fidelity of experiment with theory is 0.74.

6.4.10 Tomography Results on the Path Qubits for Polarization DR

Tomography on path qubits, when polarization qubits are measured to be DR, give the following results. The eigenvalues of the density matrix reconstructed by the method of Linear Inversion (Eig-Linear) and Maximum Likelihood (Eig-MLH), and their corresponding purities are

Eig-Linear	Eig-MLH
-0.1434	0.0000
0.0382	0.0000
0.1134	0.0203
0.9918	0.9797
Purity-Linear	Purity-MLH
1.0185	0.9602

The density matrix reconstructed by Linear Inversion is

$$\rho = \begin{pmatrix} 0.0985 & 0.0574 - 0.0712i & 0.0324 + 0.2588i & 0.1350 + 0.0931i \\ 0.0574 + 0.0712i & 0.0344 & 0.0169 + 0.0165i & 0.0169 + 0.0771i \\ 0.0324 - 0.2588i & 0.0169 - 0.0165i & 0.4041 & 0.1526 - 0.4262i \\ 0.1350 - 0.0931i & 0.0169 - 0.0771i & 0.1526 + 0.4262i & 0.4629 \end{pmatrix}.$$

The density matrix reconstructed by Maximum Likelihood is

$$\rho_{mlh} = \begin{pmatrix} 0.1175 & 0.0390 - 0.0452i & 0.0178 + 0.2110i & 0.2069 + 0.0701i \\ 0.0390 + 0.0452i & 0.0364 & -0.0654 + 0.0682i & 0.0376 + 0.0900i \\ 0.0178 - 0.2110i & -0.0654 - 0.0682i & 0.4099 & 0.1689 - 0.3876i \\ 0.2069 - 0.0701i & 0.0376 - 0.0900i & 0.1689 + 0.3876i & 0.4362 \end{pmatrix}.$$

The theoretical, target state is

$$T = \frac{1}{4}\begin{pmatrix} 1 & -i & i & 1 \\ i & 1 & -1 & i \\ -i & -1 & 1 & -i \\ 1 & -i & i & 1 \end{pmatrix}.$$

The fidelity of experiment with theory is 0.75.

6.4.11 Tomography Results on the Path Qubits for Polarization DD

Tomography on path qubits, when polarization qubits are measured to be DD, give the following results. The eigenvalues of the density matrix reconstructed by the method of Linear Inversion (Eig-Linear) and Maximum Likelihood (Eig-MLH), and their corresponding purities are

Eig-Linear	Eig-MLH
-0.0380	-0.0000
-0.0135	0.0000
0.0968	0.0669
0.9546	0.9331
Purity-Linear	Purity-MLH
0.92	0.87

The density matrix reconstructed by Linear Inversion is

$$\rho = \begin{pmatrix} 0.3072 & -0.0133 + 0.2657i & -0.2398 - 0.0752i & 0.0093 + 0.2195i \\ -0.0133 - 0.2657i & 0.2248 & -0.0474 + 0.1935i & 0.2681 - 0.0139i \\ -0.2398 + 0.0752i & -0.0474 - 0.1935i & 0.1724 & -0.0705 - 0.1766i \\ 0.0093 - 0.2195i & 0.2681 + 0.0139i & -0.0705 + 0.1766i & 0.2955 \end{pmatrix}.$$

The density matrix reconstructed by Maximum Likelihood is

$$\rho_{mlh} = \begin{pmatrix} 0.2804 & -0.0110 + 0.2603i & -0.2141 - 0.0537i & 0.0281 + 0.2416i \\ -0.0110 - 0.2603i & 0.2426 & -0.0419 + 0.2005i & 0.2300 - 0.0353i \\ -0.2141 + 0.0537i & -0.0419 - 0.2005i & 0.1743 & -0.0735 - 0.1748i \\ 0.0281 - 0.2416i & 0.2300 + 0.0353i & -0.0735 + 0.1748i & 0.3026 \end{pmatrix}.$$

The theoretical, target state is

$$T = \frac{1}{4}\begin{pmatrix} 1 & 1 & -1 & 1 \\ 1 & 1 & -1 & 1 \\ -1 & -1 & 1 & -1 \\ 1 & 1 & -1 & 1 \end{pmatrix}.$$

The fidelity of experiment with theory is 0.54.

6.4.12 Tomography Results on the Path Qubits for Polarization RD

Tomography on path qubits, when polarization qubits are measured to be RD, give the following results. The eigenvalues of the density matrix reconstructed by the method of Linear Inversion (Eig-Linear) and Maximum Likelihood (Eig-MLH), and their corresponding purities are

Eig-Linear	Eig-MLH
-0.2121	-0.0000
0.0637	0.0000
0.1738	0.0520
0.9747	0.9480
Purity-Linear	Purity-MLH
1.0293	0.9013

The density matrix reconstructed by Linear Inversion is

$$\rho = \begin{pmatrix} 0.2123 & 0.0125 + 0.2396i & -0.2205 + 0.0537i & -0.2806 + 0.1439i \\ 0.0125 - 0.2396i & 0.3584 & 0.1172 + 0.1868i & 0.2373 + 0.1266i \\ -0.2205 - 0.0537i & 0.1172 - 0.1868i & 0.2286 & 0.0822 - 0.2131i \\ -0.2806 - 0.1439i & 0.2373 - 0.1266i & 0.0822 + 0.2131i & 0.2007 \end{pmatrix}.$$

The density matrix reconstructed by Maximum Likelihood is

$$\rho_{mlh} = \begin{pmatrix} 0.2307 & -0.0306 + 0.2533i & -0.2244 + 0.0078i & -0.1140 + 0.1753i \\ -0.0306 - 0.2533i & 0.3592 & 0.0474 + 0.2449i & 0.2122 + 0.0946i \\ -0.2244 - 0.0078i & 0.0474 - 0.2449i & 0.2196 & 0.1173 - 0.1676i \\ -0.1140 - 0.1753i & 0.2122 - 0.0946i & 0.1173 + 0.1676i & 0.1905 \end{pmatrix}.$$

The theoretical, target state is

$$T = \frac{1}{4}\begin{pmatrix} 1 & i & -1 & i \\ -i & 1 & i & 1 \\ -1 & -i & -1 & -i \\ -i & 1 & i & 1 \end{pmatrix}.$$

The fidelity of experiment with theory is 0.78.

6.4.13 Tomography Results on the Path Qubits for Polarization HD

Tomography on path qubits, when polarization qubits are measured to be HD, give the following results. The eigenvalues of the density matrix reconstructed by the method of Linear Inversion (Eig-Linear) and Maximum Likelihood (Eig-MLH), and their corresponding purities are

Eig-Linear	Eig-MLH
-0.1959	-0.0000
0.0304	0.0000
0.1570	0.0388
1.0085	0.9612
Purity-Linear	Purity-MLH
1.0811	0.9254

The density matrix reconstructed by Linear Inversion is

$$\rho = \begin{pmatrix} 0.0000 & 0.0271+0.1004i & 0.0312+0.0000i & -0.0286-0.0830i \\ 0.0271-0.1004i & 0.4725 & -0.0184+0.0930i & 0.4606+0.2043i \\ 0.0312-0.0000i & -0.0184-0.0930i & 0.0000 & 0.0506+0.0692i \\ -0.0286+0.0830i & 0.4606-0.2043i & 0.0506-0.0692i & 0.5275 \end{pmatrix}.$$

The density matrix reconstructed by Maximum Likelihood is

$$\rho_{mlh} = \begin{pmatrix} 0.0106 & 0.0353+0.0567i & 0.0089+0.0018i & 0.0140+0.0679i \\ 0.0353-0.0567i & 0.4450 & 0.0445-0.0390i & 0.4049+0.1967i \\ 0.0089-0.0018i & 0.0445+0.0390i & 0.0092 & 0.0273+0.0648i \\ 0.0140-0.0679i & 0.4049-0.1967i & 0.0273-0.0648i & 0.5351 \end{pmatrix}.$$

The theoretical, target state is

$$T = \begin{pmatrix} 0 & 0 & 0 & 0 \\ 0 & 0.5 & 0 & 0.5 \\ 0 & 0 & 0 & 0 \\ 0 & 0.5 & 0 & 0.5 \end{pmatrix}.$$

The fidelity of experiment with theory is 0.89.

6.4.14 Tomography Results on the Path Qubits for Polarization VD

Tomography on path qubits, when polarization qubits are measured to be VD, give the following results. The eigenvalues of the density matrix reconstructed by the method of Linear Inversion (Eig-Linear) and Maximum Likelihood (Eig-MLH), and their corresponding purities are

Eig-Linear	Eig-MLH
-0.0412	-0.0000
-0.0053	0.0000
0.0451	0.0000
1.0014	1.0000
Purity-Linear	Purity-MLH
1.0066	1.0000

The density matrix reconstructed by Linear Inversion is

$$\rho = \begin{pmatrix} 0.5373 & -0.0938 + 0.0047i & -0.4747 - 0.0900i & 0.0723 + 0.0287i \\ -0.0938 - 0.0047i & 0.0403 & 0.1166 + 0.0306i & -0.0253 - 0.0253i \\ -0.4747 + 0.0900i & 0.1166 - 0.0306i & 0.4121 & -0.0951 - 0.0028i \\ 0.0723 - 0.0287i & -0.0253 + 0.0253i & -0.0951 + 0.0028i & 0.0103 \end{pmatrix}.$$

The density matrix reconstructed by Maximum Likelihood is

$$\rho_{mlh} = \begin{pmatrix} 0.5475 & -0.1255 + 0.0203i & -0.4682 - 0.0745i & 0.0813 + 0.0145i \\ -0.1255 - 0.0203i & 0.0295 & 0.1045 + 0.0344i & -0.0181 - 0.0063i \\ -0.4682 + 0.0745i & 0.1045 - 0.0344i & 0.4105 & -0.0715 - 0.0013i \\ 0.0813 - 0.0145i & -0.0181 + 0.0063i & -0.0715 + 0.0013i & 0.0125 \end{pmatrix}.$$

The theoretical, target state is

$$T = \begin{pmatrix} 0.5 & 0 & -0.5 & 0 \\ 0 & 0 & 0 & 0 \\ -0.5 & 0 & 0.5 & 0 \\ 0 & 0 & 0 & 0 \end{pmatrix}.$$

The fidelity of experiment with theory is 0.95.

6.4.15 Tomography Results on the Path Qubits for Polarization VL

Tomography on path qubits, when polarization qubits are measured to be VL, give the following results. The eigenvalues of the density matrix reconstructed by the method of Linear Inversion (Eig-Linear) and Maximum Likelihood (Eig-MLH), and their corresponding purities are

Eig-Linear	Eig-MLH
-0.0224	-0.0000
-0.0033	0.0000
0.0418	0.0174
0.9840	0.9826
Purity-Linear	Purity-MLH
0.9705	0.9659

The density matrix reconstructed by Linear Inversion is

$$\rho = \begin{pmatrix} 0.3307 & -0.0437 + 0.2583i & -0.2945 - 0.0486i & 0.0689 - 0.2350i \\ -0.0437 - 0.2583i & 0.2387 & 0.0231 + 0.2235i & -0.2047 - 0.0394i \\ -0.2945 + 0.0486i & 0.0231 - 0.2235i & 0.2584 & -0.0491 + 0.1995i \\ 0.0689 + 0.2350i & -0.2047 + 0.0394i & -0.0491 - 0.1995i & 0.1723 \end{pmatrix}.$$

The density matrix reconstructed by Maximum Likelihood is

$$\rho_{mlh} = \begin{pmatrix} 0.3229 & -0.0602 + 0.2554i & -0.2897 - 0.0346i & 0.0736 - 0.2200i \\ -0.0602 - 0.2554i & 0.2321 & 0.0306 + 0.2396i & -0.2020 - 0.0237i \\ -0.2897 + 0.0346i & 0.0306 - 0.2396i & 0.2653 & -0.0469 + 0.2070i \\ 0.0736 + 0.2200i & -0.2020 + 0.0237i & -0.0469 - 0.2070i & 0.1796 \end{pmatrix}.$$

The theoretical, target state is

$$T = \frac{1}{4}\begin{pmatrix} 1 & i & -1 & -i \\ -i & 1 & i & -1 \\ -1 & -i & 1 & i \\ i & -1 & -i & 1 \end{pmatrix}.$$

The fidelity of experiment with theory is 0.96.

6.4.16 Tomography Results on the Path Qubits for Polarization HL

Tomography on path qubits, when polarization qubits are measured to be HL, give the following results. The eigenvalues of the density matrix reconstructed by the method of Linear Inversion (Eig-Linear) and Maximum Likelihood (Eig-MLH), and their corresponding purities are

Eig-Linear	Eig-MLH
-0.1936	-0.0000
0.0353	0.0000
0.0742	0.0297
1.0841	0.9703
Purity-Linear	Purity-MLH
1.2196	0.9423

The density matrix reconstructed by Linear Inversion is

$$\rho = \begin{pmatrix} 0.2784 & -0.1204+0.2322i & 0.3908+0.1070i & -0.2493+0.1191i \\ -0.1204-0.2322i & 0.2674 & -0.0958-0.2614i & 0.2225+0.0815i \\ 0.3908-0.1070i & -0.0958+0.2614i & 0.2390 & -0.0709+0.1898i \\ -0.2493-0.1191i & 0.2225-0.0815i & -0.0709-0.1898i & 0.2153 \end{pmatrix}.$$

The density matrix reconstructed by Maximum Likelihood is

$$\rho_{mlh} = \begin{pmatrix} 0.2859 & -0.1126+0.2285i & 0.2631+0.0755i & -0.1466+0.1682i \\ -0.1126-0.2285i & 0.2485 & -0.0403-0.2406i & 0.2107+0.0677i \\ 0.2631-0.0755i & -0.0403+0.2406i & 0.2624 & -0.0884+0.1963i \\ -0.1466-0.1682i & 0.2107-0.0677i & -0.0884-0.1963i & 0.2032 \end{pmatrix}.$$

The theoretical, target state is

$$T = \frac{1}{4}\begin{pmatrix} 1 & i & 1 & i \\ -i & 1 & -i & 1 \\ 1 & i & 1 & i \\ -i & 1 & -i & 1 \end{pmatrix}.$$

The fidelity of experiment with theory is 0.90.

6.4.17 Tomography Results on the Path Qubits for Polarization RL

Tomography on path qubits, when polarization qubits are measured to be RL, give the following results. The eigenvalues of the density matrix reconstructed by the method of Linear Inversion (Eig-Linear) and Maximum Likelihood (Eig-MLH), and their corresponding purities are

Eig-Linear	Eig-MLH
-0.0840	0.0000
0.0007	0.0000
0.1104	0.0379
0.9729	0.9621
Purity-Linear	Purity-MLH
0.9658	0.9270

The density matrix reconstructed by Linear Inversion is

$$\rho = \begin{pmatrix} 0.5637 & -0.0340 + 0.4129i & -0.0281 + 0.1314i & -0.2153 + 0.0055i \\ -0.0340 - 0.4129i & 0.3285 & 0.0629 - 0.0956i & 0.0313 + 0.1168i \\ -0.0281 - 0.1314i & 0.0629 + 0.0956i & 0.0334 & -0.0043 + 0.0539i \\ -0.2153 - 0.0055i & 0.0313 - 0.1168i & -0.0043 - 0.0539i & 0.0744 \end{pmatrix}.$$

The density matrix reconstructed by Maximum Likelihood is

$$\rho_{mlh} = \begin{pmatrix} 0.5625 & -0.0659 + 0.4184i & -0.0057 + 0.1166i & -0.1758 - 0.0008i \\ -0.0659 - 0.4184i & 0.3343 & 0.0774 - 0.0132i & 0.0250 + 0.1156i \\ -0.0057 - 0.1166i & 0.0774 + 0.0132i & 0.0315 & 0.0021 + 0.0475i \\ -0.1758 + 0.0008i & 0.0250 - 0.1156i & 0.0021 - 0.0475i & 0.0716 \end{pmatrix}.$$

The theoretical, target state is

$$T = \begin{pmatrix} 0.5 & 0.5i & 0 & 0 \\ -0.5i & 0.5 & 0 & 0 \\ 0 & 0 & 0 & 0 \\ 0 & 0 & 0 & 0 \end{pmatrix}.$$

The fidelity of experiment with theory is 0.87.

6.5 Summary of the Experimental Results and Discussion

Fig. 6.12 shows the result of the state tomography on path qubits for each setting of polarization tomography, as discussed in simulations of chapter 5.5, and the comparison with the target state found in those simulations.

Measurement Basis	Linear Inversion Purity	Maximum Likelihood Purity	Fidelity of Experimental Results with Target State	Fidelity of Simulated Results with Target State
HH	0.77	0.78	0.84	0.85
HV	0.81	0.72	0.81	0.86
VH	1.16	0.97	0.95	0.82
VV	1.36	1.00	0.88	0.82
RH	1.04	0.84	0.76	0.75
RV	0.91	0.83	0.62	0.76
DV	0.77	0.73	0.64	0.75
DH	0.92	0.88	0.74	0.74
DR	1.02	0.96	0.75	0.74
DD	0.92	0.87	0.54	0.75
RD	1.03	0.90	0.78	0.76
HD	1.08	0.92	0.89	0.85
VD	1.01	1.00	0.95	0.83
VL	0.97	0.96	0.96	0.87
HL	1.22	0.94	0.90	0.87
RL	0.96	0.93	0.87	0.81

Figure 6.12 The result of state tomography on four qubits.

The first column is the basis setting of the two polarization qubits. The second column is the purity of the result of state tomography on path qubits, where the method of Linear Inversion is used for reconstruction of the density matrices. This method can give rise to non-physical density matrices and consequently to purities above one. The third column is

the same result, but the method of Maximum Likelihood, which guarantees physical density matrices, is used. The third column is the fidelity of the experimental density matrices, reconstructed by Maximum Likelihood, with that of the perfect target state. These states were calculated in the simulations discussed in the previous chapter. In order to be able to determine what we should realistically expect from our experimental setup, given the quality of polarization entangled pairs from the source and the properties of interferometers, the creation of the graph is simulated, taking into account the different losses of different arms of interferometers, with the Maximum Likelihood density matrix that was reconstructed for the photons from the source as the input to the loop graph setup. The last column of the results is the fidelity of path qubits from this simulation with the perfect target state.

This column is the result of the simulation that takes all the errors listed in figure 6.9 into account as discussed in detail in section 6.3.

The purities of the reconstructed density matrices from the data taken for state tomography to characterize the experimentally created loop graph, range from 0.72 to 1. The fidelities with the ideal target state range from 0.54 to 0.96. The results of the accumulation of all errors listed for the setup can be seen in the experimental data. It is interesting to see that both simulations and the experimental data show that imperfect experimental conditions manifest as different amounts of error in different bases. Comparing the experimental values with the results of the last column of Fig. 6.12 and taking the errors into account the results of Maximum Likelihood reconstruction are what we would expect to obtain from the experimental setup for all basis settings for the majority of data points.

The results of tomography and quantum computation that include error bars are shown in Appendix F. For calculation of these error bars we have used a code borrowed from another group, which requires an over-complete set of data for maximum Likelihood Reconstruction. As our experimental data is complete, we have extrapolated the over-complete set from the available data. This is the main reason we are not reporting this data in this section and we only show the results in the mentioned Appendix. Note that the results, however, are very similar to the results we have presented in this section, hence the error bars reported in that Appendix are a fair representation of the error bars on our experimental data.

In order to obtain more confidence about the creation of the intended 4-qubit loop graph, we check to see if the state of path qubits, given certain states for polarization qubits, are indeed maximally entangled, within the errors, when they should be and completely separable when they should be. For this check we calculate the tangle and concurrence (Wootters, 1998) for each density matrix of path qubits. The concurrence is computed using a code written by Toby Cubitt, which is available online. The tangle was then calculated using the following

formula

$$Tangle(C) = -\frac{1+\sqrt{1-C^2}}{2} log_2 \frac{1+\sqrt{1-C^2}}{2} - \frac{1-\sqrt{1-C^2}}{2} log_2 \frac{1-\sqrt{1-C^2}}{2}.$$

Concurrence and Tangle are equal to 1 for a maximally entangled state and are equal to 0 for a fully separable state. The summary of these results and their comparison with the expected theoretical results are give in figure 6.13.

	Concurrence Experiment	Concurrence Theory	Tangle Experiment	Tangle Theory	Purity
HH	0.01	0	0.00	0	0.78
HV	0.15	0	0.05	0	0.72
VH	0.08	0	0.02	0	0.97
VV	0.06	0	0.01	0	1.00
RH	0.79	1	0.70	1	0.84
RV	0.86	1	0.80	1	0.83
DV	0.61	1	0.48	1	0.73
DH	0.86	1	0.81	1	0.88
DR	0.26	0	0.13	0	0.96
DD	0.88	1	0.83	1	0.87
RD	0.89	1	0.85	1	0.90
HD	0.04	0	0.00	0	0.92
VD	0.06	0	0.01	0	1.00
VL	0.01	0	0.00	0	0.96
HL	0.05	0	0.01	0	0.94
RL	0.20	0	0.08	0	0.93

Figure 6.13 A check to make sure the states are maximally entangled or completely separable when they should be. Concurrence and Tangle equal 1 show a maximally entangled state and Concurrence and Tangle equal 0 show a completely separable state.

The results show the states of path qubits are entangled for the polarization setting when they should be, and are completely separable when they should be. These results and the purities and fidelities given in figure 6.12 show that one can be fairly confident that the state we have created has an acceptable overlap with the 4-qubit loop graph state.

6.6 Experimental Results of Quantum Computation

Quantum computation using the graph state is demonstrated by choosing three different measurement settings, which correspond to three different combinations of θ_1 and θ_2 in the circuit of Fig. 4.4(b), where the angles θ are the angle of rotation in $HR(\theta)$ gate, before projection on computational basis. These values are chosen because they can give outputs that are very different from each other. For example, one is a completely separable state,

while the other is maximally entangled. The computations are done by post-selecting on the results of measurements of polarization qubits being zero, hence no active feed-forward was necessary.

6.6.1 Tomography Results on the Source for Quantum Computation

This result is for the polarization entangled photons coming from the source, after single mode fibers. It is taken on a different night from the previous result. Different temperature conditions on the lab at different nights give slightly different result.

The eigenvalues of the density matrix reconstructed by the method of Linear Inversion (Eig-Linear) and Maximum Likelihood (Eig-MLH), and their corresponding purities are

Eig-Linear	Eig-MLH
-0.0565	0.0000
0.0468	0.0066
0.0851	0.0751
0.9246	0.9183
Purity-Linear	Purity-MLH
0.8676	0.8489

The density matrix reconstructed by Linear Inversion is

$$\rho = \begin{pmatrix} 0.5288 & -0.0232 - 0.0245i & -0.0399 + 0.0281i & 0.4271 + 0.0266i \\ -0.0232 + 0.0245i & 0.0192 & -0.0392 - 0.0117i & 0.0116 + 0.0081i \\ -0.0399 - 0.0281i & -0.0392 + 0.0117i & 0.0000 & 0.0214 - 0.0516i \\ 0.4271 - 0.0266i & 0.0116 - 0.0081i & 0.0214 + 0.0516i & 0.4520 \end{pmatrix}.$$

The density matrix reconstructed by Maximum Likelihood is

$$\rho_{mlh} = \begin{pmatrix} 0.5082 & -0.0148 - 0.0403i & -0.0130 + 0.0334i & 0.4238 + 0.0250i \\ -0.0148 + 0.0403i & 0.0189 & 0.0000 - 0.0018i & -0.0024 + 0.0059i \\ -0.0130 - 0.0334i & 0.0000 + 0.0018i & 0.0032 & -0.0064 - 0.0370i \\ 0.4238 - 0.0250i & -0.0024 - 0.0059i & -0.0064 + 0.0370i & 0.4697 \end{pmatrix}.$$

The Fidelity of this state with the target state, which is $\frac{|HH\rangle+|VV\rangle}{\sqrt{2}}$, is 0.91.

6.6.2 Results for the Quantum Computation Corresponding to $\theta_1 = \theta_2 = \pi/2$

One of the chosen values for performing quantum computation using the 4-qubit loop graph is $\theta_1 = \theta_2 = \pi/2$. The matrix of $HR(\pi/2)$ turns out to be the same as the matrix of measuring the polarization qubits in state R, right-circular, using the QWP and HWP that are in place for polarization tomography. The matrix is

$$HR(\pi/2) = \frac{1}{\sqrt{2}} \begin{pmatrix} 1 & i \\ 1 & i \end{pmatrix} \tag{6.7}$$

and corresponds to the combination $HWP(22.5) \cdot QWP(0)$. The theoretical output of this computation is $\frac{|t\rangle\otimes(|r\rangle+i|t\rangle)}{\sqrt{2}}$, which is a fully separable state and has concurrence and Tangle equal 0. The density matrix associated to this state, written in basis in the order $|rr\rangle$, $|rt\rangle$, $|tr\rangle$ and $|tt\rangle$, where t and r respectively stand for $transmission$ and $reflection$ is

$$\text{TargetState}_{\frac{\pi}{2},\frac{\pi}{2}} = \begin{pmatrix} 0 & 0 & 0 & 0 \\ 0 & 0 & 0 & 0 \\ 0 & 0 & 0.5 & -0.5i \\ 0 & 0 & 0.5i & 0.5 \end{pmatrix}. \tag{6.8}$$

The reconstructed matrix using Maximum Likelihood is

$$C_{\frac{\pi}{2},\frac{\pi}{2}} = \begin{pmatrix} 0.0148 & 0.0094 - 0.0199i & 0.0796 - 0.0114i & -0.0190 - 0.0743i \\ 0.0094 + 0.0199i & 0.0731 & 0.0921 + 0.0684i & 0.0554 - 0.0944i \\ 0.0796 + 0.0114i & 0.0921 - 0.0684i & 0.4774 & -0.0492 - 0.4529i \\ -0.0190 + 0.0743i & 0.0554 + 0.0944i & -0.0492 + 0.4529i & 0.4347 \end{pmatrix}. \tag{6.9}$$

This output has the purity of 0.91 and also a fidelity of 0.91 with the target state. The concurrence of this state is 0.18 and its tangle is 0.07.

Fig. 6.14 shows the real and imaginary parts of the density matrix, reconstructed by Maximum Likelihood.

6.6.3 Results for the Quantum Computation Corresponding to $\theta_1 = 0$ and $\theta_2 = \pi/2$

Another value chosen for the measurement angles is $\theta_1 = 0$ and $\theta_2 = \pi/2$. The matrix of $HR(0)$ is

$$HR(0) = \frac{1}{\sqrt{2}} \begin{pmatrix} 1 & 1 \\ 1 & -1 \end{pmatrix} \tag{6.10}$$

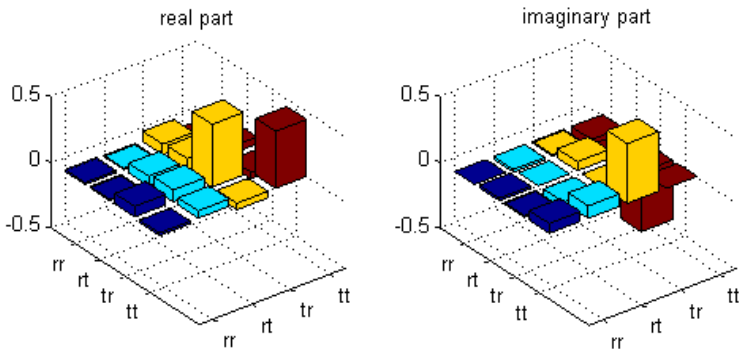

Figure 6.14 The real and imaginary parts of the density matrix, reconstructed by Maximum Likelihood, that is the output of the computation choosing $\theta_1 = \theta_2 = \pi/2$.

and corresponds to $HWP(22.5)$. Hence, for this measurement the quarter-wave plate of interferometer A is taken out of the setup. The theoretical output of this computation is $(\frac{|r\rangle - i|t\rangle}{\sqrt{2}}) \otimes (\frac{|r\rangle + i|t\rangle}{\sqrt{2}})$, which is a fully separable state and has concurrence and tangle equal 0. The density matrix associated to this state, written in basis in the order $|rr\rangle$, $|rt\rangle$, $|tr\rangle$ and $|tt\rangle$, where t and r is

$$\text{TargetState}_{0,\frac{\pi}{2}} = \frac{1}{4}\begin{pmatrix} 1 & -i & i & 1 \\ i & 1 & -1 & i \\ -i & -1 & 1 & -i \\ 1 & -i & i & 1 \end{pmatrix}. \tag{6.11}$$

The reconstructed matrix using Maximum Likelihood is

$$C_{0,\frac{\pi}{2}} = \begin{pmatrix} 0.2726 & -0.0026 - 0.1900i & 0.0843 + 0.2334i & 0.2493 - 0.0737i \\ -0.0026 + 0.1900i & 0.1347 & -0.1542 + 0.0630i & 0.0565 + 0.1654i \\ 0.0843 - 0.2334i & -0.1542 - 0.0630i & 0.2826 & 0.0186 - 0.2954i \\ 0.2493 + 0.0737i & 0.0565 - 0.1654i & 0.0186 + 0.2954i & 0.3101 \end{pmatrix}. \tag{6.12}$$

This output has the purity of 0.89 and also a fidelity of 0.89 with the target state. The concurrence of this state is 0.018 and its tangle is 0.07.

Fig. 6.15 shows the real and imaginary parts of the density matrix, reconstructed by Maximum Likelihood.

6.6.4 Results for the Quantum Computation Corresponding to $\theta_1 = 0$ and $\theta_2 = 0$

The last value chosen for the measurement angles is $\theta_1 = 0$ and $\theta_2 = 0$. For this measurement, both quarter-wave plates of polarization tomography in interferometers are taken out of the setup. The theoretical output of this computation is $\frac{|rr\rangle + |rt\rangle - |tr\rangle + |tt\rangle}{2}$, which is

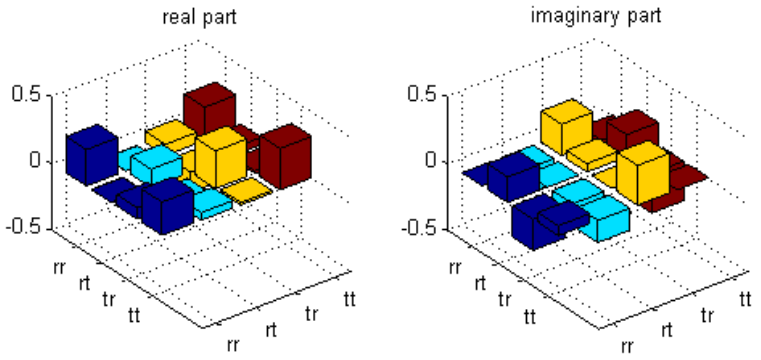

Figure 6.15 The real and imaginary parts of the density matrix, reconstructed by Maximum Likelihood, that is the output of the computation choosing $\theta_1 = 0$ and $\theta_2 = \frac{\pi}{2}$.

a maximally entangled state and has concurrence and tangle equal 1. The density matrix associated to this state, written in basis in the order $|rr\rangle$, $|rt\rangle$, $|tr\rangle$ and $|tt\rangle$, where t and r is

$$\text{TargetState}_{0,0} = \frac{1}{4}\begin{pmatrix} 1 & 1 & -1 & 1 \\ 1 & 1 & -1 & 1 \\ -1 & -1 & 1 & -1 \\ 1 & 1 & -1 & 1 \end{pmatrix}. \tag{6.13}$$

The reconstructed matrix using Maximum Likelihood is

$$C_{0,0} = \begin{pmatrix} 0.0.3091 & 0.2324 + 0.1027i & -0.2292 + 0.0474i & 0.2672 + 0.0484i \\ 0.2324 - 0.1027i & 0.2644 & -0.1577 + 0.0959i & 0.2112 - 0.0348i \\ -0.2292 - 0.0474i & -0.1577 - 0.0959i & 0.1819 & -0.1956 - 0.0788i \\ 0.2672 - 0.0484i & 0.2112 + 0.0348i & -0.1956 + 0.0788i & 0.2447 \end{pmatrix}. \tag{6.14}$$

This output has the purity of 0.89 and also a fidelity of 0.90 with the target state. The Concurrence of this state is 0.91 and its tangle is 0.87, which given the purity and fidelity of the state testify the pure portion of state being close to maximally entangled. Fig. 6.16 shows the real and imaginary parts of the density matrix, reconstructed by Maximum Likelihood.

6.6.5 Discussion

The results of quantum computation we detailed in the previous 3 subsections are summarized in figure 6.17.

These results of quantum computation agree with the expected target results, within experimental errors. For the cases when the output should be completely separable the concurrence and tangle are close to zero and for the case when the output state is maximally entangled, the values of concurrence and tangle reflect this fact.

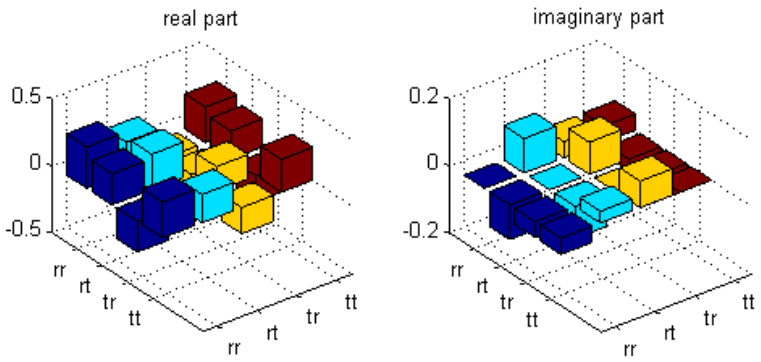

Figure 6.16 The real and imaginary parts of the density matrix, reconstructed by Maximum Likelihood, that is the output of the computation choosing $\theta_1 = 0$ and $\theta_2 = 0$.

Measurement Angles Θ_1, Θ_2	Maximum Likelihood Purity	Fidelity of Experimental Results with Target State	Fidelity of Simulated Results with Target State
0, 0	0.89	0.9	0.75
0, π/2	0.89	0.89	0.74
π/2 , π/2	0.91	0.91	0.73

	Concurrence - Experiment	Concurrence-Theory	Tangle - experiment	Tangle-theory
Source:	0.82	1	0.75	1
Θ1 = 0, Θ2 = 0	0.91	1	0.87	1
Θ1 = 0, Θ2 = π/2	0.18	0	0.07	0
Θ1 = π/2 , Θ2 = π/2	0.18	0	0.07	0

Figure 6.17 The summary of the results of quantum computation using the 4-qubit loop graph. The Measurement angles refer to the measurement bases of polarization qubits.

These are the results of the computation using the 4-qubit graph state, which agree with the expected results from the circuit equivalent to this graph (Fig. 4.9(c)) that was found using generalized flow. This demonstrates that the 4-qubit loop graph that is experimentally realized indeed performs the same computation as this circuit. On the other hand, this circuit is equivalent to the circuit with the time-like loop that can be written as the Bennett-Schumacher-Svetlichny circuit shown in Fig. 4.9(d). Hence the experiment successfully simulates a closed time-like curve, without the post-selection that is necessary in the BSS model.

Chapter 7

Conclusion

7.1 Summary of Work

The one-way model of quantum computation is a promising method for the realization of a quantum computer. Photonics systems have proven to be the most readily available for the implementation of this model. Such implementations combine the use of fusion gates for the production of graph states and proccessing, which requires feed-forward of measurement results. Thus, a scheme is proposed to use time-bin qubits in optical fibres for the realization of one-way QC. The use of optical fibres provides a natural place to keep the photons during the production of the graph by the fusion gates and, later on, during proccessing of the measurement results and determination and setting of future measurement bases for computation. All necessary gates for the fusion gates and arbitrary single qubit operations are studied and described in detail. The methods described here can be used not only in optical fibres, but also in the new photonic integrated devices.

The experimental implementation of the 4-qubit loop graph combined two different degrees of freedom of photons. A novel method was used to perform a controlled-Z operation between the polarization degree of freedom of one photon and the path of another one. This method is the only reported one that used only linear optical elements for this purpose.

Simulations of the effect of realistic experimental errors on the creation of this 4-qubit state showed that inaccuracies in the angle of the waveplates used to create the graph state and in their retardance reduce the fidelity of the state with the target state by 2%. Inaccurate settings of interferometer phases can reduce the fidelity further down by 7%. The imperfect visibility of the interferometers, which is about 93%, can further reduce the purity of the state and the fidelity with the target state. We see that the effects of these errors manifest themselves by different amount for different measurement settings of polarization qubits.

Due to the high sensitivity of the source to temperature fluctuations, the polarization entangled photon pairs from the source have purity of about 85% and the fidelity with the target state of 87% to 91%. A simulation that combines these results with the unbalanced loss for different arms of interferometers and imperfect visibility of interferometers show these error can reduce the fidelity of the state to as low as 74%. Taking all these sources of errors

into account, one can expect the lower bound of the experimental fidelity with target states to be less than 70%.

For the experimental characterization of the created state, $16 \times 16 = 256$ measurements are performed. These measurements include 16 measurement basis settings on polarization qubits and, for each of these settings, there are 16 basis settings for path qubits. For each polarization basis setting, 2-qubit tomography is performed on path qubits and the corresponding density matrix is reconstructed using the methods of Linear Inversion and Maximum Likelihood. The experimental results are then compared to the results from the ideal target state predicted from the simulation of the experiment. The purities of these reconstructed density matrices range from 0.72 to 1. The fidelities with the ideal target sate range from 0.54 to 0.96. Taking the experimental errors into account, these values fall within the expected results and show that we have created the 4-qubit graph state with a reasonable overlap with the target state.

Using the created graph state as the initial resource for one-way quantum computing, three computations corresponding to three different choices of measurement basis for polarization qubits are performed. The results of these computations are in agreement with the expected target state with fidelities of 90% and have purities of 0.90. These results compare favourably with the state of the art results of proof of principle experiments.

7.2 Limitations of the Proposed Solution

The main difficulty for the realization of a graph state using the path DOF of photons in free space is achieving the requirements for the stability of the interferometers, their visibility for single photons and accurate setting interferometer phases. Using optical fibres or integrated photonic devices can overcome this issue.

Using entangled photons with longer coherence length helps with balancing the optical paths of the interferometers. However, the source used for this experiment is highly sensitive to the temperature of the environment. As a result, the purity and fidelity of the created state was not very high. Improving the source will give a general improvement over the result.

7.3 Future Work

The work reported herein suggests three different areas of research to be further explored. One is related to the time-like loops and their properties. Two are related to photonic implementations of quantum computation.

The 4-qubit loop graph is the first experimental realization of a system that can simulate time-like loops in a model equivalent to that of Bennett, Schumacher and Svetlichny, but without using post-selection. This experiment opens new avenues for at least two different interesting ideas to be explored in this regard. The first is the study of time-like loops when the qubit entering the loop interacts with another qubit that respects the regular passage of time. The second is studying how the paradoxes, such as the grand-father paradox or the information paradox, manifest themselves in the created 4-qubit loop graph and whether the results agree with that of Lloyd *et al.* (2011).

In terms of photonic implementations of quantum computation, using more than one degree of freedom of photons allows one to reduce the required number of photons for a computation. Hence, it is desirable to create graph states using more than one DOF. A fusion gate for fusing hyper-enganled photons is proposed Joo *et al.* (2007), however, its success probability it too low for a realistic implementation. It is interesting to see if it is possible to create larger graph states with more than one DOF of photons, using only the fusion gates for polarization DOF and linear optical elements to add the other DOFs.

Another intersting possibility is the combination of the one-way model with the circuit model of QC through the combination of different DOFs of photons. For example, one can break up a quantum computation so that it can use a combination of the one-way model that can be implemented using polarization DOFs and the circuit model that can be added to the polarization entangled state using other DOFs of the photons. The questions to answer here are what is the best way to combine these two models and what are the properties of this type of computation in terms of fault tolerance.

The work reported here includes not only a new proposal for the realization of the one-way model of QC in photonic systems and a novel exprimental method for the realization of a graph with loop geometry, it also announces interesting new directions to be explored in the contex of time-like loops, the realization of larger graphs using more than one DOF of photons and even a completely novel method of quantum computation for photonic systems that combines the one-way model with the circuit model of QC.

References

ALTEPETER, J. B., JEFFREY, E. R. et KWIAT, P. G. (2010). *Advances in Atomic, Molecular, and Optical Physics*. Elsevier.

BENNETT, C. H. et SCHUMACHER, B. (2002).

BENNETT, C. H. et SCHUMACHER, B. (2004).

BLOCH, I. (2008). Quantum coherence and entanglement with ultracold atoms in optical lattices. *Nature*, pp. 1016–1022.

BRENDEL, J., GISIN, N., TITTEL, W. et ZBINDEN, H. (1999). Pulsed energy-time entangled twin-photon source for quantum communication. *PHYS.REV.LETT.*, 82, 2594.

BROWNE, D. E., KASHEFI, E., MHALLA, M. et PERDRIX, S. (2007). Generalized flow and determinism in measurement-based quantum computation. *NEW J.PHYS.*, 9, 250.

BROWNE, D. E. et RUDOLPH, T. (2005). Resource-efficient linear optical quantum computation. *Phys. Rev. Lett.*, 95, 010501.

CATHERINE HOLLOWAY, EVAN MEYER-SCOTT, C. E. et JENNEWEIN, T. (2011). Quantum entanglement distribution with 810 nm photons through active telecommunication fibers. *Opt. Express*, 19, 20597–20603.

CHEN, K., LI, C.-M., ZHANG, Q., CHEN, Y.-A., GOEBEL, A., CHEN, S., MAIR, A. et PAN, J.-W. (2007). Experimental realization of one-way quantum computing with two-photon four-qubit cluster states. *Phys. Rev. Lett.*, 99, 120503.

COLLETT, E. (2005). *Field Guide to Polarization*. SPIE Vol. FG05.

DANOS, V. et KASHEFI, E. (2006). Determinism in the one-way model. *Phys. Rev. A*, 74, 052310.

DANOS, V., KASHEFI, E. et PANANGADEN, P. (2007). The measurement calculus. *J. ACM*, 54.

DIAS DA SILVA, R., GALVÃO, E. F. et KASHEFI, E. (2011). Closed timelike curves in measurement-based quantum computation. *Phys. Rev. A*, 83, 012316.

DÜR, W. et BRIEGEL, H.-J. (2004). Stability of macroscopic entanglement under decoherence. *Phys. Rev. Lett.*, 92, 180403.

FEYNMAN, R. (1982). Simulating physics with computers. *International Journal of Theoretical Physics*, 21, 467–488. 10.1007/BF02650179.

GAO, W.-B., FOWLER, A. G., RAUSSENDORF, R., YAO, X.-C., LU, H., XU, P., LU, C.-Y., PENG, C.-Z., DENG, Y., CHEN, Z.-B. et PAN, J.-W. (2009). Experimental demonstration of topological error correction.

GERRY, C. et KNIGHT, P. (2004). *Introductory Quantum Optics*. Cambridge University Press.

HEIN, M., DUR, W., EISERT, J., RAUSSENDORF, R., DEN NEST, M. V. et BRIEGEL, H. J. (2006). Entanglement in graph states and its applications.

HÜBEL, H., VANNER, M. R., LEDERER, T., BLAUENSTEINER, B., LORÜNSER, T., POPPE, A. et ZEILINGER, A. (2007). High-fidelity transmission of polarization encoded qubits from an entangled source over 100 km of fiber. *Opt. Express*, 15, 7853–7862.

JAMES, D. F. V., KWIAT, P. G., MUNRO, W. J. et WHITE, A. G. (2001). Measurement of qubits. *Phys. Rev. A*, 64, 052312.

JENNEWEIN, T., BARBIERI, M. et WHITE, A. G. (2011). Single-photon device requirements for operating linear optics quantum computing outside the post-selection basis. *Journal of Modern Optics*, 58, 276–287.

JEREMY L. O'BRIEN, A. F. . J. V. (2009). Photonic quantum technologies. *Nature Photonics*, pp. 687–695.

JOO, J., KNIGHT, P. L., O'BRIEN, J. L. et RUDOLPH, T. (2007). One-way quantum computation with four-dimensional photonic qudits. *Physical Review A*, 76, 1–10.

JU, C., ZHU, J., PENG, X., CHONG, B., ZHOU, X. et DU, J. (2010). Experimental demonstration of deterministic one-way quantum computation on a nmr quantum computer. *Phys. Rev. A*, 81, 012322.

KOK, P., MUNRO, W. J., NEMOTO, K., RALPH, T. C., DOWLING, J. P. et MILBURN, G. J. (2007). Linear optical quantum computing with photonic qubits. *Rev. Mod. Phys.*, 79, 135–174.

KWIAT, P. G., MATTLE, K., WEINFURTER, H., ZEILINGER, A., SERGIENKO, A. V. et SHIH, Y. (1995). New high-intensity source of polarization-entangled photon pairs. *Phys. Rev. Lett.*, 75, 4337–4341.

KWIAT, P. G., WAKS, E., WHITE, A. G., APPELBAUM, I. et EBERHARD, P. H. (1999). Ultrabright source of polarization-entangled photons. *Phys. Rev. A*, 60, R773–R776.

LAING, A., PERUZZO, A., POLITI, A., VERDE, M. R., HALDER, M., RALPH, T. C., THOMPSON, M. G. et O'BRIEN, J. L. (2010). High-fidelity operation of quantum photonic circuits. *Applied Physics Letters*, 97, 211109.

LEE, S. M., PARK, H. S., CHO, J., KANG, Y., LEE, J. Y., KIM, H., LEE, D.-H. et CHOI, S.-K. (2011). Experimental realization of a four-photon seven-qubit graph state for one-way quantum computation.

LLOYD, S., MACCONE, L., GARCIA-PATRON, R., GIOVANNETTI, V., SHIKANO, Y., PIRANDOLA, S., ROZEMA, L. A., DARABI, A., SOUDAGAR, Y., SHALM, L. K. et STEINBERG, A. M. (2011). Closed timelike curves via postselection: Theory and experimental test of consistency. *Phys. Rev. Lett.*, 106, 040403.

LU, C.-Y., ZHOU, X.-Q., GUHNE, O., BO GAO, W., ZHANG, J., YUAN, Z.-S., GOEBEL, A., YANG, T. et PAN, J.-W. (2007). Experimental entanglement of six photons in graph states. *NATURE PHYSICS*, 3, 91.

MARCIKIC, I., DE RIEDMATTEN, H., TITTEL, W., ZBINDEN, H., LEGRÉ, M. et GISIN, N. (2004). Distribution of time-bin entangled qubits over 50 km of optical fiber. *Phys. Rev. Lett.*, 93, 180502.

MENICUCCI, N. C., FLAMMIA, S. T. et PFISTER, O. (2008). One-way quantum computing in the optical frequency comb. *Phys. Rev. Lett.*, 101, 130501.

NIELSEN, A. M. (2006). Cluster-state quantum computation. *Rep. Math. Phys.*, 57, pp. 147–161.

NIELSEN, M. A. et CHUANG, I. L. (2000). *Quantum Computation and Quantum Information*. Cambridge University Press.

PREVEDEL, R., WALTHER, P., TIEFENBACHER, F., BÃHI, P., KALTENBAEK, R., JENNEWEIN, T. et ZEILINGER, A. (2007). High-speed linear optics quantum computing using active feed-forward. *Nature*, pp. 65–69.

RAUSSENDORF, R. et BRIEGEL, H. J. (2001). A one-way quantum computer. *Phys. Rev. Lett.*, 86, 5188–5191.

RAUSSENDORF, R., BROWNE, D. E. et BRIEGEL, H. J. (2003). Measurement-based quantum computation on cluster states. *Phys. Rev. A*, 68, 022312.

SHOR, P. (1994). Algorithms for quantum computation: discrete logarithms and factoring. *Foundations of Computer Science, 1994 Proceedings., 35th Annual Symposium on*. 124 – 134. 10.1109/SFCS.1994.365700.

SOUDAGAR, Y., BUSSIÈRES, F., BERLÍN, G., LACROIX, S., FERNANDEZ, J. M. et GODBOUT, N. (2007). Cluster-state quantum computing in optical fibers. *J. Opt. Soc. Am. B*, 24, 226–230.

STEVENSON, R. M., YOUNG, R. J., ATKINSON, P., COOPER, K., RITCHIE, D. A. et SHIELDS, A. J. (2006). A semiconductor source of triggered entangled photon pair. *Nature*, 439, pp. 179–182.

SVETLICHNY, G. (2009). Effective quantum time travel.

SVETLICHNY, G. (2011). Time travel: Deutsch vs. teleportation. *International Journal of Theoretical Physics*, 1–12. 10.1007/s10773-011-0973-x.

VALLONE, G., CECCARELLI, R., DE MARTINI, F. et MATALONI, P. (2008a). Hyper-entanglement witness. *Phys. Rev. A*, 78, 062305.

VALLONE, G., DONATI, G., BRUNO, N., CHIURI, A. et MATALONI, P. (2010a). Experimental realization of the deutsch-jozsa algorithm with a six-qubit cluster state. *PHYS.REV.A*, 81, 050302.

VALLONE, G., DONATI, G., CECCARELLI, R. et MATALONI, P. (2010b). Six-qubit two-photon hyperentangled cluster states: Characterization and application to quantum computation. *Phys. Rev. A*, 81, 052301.

VALLONE, G., POMARICO, E., DE MARTINI, F. et MATALONI, P. (2008b). Active one-way quantum computation with two-photon four-qubit cluster states. *Phys. Rev. Lett.*, 100, 160502.

VALLONE, G., POMARICO, E., DE MARTINI, F. et MATALONI, P. (2008c). One-way quantum computation with two-photon multiqubit cluster states. *Phys. Rev. A*, 78, 042335.

VALLONE, G., POMARICO, E., MATALONI, P., DE MARTINI, F. et BERARDI, V. (2007). Realization and characterization of a two-photon four-qubit linear cluster state. *Phys. Rev. Lett.*, 98, 180502.

WALTHER, P., RESCH, K. J., RUDOLPH, T., SCHENCK, E., WEINFURTER, H., VEDRAL, V., ASPELMEYER, M. et ZEILINGER, A. (2005). Experimental one-way quantum computing. *Nature*, pp. 169–176.

WOLFGRAMM, F., XING, X., CERÈ, A., PREDOJEVIĆ, A., STEINBERG, A. M. et MITCHELL, M. W. (2008). Bright filter-free source of indistinguishable photon pairs. *Opt. Express*, 16, 18145–18151.

WOOTTERS, W. K. (1998). Entanglement of formation of an arbitrary state of two qubits. *Phys. Rev. Lett.*, 80, 2245–2248.

ZHAO, Z., CHEN, Y.-A., ZHANG, A.-N., YANG, T., BRIEGEL, H. J. et PAN, J.-W. (2004). Experimental demonstration of five-photon entanglement and open-destination teleportation. *Nature*, pp. 54–58.

Appendix A

The equivalency of the circuit with cNOT and the BSS circuit

Here we perform the calculations to show the output of the circuit with cNOT, equivalent to the loop circuit, is the same as the output of the circuit with BSS, when post-selection is successful.

Tensor Product

```
> with(LinearAlgebra):
> Kron:=proc(A::Matrix,B::Matrix)
  local M,P,i,j;
  M:=Matrix(RowDimension(A)*RowDimension(B),ColumnDimension(A)*ColumnDimension
  (B)):
  P:=Matrix(RowDimension(B),ColumnDimension(B)):
  for i to RowDimension(A) do
  for j to ColumnDimension(A) do
  P:=ScalarMultiply(B,A[i,j]):
  M[1+(i-1)*RowDimension(B)..(i-1)*RowDimension(B)+RowDimension(B),1+(j-1)*
  ColumnDimension(B)..(j-1)*ColumnDimension(B)+ColumnDimension(B)]:=P:
  od
  od:
  M;
  end proc:
```

Definition of gates:

```
> Id := Matrix([[1 , 0], [0,  1]]);
```

$$Id := \begin{bmatrix} 1 & 0 \\ 0 & 1 \end{bmatrix} \tag{1}$$

```
> cZ := Matrix([[1 , 0, 0, 0], [0,  1, 0, 0], [0, 0, 1, 0], [0, 0, 0, -1]]);
```

$$cZ := \begin{bmatrix} 1 & 0 & 0 & 0 \\ 0 & 1 & 0 & 0 \\ 0 & 0 & 1 & 0 \\ 0 & 0 & 0 & -1 \end{bmatrix} \tag{2}$$

```
> cNOT := Matrix([[1 , 0, 0, 0], [0,  1, 0, 0], [0, 0, 0, 1], [0, 0, 1, 0]]);
```

$$cNOT := \begin{bmatrix} 1 & 0 & 0 & 0 \\ 0 & 1 & 0 & 0 \\ 0 & 0 & 0 & 1 \\ 0 & 0 & 1 & 0 \end{bmatrix} \tag{3}$$

```
> swap23 := Matrix([[1 , 0, 0, 0], [0,  0, 1, 0], [0, 1, 0, 0], [0, 0, 0, 1]]);
```

$$swap23 := \begin{bmatrix} 1 & 0 & 0 & 0 \\ 0 & 0 & 1 & 0 \\ 0 & 1 & 0 & 0 \\ 0 & 0 & 0 & 1 \end{bmatrix} \tag{4}$$

```
> had := 1/sqrt(2) Matrix([[1, 1], [1, -1]]);
```

$$had := \begin{bmatrix} \frac{1}{2}\sqrt{2} & \frac{1}{2}\sqrt{2} \\ \frac{1}{2}\sqrt{2} & -\frac{1}{2}\sqrt{2} \end{bmatrix} \quad (5)$$

> $ret := Matrix([[1, 0], [0, \exp(I \cdot \text{theta})]]);$

$$ret := \begin{bmatrix} 1 & 0 \\ 0 & e^{I\theta} \end{bmatrix} \quad (6)$$

> $R := \text{theta} \rightarrow \frac{1}{\text{sqrt}(2)} \cdot (Matrix([[1, \exp(I \cdot \text{theta})], [1, -\exp(I \cdot \text{theta})]]));$

$$R := \theta \rightarrow \frac{Matrix([[1, e^{I\theta}], [1, -e^{I\theta}]])}{\sqrt{2}} \quad (7)$$

The unitary corresponding to the circuit with cNOT:

> $U2 := cNOT.Kron(R(theta2).R(theta1), Id).cZ;$

$$U2 := \begin{bmatrix} \frac{1}{2} + \frac{1}{2}e^{I\theta 2} & 0 & \frac{1}{2}e^{I\theta 1} - \frac{1}{2}e^{I\theta 2}e^{I\theta 1} & 0 \\ 0 & \frac{1}{2} + \frac{1}{2}e^{I\theta 2} & 0 & -\frac{1}{2}e^{I\theta 1} + \frac{1}{2}e^{I\theta 2}e^{I\theta 1} \\ 0 & \frac{1}{2} - \frac{1}{2}e^{I\theta 2} & 0 & -\frac{1}{2}e^{I\theta 1} - \frac{1}{2}e^{I\theta 2}e^{I\theta 1} \\ \frac{1}{2} - \frac{1}{2}e^{I\theta 2} & 0 & \frac{1}{2}e^{I\theta 1} + \frac{1}{2}e^{I\theta 2}e^{I\theta 1} & 0 \end{bmatrix} \quad (8)$$

Preparing the input qubit:

> $psi1 := Matrix([[alpha1], [beta1]]);$

$$\psi 1 := \begin{bmatrix} \alpha 1 \\ \beta 1 \end{bmatrix} \quad (9)$$

> $plus := \frac{1}{\text{sqrt}(2)} Matrix([[1], [1]]);$

$$plus := \begin{bmatrix} \frac{1}{2}\sqrt{2} \\ \frac{1}{2}\sqrt{2} \end{bmatrix} \quad (10)$$

> $input := Kron(psi1, plus);$

(11)

$$input := \begin{bmatrix} \frac{1}{2}\,\alpha 1\,\sqrt{2} \\ \frac{1}{2}\,\alpha 1\,\sqrt{2} \\ \frac{1}{2}\,\beta 1\,\sqrt{2} \\ \frac{1}{2}\,\beta 1\,\sqrt{2} \end{bmatrix} \tag{11}$$

The output from the circuit with cNOT:

```
> U2.input;
```

$$\begin{bmatrix} \frac{1}{2}\left(\frac{1}{2}+\frac{1}{2}\,e^{I\theta 2}\right)\alpha 1\,\sqrt{2}+\frac{1}{2}\left(\frac{1}{2}\,e^{I\theta 1}-\frac{1}{2}\,e^{I\theta 2}\,e^{I\theta 1}\right)\beta 1\,\sqrt{2} \\ \frac{1}{2}\left(\frac{1}{2}+\frac{1}{2}\,e^{I\theta 2}\right)\alpha 1\,\sqrt{2}+\frac{1}{2}\left(-\frac{1}{2}\,e^{I\theta 1}+\frac{1}{2}\,e^{I\theta 2}\,e^{I\theta 1}\right)\beta 1\,\sqrt{2} \\ \frac{1}{2}\left(\frac{1}{2}-\frac{1}{2}\,e^{I\theta 2}\right)\alpha 1\,\sqrt{2}+\frac{1}{2}\left(-\frac{1}{2}\,e^{I\theta 1}-\frac{1}{2}\,e^{I\theta 2}\,e^{I\theta 1}\right)\beta 1\,\sqrt{2} \\ \frac{1}{2}\left(\frac{1}{2}-\frac{1}{2}\,e^{I\theta 2}\right)\alpha 1\,\sqrt{2}+\frac{1}{2}\left(\frac{1}{2}\,e^{I\theta 1}+\frac{1}{2}\,e^{I\theta 2}\,e^{I\theta 1}\right)\beta 1\,\sqrt{2} \end{bmatrix} \tag{12}$$

The circuit with BSS. Preparation of input:

```
> input4 := Kron(Kron(Kron(plus, plus), psi1), plus);
```

$$input4 := \begin{bmatrix} 16\ x\ 1\ Matrix \\ Data\ Type:\ anything \\ Storage:\ rectangular \\ Order:\ Fortran\_order \end{bmatrix} \tag{13}$$

The unitary that the circuit applies to the input, before post selection:

```
> U4 := Kron(Kron(Kron(had, had), Id), Id).Kron(Kron(cZ, Id), Id).Kron(Kron(Kron(Id,
      R(theta2).R(theta1)), Id), Id).Kron(Kron(Id, cZ), Id).Kron(Kron(Id, swap23), Id)
      .Kron(cZ, cZ);
```

$$U4 := \begin{bmatrix} 16\ x\ 16\ Matrix \\ Data\ Type:\ anything \\ Storage:\ rectangular \\ Order:\ Fortran\_order \end{bmatrix} \tag{14}$$

```
> out := evalm(U4.input4);
```

$$out := \begin{bmatrix}
\frac{1}{8}\,\alpha 1\sqrt{2} + \frac{1}{8}\,e^{I\theta 1}\,\beta 1\sqrt{2} + \frac{1}{8}\,e^{I\theta 2}\,\alpha 1\sqrt{2} - \frac{1}{8}\,e^{I\theta 2}\,e^{I\theta 1}\,\beta 1\sqrt{2} \\
\frac{1}{8}\,\alpha 1\sqrt{2} - \frac{1}{8}\,e^{I\theta 1}\,\beta 1\sqrt{2} + \frac{1}{8}\,e^{I\theta 2}\,\alpha 1\sqrt{2} + \frac{1}{8}\,e^{I\theta 2}\,e^{I\theta 1}\,\beta 1\sqrt{2} \\
\frac{1}{8}\,\alpha 1\sqrt{2} - \frac{1}{8}\,e^{I\theta 1}\,\beta 1\sqrt{2} - \frac{1}{8}\,e^{I\theta 2}\,\alpha 1\sqrt{2} - \frac{1}{8}\,e^{I\theta 2}\,e^{I\theta 1}\,\beta 1\sqrt{2} \\
\frac{1}{8}\,\alpha 1\sqrt{2} + \frac{1}{8}\,e^{I\theta 1}\,\beta 1\sqrt{2} - \frac{1}{8}\,e^{I\theta 2}\,\alpha 1\sqrt{2} + \frac{1}{8}\,e^{I\theta 2}\,e^{I\theta 1}\,\beta 1\sqrt{2} \\
\frac{1}{8}\,\alpha 1\sqrt{2} + \frac{1}{8}\,e^{I\theta 1}\,\beta 1\sqrt{2} + \frac{1}{8}\,e^{I\theta 2}\,\alpha 1\sqrt{2} - \frac{1}{8}\,e^{I\theta 2}\,e^{I\theta 1}\,\beta 1\sqrt{2} \\
\frac{1}{8}\,\alpha 1\sqrt{2} - \frac{1}{8}\,e^{I\theta 1}\,\beta 1\sqrt{2} + \frac{1}{8}\,e^{I\theta 2}\,\alpha 1\sqrt{2} + \frac{1}{8}\,e^{I\theta 2}\,e^{I\theta 1}\,\beta 1\sqrt{2} \\
\frac{1}{8}\,e^{I\theta 2}\,\alpha 1\sqrt{2} + \frac{1}{8}\,e^{I\theta 2}\,e^{I\theta 1}\,\beta 1\sqrt{2} - \frac{1}{8}\,\alpha 1\sqrt{2} + \frac{1}{8}\,e^{I\theta 1}\,\beta 1\sqrt{2} \\
\frac{1}{8}\,e^{I\theta 2}\,\alpha 1\sqrt{2} - \frac{1}{8}\,e^{I\theta 2}\,e^{I\theta 1}\,\beta 1\sqrt{2} - \frac{1}{8}\,\alpha 1\sqrt{2} - \frac{1}{8}\,e^{I\theta 1}\,\beta 1\sqrt{2} \\
\frac{1}{8}\,\alpha 1\sqrt{2} + \frac{1}{8}\,e^{I\theta 1}\,\beta 1\sqrt{2} - \frac{1}{8}\,e^{I\theta 2}\,\alpha 1\sqrt{2} + \frac{1}{8}\,e^{I\theta 2}\,e^{I\theta 1}\,\beta 1\sqrt{2} \\
\frac{1}{8}\,\alpha 1\sqrt{2} - \frac{1}{8}\,e^{I\theta 1}\,\beta 1\sqrt{2} - \frac{1}{8}\,e^{I\theta 2}\,\alpha 1\sqrt{2} - \frac{1}{8}\,e^{I\theta 2}\,e^{I\theta 1}\,\beta 1\sqrt{2} \\
\frac{1}{8}\,\alpha 1\sqrt{2} - \frac{1}{8}\,e^{I\theta 1}\,\beta 1\sqrt{2} + \frac{1}{8}\,e^{I\theta 2}\,\alpha 1\sqrt{2} + \frac{1}{8}\,e^{I\theta 2}\,e^{I\theta 1}\,\beta 1\sqrt{2} \\
\frac{1}{8}\,\alpha 1\sqrt{2} + \frac{1}{8}\,e^{I\theta 1}\,\beta 1\sqrt{2} + \frac{1}{8}\,e^{I\theta 2}\,\alpha 1\sqrt{2} - \frac{1}{8}\,e^{I\theta 2}\,e^{I\theta 1}\,\beta 1\sqrt{2} \\
\frac{1}{8}\,e^{I\theta 2}\,\alpha 1\sqrt{2} - \frac{1}{8}\,e^{I\theta 2}\,e^{I\theta 1}\,\beta 1\sqrt{2} - \frac{1}{8}\,\alpha 1\sqrt{2} - \frac{1}{8}\,e^{I\theta 1}\,\beta 1\sqrt{2} \\
\frac{1}{8}\,e^{I\theta 2}\,\alpha 1\sqrt{2} + \frac{1}{8}\,e^{I\theta 2}\,e^{I\theta 1}\,\beta 1\sqrt{2} - \frac{1}{8}\,\alpha 1\sqrt{2} + \frac{1}{8}\,e^{I\theta 1}\,\beta 1\sqrt{2} \\
\frac{1}{8}\,\alpha 1\sqrt{2} - \frac{1}{8}\,e^{I\theta 1}\,\beta 1\sqrt{2} + \frac{1}{8}\,e^{I\theta 2}\,\alpha 1\sqrt{2} + \frac{1}{8}\,e^{I\theta 2}\,e^{I\theta 1}\,\beta 1\sqrt{2} \\
\frac{1}{8}\,\alpha 1\sqrt{2} + \frac{1}{8}\,e^{I\theta 1}\,\beta 1\sqrt{2} + \frac{1}{8}\,e^{I\theta 2}\,\alpha 1\sqrt{2} - \frac{1}{8}\,e^{I\theta 2}\,e^{I\theta 1}\,\beta 1\sqrt{2}
\end{bmatrix} \tag{15}$$

The first 4 entries in this output correspond to post-selecting on both detectors that perform the Bell projection measurement detecting zeros. These are the same as the output of the circuit with cNOT. This shows that the circuit with cNOT is equivalent to the circuit with BSS, , with the normalization factor taken into account.

Appendix B

Simulation of the Circuit Equivalent to the Loop Graph

In this appendix, we simulate the circuit that is equivalent to the computation that is being done by the loop graph. This circuit is shown in figure 5, chapter 4.

```
> Id := Matrix([[1 , 0], [0,  1]]);
```

$$Id := \begin{bmatrix} 1 & 0 \\ 0 & 1 \end{bmatrix} \tag{1}$$

```
> cZ := Matrix([[1 , 0, 0, 0], [0,  1, 0, 0], [0, 0, 1, 0], [0, 0, 0, -1]]);
```

$$cZ := \begin{bmatrix} 1 & 0 & 0 & 0 \\ 0 & 1 & 0 & 0 \\ 0 & 0 & 1 & 0 \\ 0 & 0 & 0 & -1 \end{bmatrix} \tag{2}$$

```
> cNOT := Matrix([[1 , 0, 0, 0], [0,  1, 0, 0], [0, 0, 0, 1], [0, 0, 1, 0]]);
```

$$cNOT := \begin{bmatrix} 1 & 0 & 0 & 0 \\ 0 & 1 & 0 & 0 \\ 0 & 0 & 0 & 1 \\ 0 & 0 & 1 & 0 \end{bmatrix} \tag{3}$$

```
> Hadamard := 1/sqrt(2) Matrix([[1, 1], [1, -1]]);
```

$$Hadamard := \begin{bmatrix} \frac{1}{2}\sqrt{2} & \frac{1}{2}\sqrt{2} \\ \frac{1}{2}\sqrt{2} & -\frac{1}{2}\sqrt{2} \end{bmatrix} \tag{4}$$

```
> R := theta →Matrix([[1, 0], [0, exp(I·theta)]]);
```

$$R := \theta \rightarrow Matrix\left(\left[[1, 0], \left[0, e^{I\theta}\right]\right]\right) \tag{5}$$

```
> J := theta→Hadamard.R(theta);
```

$$J := \theta \rightarrow Typesetting:\text{-}delayDotProduct(Hadamard, R(\theta)) \tag{6}$$

```
> J(theta);
```

$$\begin{bmatrix} \frac{1}{2}\sqrt{2} & \frac{1}{2}\sqrt{2}\, e^{I\theta} \\ \frac{1}{2}\sqrt{2} & -\frac{1}{2}\sqrt{2}\, e^{I\theta} \end{bmatrix} \tag{7}$$

```
> TwoQubitUnitary := cNOT.Kron(J(theta2).J(theta1), Id).cZ;
```

$$TwoQubitUnitary := \tag{8}$$

$$\begin{bmatrix} \frac{1}{2}+\frac{1}{2}e^{I\theta 2} & 0 & \frac{1}{2}e^{I\theta 1}-\frac{1}{2}e^{I\theta 2}e^{I\theta 1} & 0 \\ 0 & \frac{1}{2}+\frac{1}{2}e^{I\theta 2} & 0 & -\frac{1}{2}e^{I\theta 1}+\frac{1}{2}e^{I\theta 2}e^{I\theta 1} \\ 0 & \frac{1}{2}-\frac{1}{2}e^{I\theta 2} & 0 & -\frac{1}{2}e^{I\theta 1}-\frac{1}{2}e^{I\theta 2}e^{I\theta 1} \\ \frac{1}{2}-\frac{1}{2}e^{I\theta 2} & 0 & \frac{1}{2}e^{I\theta 1}+\frac{1}{2}e^{I\theta 2}e^{I\theta 1} & 0 \end{bmatrix}$$

> psi := Matrix([[alpha], [beta]]) : plus := $\frac{1}{\mathrm{sqrt}(2)}$ ·Matrix([[1], [1]]) :

> Input := Kron(psi, plus);

$$Input := \begin{bmatrix} \frac{1}{2}\alpha\sqrt{2} \\ \frac{1}{2}\alpha\sqrt{2} \\ \frac{1}{2}\beta\sqrt{2} \\ \frac{1}{2}\beta\sqrt{2} \end{bmatrix} \quad (9)$$

> TwoQubitUnitary.Input;

$$\begin{bmatrix} \frac{1}{2}\left(\frac{1}{2}+\frac{1}{2}e^{I\theta 2}\right)\alpha\sqrt{2}+\frac{1}{2}\left(\frac{1}{2}e^{I\theta 1}-\frac{1}{2}e^{I\theta 2}e^{I\theta 1}\right)\beta\sqrt{2} \\ \frac{1}{2}\left(\frac{1}{2}+\frac{1}{2}e^{I\theta 2}\right)\alpha\sqrt{2}+\frac{1}{2}\left(-\frac{1}{2}e^{I\theta 1}+\frac{1}{2}e^{I\theta 2}e^{I\theta 1}\right)\beta\sqrt{2} \\ \frac{1}{2}\left(\frac{1}{2}-\frac{1}{2}e^{I\theta 2}\right)\alpha\sqrt{2}+\frac{1}{2}\left(-\frac{1}{2}e^{I\theta 1}-\frac{1}{2}e^{I\theta 2}e^{I\theta 1}\right)\beta\sqrt{2} \\ \frac{1}{2}\left(\frac{1}{2}-\frac{1}{2}e^{I\theta 2}\right)\alpha\sqrt{2}+\frac{1}{2}\left(\frac{1}{2}e^{I\theta 1}+\frac{1}{2}e^{I\theta 2}e^{I\theta 1}\right)\beta\sqrt{2} \end{bmatrix} \quad (10)$$

Appendix C

Simulation of the Loop Graph and the Proof of Its Equivalency to the Circuit of Figure 4.5(c)

This appendix includes the simulation of the graph production and measurement. The detailed explanation of the simulation is in chapter 5. The results from this simulation are summarized in the last Appendix, which include the summery of all results.

Operator Definitions

transmitted path = > logical zero, then BS matrix should be defined as is. HWP and QWP are defined so that their fast axis is at vertical.

```
> zero:=Matrix([[1],[0]]);
```

$$zero := \begin{bmatrix} 1 \\ 0 \end{bmatrix} \quad \textbf{(1.1)}$$

```
> one:=Matrix([[0],[1]]);
```

$$one := \begin{bmatrix} 0 \\ 1 \end{bmatrix} \quad \textbf{(1.2)}$$

```
> BS:=(alpha2, beta2)-> Matrix([[alpha2,beta2],[beta2,-alpha2]])
  ;
```

$$BS := (\alpha 2, \beta 2) \rightarrow Matrix([[\alpha 2, \beta 2], [\beta 2, -\alpha 2]]) \quad \textbf{(1.3)}$$

```
> Id:=Matrix([[1,0],[0,1]]);
```

$$Id := \begin{bmatrix} 1 & 0 \\ 0 & 1 \end{bmatrix} \quad \textbf{(1.4)}$$

```
> HWP0:=Matrix([[I,0],[0,-I]]); #fast axis is at horizontal
```

$$HWP0 := \begin{bmatrix} I & 0 \\ 0 & -I \end{bmatrix} \quad \textbf{(1.5)}$$

```
> QWP0:=exp(I*Pi/4)*Matrix([[1,0],[0,-I]]);
```

$$QWP0 := \begin{bmatrix} \frac{\sqrt{2}}{2} + \frac{1}{2} I\sqrt{2} & 0 \\ 0 & -I\left(\frac{\sqrt{2}}{2} + \frac{1}{2} I\sqrt{2}\right) \end{bmatrix} \quad \textbf{(1.6)}$$

```
> R:=theta->Matrix([[cos(theta),sin(theta)],[-sin(theta),cos
  (theta)]]);
```

$$R := \theta \rightarrow Matrix([[\cos(\theta), \sin(\theta)], [-\sin(\theta), \cos(\theta)]]) \quad \textbf{(1.7)}$$

```
> HWP:=theta->R(-theta).HWP0.R(theta);
```

$$HWP := \theta \rightarrow R(-\theta).HWP0.R(\theta) \quad \textbf{(1.8)}$$

```
> QWP:=theta->R(-theta).QWP0.R(theta);
```

$$QWP := \theta \rightarrow R(-\theta).QWP0.R(\theta) \quad \textbf{(1.9)}$$

controlled-HWP, control = qubit 1, logical 1, target qubit 2.

```
> CHWP:=theta->Matrix([[1,0,0,0],[0,1,0,0],[0,0,cos(theta)^2*I-
  sin(theta)^2*I,2*I*cos(theta)*sin(theta)],[0,0,2*I*cos(theta)*
  sin(theta),-cos(theta)^2*I+sin(theta)^2*I]]);
```

$$CHWP := \theta \rightarrow Matrix([[1, 0, 0, 0], [0, 1, 0, 0], [0, 0, \cos(\theta)^2 I - I\sin(\theta)^2, \quad \textbf{(1.10)}$$

$$2\,I\cos(\theta)\,\sin(\theta)\,],\,[0,\,0,\,2\,I\cos(\theta)\,\sin(\theta),\,-I\cos(\theta)^2+\sin(\theta)^2\,I]]\,)$$

controlled-HWP, control = qubit 1, logical 0, target qubit 2

```
> ZCHWP:=theta->Matrix([[cos(theta)^2*I-sin(theta)^2*I,2*I*cos
  (theta)*sin(theta), 0, 0],[2*I*cos(theta)*sin(theta),-cos
  (theta)^2*I+sin(theta)^2*I, 0, 0], [0,0,1,0],[0,0,0,1]]);
```

$$ZCHWP := \theta \rightarrow Matrix\left(\left[\left[\cos(\theta)^2\,I-I\sin(\theta)^2,\,2\,I\cos(\theta)\,\sin(\theta),\,0,\,0\right],\,\left[2\,I\cos(\theta)\,\sin(\theta),\,-I\cos(\theta)^2+\sin(\theta)^2\,I,\,0,\,0\right],\,[0,\,0,\,1,\,0],\,[0,\,0,\,0,\,1]\right]\right) \quad (1.11)$$

controlled-HWP, control = qubit 2, logical 1, target qubit 1

```
> NCHWP:=theta->Matrix([[1,0,0,0],[0,cos(theta)^2*I-sin(theta)
  ^2*I,0,2*I*cos(theta)*sin(theta)],[0,0,1,0],[0,2*I*cos(theta)*
  sin(theta), 0, -cos(theta)^2*I+sin(theta)^2*I]]);
```

$$NCHWP := \theta \rightarrow Matrix\left(\left[[1,\,0,\,0,\,0],\,\left[0,\,\cos(\theta)^2\,I-I\sin(\theta)^2,\,0,\,2\,I\cos(\theta)\,\sin(\theta)\right],\,[0,\,0,\,1,\,0],\,\left[0,\,2\,I\cos(\theta)\,\sin(\theta),\,0,\,-I\cos(\theta)^2+\sin(\theta)^2\,I\right]\right]\right) \quad (1.12)$$

controlled-HWP, control = qubit 2, logical 0, target qubit 1

```
> NZCHWP:=theta->Matrix([[cos(theta)^2*I-sin(theta)^2*I,0,2*I*
  cos(theta)*sin(theta),0],[0,1,0,0],[2*I*cos(theta)*sin(theta),
  0,-cos(theta)^2*I+sin(theta)^2*I,0],[0,0,0,1]]);
```

$$NZCHWP := \theta \rightarrow Matrix\left(\left[\left[\cos(\theta)^2\,I-I\sin(\theta)^2,\,0,\,2\,I\cos(\theta)\,\sin(\theta),\,0\right],\,[0,\,1,\,0,\,0],\,\left[2\,I\cos(\theta)\,\sin(\theta),\,0,\,-I\cos(\theta)^2+\sin(\theta)^2\,I,\,0\right],\,[0,\,0,\,0,\,1]\right]\right) \quad (1.13)$$

Theoretical

BS:

```
> A:=(a, b)->Kron(Id, BS(a, b));
```

$$A := (a,\,b) \rightarrow Kron(Id,\,BS(a,\,b)) \quad (2.1)$$

```
> BSBS:=Kron(A(1/sqrt(2)*exp(I*phi1), 1/sqrt(2)),A(1/sqrt(2)*exp
  (I*phi2), 1/sqrt(2)));
```

The input is $\alphe_{1}\vert HtHt \rangle + \beta_{1} \vert VtVt \rangle$

```
> input:=Vector([alpha1,0,0,0,0,0,0,0,0,0,beta1,0,0,0,0,0]);
> HermitianTranspose(input).input;
```

$$\alpha 1\,\overline{\alpha 1}+\beta 1\,\overline{\beta 1} \quad (2.2)$$

CHWP: target is qubit 3, control: qubit 4, logical 0 (HWP at 22.5 at the transmitted arm)

```
> HWP1:=Kron(Id,Kron(Id, evalf(NZCHWP(22.5*Pi/180))));
```

CHWP: target is qubit 3, control: qubit 4, logical 1 (HWP at -22.5 at the reflected arm)

```
> HWP2:=Kron(Id, Kron(Id, evalf(NCHWP(-(22.5)*Pi/180)))) ;
```

CHWP: Target is qubit 1, control: qubit 2, logical 1 (HWP at horizontal to apply the controlled-Z)

```
> HWP3:=Kron(Kron(evalf(NCHWP(Pi/2)), Id), Id);
```

Graph Preperation:

```
> GP:=HWP3.HWP2.HWP1.BSBS;
> graph:=GP.input;
> evalf(HermitianTranspose(graph).graph);
```

$$(0.2500000001+0.\,I)\,e^{1.\,I\phi 1}\,e^{1.\,I\phi 2}\,\beta 1\,\overline{e^{1.\,I\phi 1}\,e^{1.\,I\phi 2}\,\beta 1}+(0.2500000001+0.\,I)\,e^{1.\,I\phi 1}\,\alpha 1 \quad (2.3)$$

$$\overline{e^{1.I\phi 1}}\,\alpha 1 + (0.2500000001 + 0.I)\,e^{1.I\phi 1}\,e^{1.I\phi 2}\,\alpha 1\,\overline{e^{1.I\phi 1}\,e^{1.I\phi 2}}\,\alpha 1 + (0.2500000001 + 0.I)\,e^{1.I\phi 2}\,\alpha 1\,\overline{e^{1.I\phi 2}\,\alpha 1} + (0.2500000001 + 0.I)\,\alpha 1\,\overline{\alpha 1} + (0.2500000001 + 0.I)\,e^{1.I\phi 1}\,\beta 1\,\overline{e^{1.I\phi 1}\,\beta 1} + (0.2500000001 + 0.I)\,e^{1.I\phi 2}\,\beta 1\,\overline{e^{1.I\phi 2}\,\beta 1} + (0.2500000001 + 0.I)\,\beta 1\,\overline{\beta 1}$$

```
> for i from 1 to 16 do
  evalf(graph[i]);
  od;
```

$$(0. + 0.3535533906\,I)\,e^{1.I\phi 1}\,e^{1.I\phi 2}\,\alpha 1 \tag{2.4}$$
$$(0. + 0.3535533906\,I)\,e^{1.I\phi 1}\,\alpha 1$$
$$(0. + 0.3535533907\,I)\,e^{1.I\phi 1}\,e^{1.I\phi 2}\,\alpha 1$$
$$(0. - 0.3535533907\,I)\,e^{1.I\phi 1}\,\alpha 1$$
$$(0.3535533906 + 0.I)\,e^{1.I\phi 2}\,\alpha 1$$
$$(0.3535533906 + 0.I)\,\alpha 1$$
$$(0.3535533907 + 0.I)\,e^{1.I\phi 2}\,\alpha 1$$
$$(-0.3535533907 + 0.I)\,\alpha 1$$
$$(0. + 0.3535533907\,I)\,e^{1.I\phi 1}\,e^{1.I\phi 2}\,\beta 1$$
$$(0. - 0.3535533907\,I)\,e^{1.I\phi 1}\,\beta 1$$
$$(0. - 0.3535533906\,I)\,e^{1.I\phi 1}\,e^{1.I\phi 2}\,\beta 1$$
$$(0. - 0.3535533906\,I)\,e^{1.I\phi 1}\,\beta 1$$
$$(-0.3535533907 + 0.I)\,e^{1.I\phi 2}\,\beta 1$$
$$(0.3535533907 + 0.I)\,\beta 1$$
$$(0.3535533906 + 0.I)\,e^{1.I\phi 2}\,\beta 1$$
$$(0.3535533906 + 0.I)\,\beta 1$$

Maximizing interferometers on D:

```
> phi1:=3*Pi/2;phi2:=0;
```

$$\phi 1 := \frac{3\,\pi}{2} \tag{2.5}$$
$$\phi 2 := 0$$

```
> for i from 1 to 16 do
  evalf(graph[i]);
  od;
```

$$(0.3535533906 - 0.I)\,\alpha 1 \tag{2.6}$$
$$(0.3535533906 - 0.I)\,\alpha 1$$
$$(0.3535533907 - 0.I)\,\alpha 1$$
$$(-0.3535533907 - 0.I)\,\alpha 1$$
$$(0.3535533906 + 0.I)\,\alpha 1$$
$$(0.3535533906 + 0.I)\,\alpha 1$$
$$(0.3535533907 + 0.I)\,\alpha 1$$
$$(-0.3535533907 + 0.I)\,\alpha 1$$
$$(0.3535533907 - 0.I)\,\beta 1$$

$(-0.3535533907 - 0.\,\mathrm{I})\ \beta 1$
$(-0.3535533906 - 0.\,\mathrm{I})\ \beta 1$
$(-0.3535533906 - 0.\,\mathrm{I})\ \beta 1$
$(-0.3535533907 + 0.\,\mathrm{I})\ \beta 1$
$(0.3535533907 + 0.\,\mathrm{I})\ \beta 1$
$(0.3535533906 + 0.\,\mathrm{I})\ \beta 1$
$(0.3535533906 + 0.\,\mathrm{I})\ \beta 1$

Graph Density Matrix:

```
> CD:=graph.HermitianTranspose(graph);
```

General formulea for measurment rotations:

Outcome of measuring in HH: M= H tensor Id tensor H tensor Id

```
> H:=Matrix([[1, 0], [0,0]]);
```

$$H := \begin{bmatrix} 1 & 0 \\ 0 & 0 \end{bmatrix} \tag{3.1}$$

```
> MHH:=Kron(H, Kron(Id, Kron(H, Id)));
> Hadamard := 1/sqrt(2)* Matrix([[1, 1], [1, -1]]);
```

$$Hadamard := \begin{bmatrix} \frac{\sqrt{2}}{2} & \frac{\sqrt{2}}{2} \\ \frac{\sqrt{2}}{2} & -\frac{\sqrt{2}}{2} \end{bmatrix} \tag{3.2}$$

```
> Ret := theta -> Matrix([[1, 0], [0, exp(I*theta)]]);
```

$$Ret := \theta \rightarrow Matrix(\left[[1, 0], [0, e^{\theta \mathrm{I}}]\right]) \tag{3.3}$$

```
> J := theta->Hadamard.Ret(theta);
```

$$J := \theta \rightarrow Hadamard.Ret(\theta) \tag{3.4}$$

```
> Jtheta1Jtheta2:=(theta1, theta2)->Kron(J(theta1), Kron(Id,
  Kron(J(theta2), Id)));
```

$$Jtheta1Jtheta2 := (\theta 1, \theta 2) \rightarrow Kron(J(\theta 1), Kron(Id, Kron(J(\theta 2), Id))) \tag{3.5}$$

```
> JJHC:=2*MHH.Jtheta1Jtheta2(theta1, theta2).graph;
> Result:=evalf(simplify(evalm(JJHC)));
```

$$\begin{aligned} Result := [&0.3535533906\ \alpha 1 - 0.3535533906\ \beta 1\ e^{1.\mathrm{I}(\theta 1 + \theta 2)} + 0.3535533907\ e^{1.\mathrm{I}\theta 2}\ \alpha 1 \\ &+ 0.3535533907\ e^{1.\mathrm{I}\theta 1}\ \beta 1, 0.3535533906\ \alpha 1 - 0.3535533906\ \beta 1\ e^{1.\mathrm{I}(\theta 1 + \theta 2)} \\ &- 0.3535533907\ e^{1.\mathrm{I}\theta 2}\ \alpha 1 - 0.3535533907\ e^{1.\mathrm{I}\theta 1}\ \beta 1, 0., 0., 0.3535533906\ \alpha 1 \\ &+ 0.3535533906\ \beta 1\ e^{1.\mathrm{I}(\theta 1 + \theta 2)} + 0.3535533907\ e^{1.\mathrm{I}\theta 2}\ \alpha 1 - 0.3535533907\ e^{1.\mathrm{I}\theta 1}\ \beta 1, \\ &0.3535533906\ \alpha 1 + 0.3535533906\ \beta 1\ e^{1.\mathrm{I}(\theta 1 + \theta 2)} - 0.3535533907\ e^{1.\mathrm{I}\theta 2}\ \alpha 1 \\ &+ 0.3535533907\ e^{1.\mathrm{I}\theta 1}\ \beta 1, 0., 0., 0., 0., 0., 0., 0., 0., 0.] \end{aligned} \tag{3.6}$$

The output or the state of path qubits for each tomography setting on the polarization qubits
To compare the results of the simulation with the experiment, we use the same input in the simulation

as the experiment, which is the state |+>. So we set v11 and v21 accordingly:

```
> alpha1:=1/sqrt(2);beta1:=1/sqrt(2);
```

$$\alpha 1 := \frac{\sqrt{2}}{2} \qquad \textbf{(4.1)}$$

$$\beta 1 := \frac{\sqrt{2}}{2}$$

Measurement bases

Rotation that takes H to H

```
> RHH:= HWP(0*Pi/180).QWP(0*Pi/180):
```

Rotation that takes V to H

```
> RVH:= HWP(45*Pi/180).QWP(0*Pi/180):
```

Rotation that takes D to H:

```
> RDH:= HWP(22.5*Pi/180).QWP(45*Pi/180):
```

Rotation that takes A to H:

```
> RAH:= HWP(67.5*Pi/180).QWP(45*Pi/180):
```

Rotation that takes L to H:

```
> RLH:= HWP(67.5*Pi/180).QWP(0*Pi/180):
```

Rotation that takes R to H

```
> RRH:= HWP(22.5*Pi/180).QWP(0*Pi/180):
```

Measurement result of perfect Graph, B1 =H, B2 = H

```
> HH16:= Kron(RHH, Kron(Id, Kron(RHH, Id))):
> HHCD:=MHH.HH16.CD.HermitianTranspose(HH16).
  HermitianTranspose(MHH)/(Trace(HermitianTranspose(MHH).
  HermitianTranspose(HH16).CD.HH16.MHH));
> evalm(evalf(HHCD));
```

Measurement result of perfect Graph, B1 =V, B2 = H

```
> VH16:= Kron(RVH, Kron(Id, Kron(RHH, Id)));
> VHCD:=MHH.VH16.CD.HermitianTranspose(VH16).
  HermitianTranspose(MHH)/(Trace(HermitianTranspose(MHH).
  HermitianTranspose(VH16).CD.VH16.MHH));
> evalm(evalf(VHCD));
```

Measurement result of perfect Graph, B1 =H, B2 = V

```
> HV16 := Kron(RHH, Kron(Id, Kron(RVH, Id)));
> HVCD:=MHH.HV16.CD.HermitianTranspose(HV16).
  HermitianTranspose(MHH)/evalf(Trace(HermitianTranspose
  (MHH).MHH.HV16.CD.HermitianTranspose(HV16)));
> evalm(evalf(HVCD));
```

Measurement result of perfect Graph, B1 =V, B2 = V

```
> VV16 := Kron(RVH, Kron(Id, Kron(RVH, Id)));
```

```
> VVCD:=MHH.VV16.CD.HermitianTranspose(VV16).
  HermitianTranspose(MHH)/evalf(Trace(HermitianTranspose
  (MHH).MHH.VV16.CD.HermitianTranspose(VV16)));
> evalm(evalf(VVCD));
```

Measurement result of perfect Graph, B1 =R, B2 = V

```
> RV16 :=  Kron(RRH, Kron(Id, Kron(RVH, Id)));
> RVCD:=MHH.RV16.CD.HermitianTranspose(RV16).
  HermitianTranspose(MHH)/evalf(Trace(HermitianTranspose
  (MHH).MHH.RV16.CD.HermitianTranspose(RV16)));
> evalm(evalf(RVCD));
```

Measurement result of perfect Graph, B1 =R, B2 = H

```
> RH16 := Kron(RRH, Kron(Id, Kron(RHH, Id)));
> RHCD:=MHH.RH16.CD.HermitianTranspose(RH16).
  HermitianTranspose(MHH)/(Trace(HermitianTranspose(MHH).
  MHH.RH16.CD.HermitianTranspose(RH16)));
> evalm(evalf(RHCD));
```

Measurement result of perfect Graph, B1 =D, B2 = V

```
> DV16 := Kron(RDH, Kron(Id, Kron(RVH, Id)));
> DVCD:=MHH.DV16.CD.HermitianTranspose(DV16).
  HermitianTranspose(MHH)/evalf(Trace(HermitianTranspose
  (MHH).MHH.DV16.CD.HermitianTranspose(DV16)));
> evalm(evalf(DVCD));
```

Measurement result of perfect Graph, B1 =D, B2 = H

```
> DH16 := Kron(RDH, Kron(Id, Kron(RHH, Id)));
> DHCD:=MHH.DH16.CD.HermitianTranspose(DH16).
  HermitianTranspose(MHH)/evalf(Trace(HermitianTranspose
  (MHH).MHH.DH16.CD.HermitianTranspose(DH16)));
> evalm(evalf(DHCD));
```

Measurement result of perfect Graph, B1 =D, B2 = R

```
> DR16 :=  Kron(RDH, Kron(Id, Kron(RRH, Id)));
> DRCD:=MHH.DR16.CD.HermitianTranspose(DR16).
  HermitianTranspose(MHH)/evalf(Trace(MHH.DR16.CD.
  HermitianTranspose(DR16).HermitianTranspose(MHH)));
> evalm(evalf(DRCD));
```

Measurement result of perfect Graph, B1 =R, B2 = R

```
> RR16 := Kron(RRH, Kron(Id, Kron(RRH, Id)));
> RRCD:=MHH.RR16.CD.HermitianTranspose(RR16).
  HermitianTranspose(MHH)/evalf(Trace(HermitianTranspose
  (MHH).MHH.RR16.CD.HermitianTranspose(RR16)));
```

```
> evalm(evalf(RRCD));
```

Measurement result of perfect Graph, B1 =R, B2 = D

```
> RD16 := Kron(RRH, Kron(Id, Kron(RDH, Id)));
> RDCD:=MHH.RD16.CD.HermitianTranspose(RD16).
  HermitianTranspose(MHH)/evalf(Trace(HermitianTranspose
  (MHH).MHH.RD16.CD.HermitianTranspose(RD16)));
> evalm(evalf(RDCD));
```

Measurement result of perfect Graph, B1 =H, B2 = D

```
> HD16 := Kron(RHH, Kron(Id, Kron(RDH, Id)));
> HDCD:=MHH.HD16.CD.HermitianTranspose(HD16).
  HermitianTranspose(MHH)/evalf(Trace(HermitianTranspose
  (MHH).MHH.HD16.CD.HermitianTranspose(HD16)));
> evalm(evalf(HDCD));
```

Measurement result of perfect Graph, B1 =V, B2 = D

```
> VD16 := Kron(RVH, Kron(Id, Kron(RDH, Id)));
> VDCD:=MHH.VD16.CD.HermitianTranspose(VD16).
  HermitianTranspose(MHH)/evalf(Trace(HermitianTranspose
  (MHH).MHH.VD16.CD.HermitianTranspose(VD16)));
> evalm(evalf(VDCD));
```

Measurement result of perfect Graph, B1 =V, B2 = L

```
> VL16 := Kron(RVH, Kron(Id, Kron(RLH, Id)));
> VLCD:=(MHH.VL16.CD.HermitianTranspose(VL16).
  HermitianTranspose(MHH))/evalf(Trace(MHH.VL16.CD.
  HermitianTranspose(VL16).HermitianTranspose(MHH)));
> evalm(evalf(VLCD));
```

Measurement result of perfect Graph, B1 =H, B2 = L

```
> HL16 := Kron(RHH, Kron(Id, Kron(RLH, Id)));
> HLCD:=MHH.HL16.CD.HermitianTranspose(HL16).
  HermitianTranspose(MHH)/evalf(Trace(HermitianTranspose
  (MHH).MHH.HL16.CD.HermitianTranspose(HL16)));
> evalm(evalf(HLCD));
```

Measurement result of perfect Graph, B1 =R, B2 = L

```
> RL16 := Kron(RRH, Kron(Id, Kron(RLH, Id)));
> RLCD:=MHH.RL16.CD.HermitianTranspose(RL16).
  HermitianTranspose(MHH)/(Trace(HermitianTranspose(MHH).
  MHH.RL16.CD.HermitianTranspose(RL16)));
> evalm(evalf(RLCD));
```

Measurement result of perfect Graph, w01 =0, w02 = Pi/2 = RRH

```
> HR16:= Kron(HWP(22.5*Pi/180), Kron(Id, Kron(RRH, Id)));
```

```
> HRCD:=MHH.HR16.CD.HermitianTranspose(HR16).
  HermitianTranspose(MHH)/evalf(Trace(HermitianTranspose
  (MHH).MHH.HR16.CD.HermitianTranspose(HR16)));
> evalm(evalf(HRCD));
```

Measurement result of perfect Graph, w01=0, w02 = 0

```
> HH16:= Kron(HWP(22.5*Pi/180), Kron(Id, Kron(HWP(22.5*
  Pi/180), Id)));
> HHCD:=MHH.HH16.CD.HermitianTranspose(HH16).MHH/(Trace
  (MHH.HH16.CD.HermitianTranspose(HH16).MHH):
> evalm(evalf(HHCD));
```

Appendix D

Simulation of the Effect of Errors in Wave Plates in Created Graph

In this appendix I study the effect of errors of the waveplate angles, retardances and phase of interferometer on state creation.

```
> restart:
```

Tensor Product

```
> with(LinearAlgebra):
> Kron:=proc(A::Matrix,B::Matrix)
  local M,P,i,j;
  M:=Matrix(RowDimension(A)*RowDimension(B),ColumnDimension(A)*
  ColumnDimension(B)):
  P:=Matrix(RowDimension(B),ColumnDimension(B)):
  for i to RowDimension(A) do
  for j to ColumnDimension(A) do
  P:=ScalarMultiply(B,A[i,j]):
  M[1+(i-1)*RowDimension(B)..(i-1)*RowDimension(B)+RowDimension
  (B),1+(j-1)*ColumnDimension(B)..(j-1)*ColumnDimension(B)+
  ColumnDimension(B)]:=P:
  od
  od:
  M;
  end proc:
```

Operator Definitions

transmitted path = > logical zero, then BS matrix should be defined as is.

```
> BS:=eta->Matrix([[exp(I*eta)*1/sqrt(2),1/sqrt(2)],[1/sqrt(2),
  -exp(I*eta)/sqrt(2)]]);
```

$$BS := \eta \to Matrix\left(\left[\left[\frac{e^{I\eta}}{\sqrt{2}}, \frac{1}{\sqrt{2}}\right], \left[\frac{1}{\sqrt{2}}, -\frac{e^{I\eta}}{\sqrt{2}}\right]\right]\right) \quad \textbf{(2.1)}$$

```
> Id:=Matrix([[1,0],[0,1]]);
```

$$Id := \begin{bmatrix} 1 & 0 \\ 0 & 1 \end{bmatrix} \quad \textbf{(2.2)}$$

General waveplate, including retardance:

```
> GWP:=(theta, phi)->Matrix([[cos(theta)^2 + exp(I*phi)* sin
  (theta)^2, (1-exp(I*phi))*sin(theta)*cos(theta)], [(1-exp(I*
  phi))*sin(theta)*cos(theta),  exp(I*phi)*cos(theta)^2 + sin
  (theta)^2]]);
```

$$GWP := (\theta, \phi) \to Matrix\left(\left[\left[\cos(\theta)^2 + e^{I\phi}\sin(\theta)^2, \left(1 - e^{I\phi}\right)\sin(\theta)\cos(\theta)\right], \left[\left(1 - e^{I\phi}\right)\sin(\theta)\cos(\theta), e^{I\phi}\cos(\theta)^2 + \sin(\theta)^2\right]\right]\right) \quad \textbf{(2.3)}$$

controlled-GWP, control = qubit 1, logical 1, target qubit 2.

```
> CGWP:=(theta, phi)->Matrix([[1,0,0,0],[0,1,0,0],[0,0,I*(cos
```

```
(theta)^2 + exp(I*phi)* sin(theta)^2),I*(1-exp(I*phi))*sin
(theta)*cos(theta)],[0,0,I*(1-exp(I*phi))*sin(theta)*cos
(theta),I*(exp(I*phi)*cos(theta)^2 + sin(theta)^2)]]);
```

$$CGWP := (\theta, \phi) \rightarrow Matrix\left(\left[[1, 0, 0, 0], [0, 1, 0, 0], \left[0, 0, I\left(\cos(\theta)^2 + e^{I\phi}\sin(\theta)^2\right), I\left(1 - e^{I\phi}\right)\sin(\theta)\cos(\theta)\right], \left[0, 0, I\left(1 - e^{I\phi}\right)\sin(\theta)\cos(\theta), I\left(e^{I\phi}\cos(\theta)^2 + \sin(\theta)^2\right)\right]\right]\right) \quad (2.4)$$

controlled-GWP, control = qubit 1, logical 0, target qubit 2

```
> ZCGWP:=(theta, phi)->Matrix([[I*(cos(theta)^2 + exp(I*phi)*
sin(theta)^2),I*(1-exp(I*phi))*sin(theta)*cos(theta), 0, 0],
[I*(1-exp(I*phi))*sin(theta)*cos(theta),I*(exp(I*phi)*cos
(theta)^2 + sin(theta)^2), 0, 0], [0,0,1,0],[0,0,0,1]]);
```

$$ZCGWP := (\theta, \phi) \rightarrow Matrix\left(\left[\left[I\left(\cos(\theta)^2 + e^{I\phi}\sin(\theta)^2\right), I\left(1 - e^{I\phi}\right)\sin(\theta)\cos(\theta), 0, 0\right], \left[I\left(1 - e^{I\phi}\right)\sin(\theta)\cos(\theta), I\left(e^{I\phi}\cos(\theta)^2 + \sin(\theta)^2\right), 0, 0\right], [0, 0, 1, 0], [0, 0, 0, 1]\right]\right) \quad (2.5)$$

controlled-HWP, control = qubit 2, logical 1, target qubit 1

```
> NCGWP:=(theta, phi)->Matrix([[1,0,0,0],[0,I*(cos(theta)^2 +
exp(I*phi)* sin(theta)^2),0,I*(1-exp(I*phi))*sin(theta)*cos
(theta)],[0,0,1,0],[0,I*(1-exp(I*phi))*sin(theta)*cos(theta),
0, I*(exp(I*phi)*cos(theta)^2 + sin(theta)^2)]]);
```

$$NCGWP := (\theta, \phi) \rightarrow Matrix\left(\left[[1, 0, 0, 0], \left[0, I\left(\cos(\theta)^2 + e^{I\phi}\sin(\theta)^2\right), 0, I\left(1 - e^{I\phi}\right)\sin(\theta)\cos(\theta)\right], [0, 0, 1, 0], \left[0, I\left(1 - e^{I\phi}\right)\sin(\theta)\cos(\theta), 0, I\left(e^{I\phi}\cos(\theta)^2 + \sin(\theta)^2\right)\right]\right]\right) \quad (2.6)$$

controlled-HWP, control = qubit 2, logical 0, target qubit 1

```
> NZCGWP:=(theta, phi)->Matrix([[I*(cos(theta)^2 + exp(I*phi)*
sin(theta)^2),0,I*(1-exp(I*phi))*sin(theta)*cos(theta),0],[0,
1,0,0],[I*(1-exp(I*phi))*sin(theta)*cos(theta),0,I*(exp(I*phi)
*cos(theta)^2 + sin(theta)^2),0],[0,0,0,1]]);
```

$$NZCGWP := (\theta, \phi) \rightarrow Matrix\left(\left[\left[I\left(\cos(\theta)^2 + e^{I\phi}\sin(\theta)^2\right), 0, I\left(1 - e^{I\phi}\right)\sin(\theta)\cos(\theta), 0\right], [0, 1, 0, 0], \left[I\left(1 - e^{I\phi}\right)\sin(\theta)\cos(\theta), 0, I\left(e^{I\phi}\cos(\theta)^2 + \sin(\theta)^2\right), 0\right], [0, 0, 0, 1]\right]\right) \quad (2.7)$$

Theoretical

BS:

```
> A:=eta->Kron(Id, BS(eta));
```

$$A := \eta \rightarrow Kron(Id, BS(\eta)) \quad (3.1)$$

```
> BSBS:=(eta1, eta2) -> Kron(A(eta1), A(eta2));
```

$$BSBS := (\eta 1, \eta 2) \rightarrow Kron(A(\eta 1), A(\eta 2)) \quad (3.2)$$

The input is (|HtHt> + |VtVt>)/sqrt(2):

```
> input:=1/sqrt(2)*Vector([1,0,0,0,0,0,0,0,0,0,1,0,0,0,0,0]);
```

$$input := \begin{bmatrix} 1 .. 16\ Vector_{column} \\ Data\ Type: anything \\ Storage: rectangular \\ Order: Fortran\_order \end{bmatrix} \tag{3.3}$$

```
> HermitianTranspose(input).input;
```

$$1 \tag{3.4}$$

CHWP: target is qubit 3, control: qubit 4, logical 0 (HWP at 22.5 at the transmitted arm)

```
> HWP1:=(theta1, phi1)-> Kron(Id,Kron(Id, evalf(NZCGWP((22.5+
  theta1)*Pi/180, Pi*(1+phi1)))));
```

$$HWP1 := (\theta 1, \phi 1) \rightarrow Kron\left(Id, Kron\left(Id, evalf\left(NZCGWP\left(\frac{1}{180}\ (22.5 + \theta 1)\ \pi, \pi\ (1 + \phi 1)\right)\right)\right)\right) \tag{3.5}$$

CHWP: target is qubit 3, control: qubit 4, logical 1 (HWP at -22.5 at the reflected arm)

```
> HWP2:=(theta2, phi2)-> Kron(Id, Kron(Id, evalf(NCGWP((-22.5+
  theta2)*Pi/180, Pi*(1+phi2)))));
```

$$HWP2 := (\theta 2, \phi 2) \rightarrow Kron\left(Id, Kron\left(Id, evalf\left(NCGWP\left(\frac{1}{180}\ (-22.5 + \theta 2)\ \pi, \pi\ (1 + \phi 2)\right)\right)\right)\right) \tag{3.6}$$

CHWP: Target is qubit 1, control: qubit 2, logical 1 (HWP at horizontal to apply the controlled-Z)

```
> HWP3:=(theta3, phi3)-> Kron(Kron(NCGWP((90+theta3)*Pi/180, Pi*
  (1+phi3)), Id), Id);
```

$$HWP3 := (\theta 3, \phi 3) \rightarrow Kron\left(Kron\left(NCGWP\left(\frac{1}{180}\ (90 + \theta 3)\ \pi, \pi\ (1 + \phi 3)\right), Id\right), Id\right) \tag{3.7}$$

```
> GP := (θ1, θ2, θ3, ϕ1, ϕ2, ϕ3, η1, η2) →HWP3(θ3, ϕ3).HWP2(θ2, ϕ2).HWP1(θ1, ϕ1)
      .BSBS(3·π/2 ·(1 + η1), η2);
```

$$GP := (\theta 1, \theta 2, \theta 3, \phi 1, \phi 2, \phi 3, \eta 1, \eta 2) \rightarrow Typesetting{:}\text{-}delayDotProduct\left(Typesetting{:}\text{-}delayDotProduct\left(Typesetting{:}\text{-}delayDotProduct\left(HWP3(\theta 3, \phi 3), HWP2(\theta 2, \phi 2)\right), HWP1(\theta 1, \phi 1)\right), BSBS\left(\frac{3}{2}\ \pi\ (1 + \eta 1), \eta 2\right)\right) \tag{3.8}$$

```
> PGraph := 1/4 Vector([1, 1, 1, -1, 1, 1, 1,-1, 1, -1, -1, -1, -1, 1, 1, 1]);
```

$$PGraph := \begin{bmatrix} 1 .. 16\ Vector_{column} \\ Data\ Type: anything \\ Storage: rectangular \\ Order: Fortran\_order \end{bmatrix} \tag{3.9}$$

Graph Density Matrix:

```
> CDPerfect:=PGraph.HermitianTranspose(PGraph);
```

$$CDPerfect := \begin{bmatrix} 16 \text{ x } 16 \text{ Matrix} \\ \text{Data Type: anything} \\ \text{Storage: rectangular} \\ \text{Order: Fortran\_order} \end{bmatrix} \quad \textbf{(3.10)}$$

Studying the effect of error of up to 4 degrees in setting of each waveplate:

```
> for θ1 from -2 by 2 to 2 do;
  for θ2 from -2 by 2 to 2 do;
  for θ3 from -2 by 2 to 2 do;
  graph := GP(θ1, θ2, θ3, 0, 0, 0, 0, 0).input;
 CD := graph.HermitianTranspose(graph) :
 M := CDPerfect.CD :
 Fidelity := evalf(Trace(M));
 Purity := evalf(HermitianTranspose(graph).graph);
  print(θ1); print(θ2); print(θ3);
 print(ℜ(Fidelity));
  print(Purity);
  od;od;od;
```

Effect of error in retardance of WPs in state creation:

```
> for ϕ1 from -0.02 by 0.02 to 0.02 do;
 for ϕ2 from -0.02 by 0.02 to 0.02 do;
 for ϕ3 from -0.02 by 0.02 to 0.02 do;

  graph := GP(0, 0, 0, ϕ1, ϕ2, ϕ3, 0, 0).input;
 CD := graph.HermitianTranspose(graph) :
 M := CDPerfect.CD :
 Fidelity := evalf(Trace(M));
  Purity := evalf(HermitianTranspose(graph).graph);
 print(ϕ1); print(ϕ2); print(ϕ3);
 print(ℜ(Fidelity));
  print(Purity);
  od;od;od;
```

Effect of error in retardance of WPs in state creation:

```
> for η1 from -0.1 by 0.1 to 0.1 do;
 for η2 from -0.1 by 0.1 to 0.1 do;
 graph := GP(0, 0, 0, 0, 0,  0, η1, η2).input;
 CD := graph.HermitianTranspose(graph) :
 M := CDPerfect.CD :
 Fidelity := evalf(Trace(M));
  Purity := evalf(HermitianTranspose(graph).graph);
 print(η1); print(η2);
 print(ℜ(Fidelity));
  print(Purity);
  od;od;
```

```
> for theta1 from -1 by 1 to 1 do;
  for theta2 from -1 by 1 to 1 do;
  for theta3 from -1 by 1 to 1 do;
  for phi1 from -0.02 by 0.02 to 0.02 do;
  for phi2 from -0.02 by 0.02 to 0.02 do;
  for phi3 from -0.02 by 0.02 to 0.02 do;
  for eta1 from -0.1 by 0.1 to 0.1 do;
  for eta2 from -0.1 by 0.1 to 0.1 do;
  graph:=GP(theta1, theta2, theta3, phi1, phi2, phi3, eta1,
  eta2).input;
  CD:=graph.HermitianTranspose(graph):
  M:=CDPerfect.CD:
  Fidelity:=evalf(Trace(M));
  print(theta1);print(theta2);print(theta3);print(phi1);print
  (phi2);print(phi3);print(eta1);print(eta2);
  print(Fidelity);
  od;od;od;od;od;od;od;od;
```

Appendix E

Simulation of Loop Graph with Realistic Polarization Entangled Photons, Unbalanced Interferometric Loss and Imperfect Interferometric Visibility

This appendix includes the simulation of the graph production and measurement. The input to the graph state setup in this simulation is the output of the source in the experiment, the interferometers have different losses in each arm and the effect of visibilities being 93% to 95% is taken into account.

```
> restart:
```

Tensor Product

Operator Definitions

transmitted path = > logical zero, then BS matrix should be defined as is. HWP and QWP are defined so that their fast axis is at vertical.

```
> zero:=Matrix([[1],[0]]);
> one:=Matrix([[0],[1]]);
> BS:=(alpha2, beta2)-> Matrix([[alpha2,beta2],[beta2,-alpha2]])
  ;
```

$$BS := (\alpha 2, \beta 2) \rightarrow \mathrm{Matrix}([[\alpha 2, \beta 2], [\beta 2, -\alpha 2]]) \quad \textbf{(2.1)}$$

```
> Id:=Matrix([[1,0],[0,1]]);
> HWP0:=Matrix([[I,0],[0,-I]]); #fast axis is at horizontal
> QWP0:=exp(I*Pi/4)*Matrix([[1,0],[0,-I]]);
> R:=theta->Matrix([[cos(theta),sin(theta)],[-sin(theta),cos
  (theta)]]);
> HWP:=theta->R(-theta).HWP0.R(theta);
> QWP:=theta->R(-theta).QWP0.R(theta);
```

controlled-HWP, control = qubit 1, logical 1, target qubit 2.

```
> CHWP:=theta->Matrix([[1,0,0,0],[0,1,0,0],[0,0,cos(theta)^2*I-
  sin(theta)^2*I,2*I*cos(theta)*sin(theta)],[0,0,2*I*cos(theta)*
  sin(theta),-cos(theta)^2*I+sin(theta)^2*I]]);
```

controlled-HWP, control = qubit 1, logical 0, target qubit 2

```
> ZCHWP:=theta->Matrix([[cos(theta)^2*I-sin(theta)^2*I,2*I*cos
  (theta)*sin(theta), 0, 0],[2*I*cos(theta)*sin(theta),-cos
  (theta)^2*I+sin(theta)^2*I, 0, 0], [0,0,1,0],[0,0,0,1]]);
```

controlled-HWP, control = qubit 2, logical 1, target qubit 1

```
> NCHWP:=theta->Matrix([[1,0,0,0],[0,cos(theta)^2*I-sin(theta)
  ^2*I,0,2*I*cos(theta)*sin(theta)],[0,0,1,0],[0,2*I*cos(theta)*
  sin(theta), 0, -cos(theta)^2*I+sin(theta)^2*I]]);
```

controlled-HWP, control = qubit 2, logical 0, target qubit 1

```
> NZCHWP:=theta->Matrix([[cos(theta)^2*I-sin(theta)^2*I,0,2*I*
  cos(theta)*sin(theta),0],[0,1,0,0],[2*I*cos(theta)*sin(theta),
  0,-cos(theta)^2*I+sin(theta)^2*I,0],[0,0,0,1]]);
```

Theoretical

BS:

Interferometer B:

```
> TB:=evalf(163/(192+163));
```

$$TB := 0.4591549296 \quad \textbf{(3.1)}$$

```
> RB:=evalf(192/(192+163));
```

$$RB := 0.5408450704 \quad \textbf{(3.2)}$$

Interferometer A:

```
> TA:=evalf(146/(146+220));
```

$$TA := 0.3989071038 \quad \textbf{(3.3)}$$

```
> RA:=evalf(220/(146+220));
```

$$RA := 0.6010928962 \quad \textbf{(3.4)}$$

```
> A:=(a, b)->Kron(Id, BS(a, b));
> BSBS:=Kron(A(sqrt(TA)*exp(I*(3*Pi/2)), sqrt(RA)),A(sqrt(TB)*
  exp(I*0), sqrt(RB)));
```

The perfect input is (|HtHt>+ |VtVt>)/sqrt(2):

```
> input:=1/sqrt(2)*Vector([1,0,0,0,0,0,0,0,0,0,1,0,0,0,0,0]);
> HermitianTranspose(input).input;
> CD:=input.HermitianTranspose(input);
```

The density matrix of the polarization state of the two photons after single mode fibers:

```
> DMX:=Matrix([[0.5393,0, -0.0235 + 0.0229*I, 0,0,0,0,0,
  -0.0458 - 0.0361*I, 0, 0.3919 - 0.1710*I, 0, 0, 0, 0, 0],
  [0,0,0,0,0,0,0,0,0,0,0,0,0,0,0,0],
  [-0.0235 - 0.0229*I, 0, 0.0111, 0, 0, 0, 0, 0,  0.0042 +
  0.0160*I, 0, -0.0026 + 0.0084*I, 0, 0, 0, 0, 0],
  [0,0,0,0,0,0,0,0,0,0,0,0,0,0,0,0],
  [0,0,0,0,0,0,0,0,0,0,0,0,0,0,0,0],
  [0,0,0,0,0,0,0,0,0,0,0,0,0,0,0,0],
  [0,0,0,0,0,0,0,0,0,0,0,0,0,0,0,0],
  [0,0,0,0,0,0,0,0,0,0,0,0,0,0,0,0],
  [ -0.0458 + 0.0361*I, 0, 0.0042 - 0.0160*I, 0, 0, 0, 0, 0,
  0.0249, 0, 0.0112 + 0.0184*I, 0, 0, 0, 0, 0],
  [0,0,0,0,0,0,0,0,0,0,0,0,0,0,0,0],
  [0.3919 + 0.1710*I, 0, -0.0026 - 0.0084*I, 0, 0, 0, 0, 0,
  0.0112 - 0.0184*I, 0, 0.4245, 0, 0, 0, 0, 0],
  [0,0,0,0,0,0,0,0,0,0,0,0,0,0,0,0],
  [0,0,0,0,0,0,0,0,0,0,0,0,0,0,0,0],
  [0,0,0,0,0,0,0,0,0,0,0,0,0,0,0,0],
  [0,0,0,0,0,0,0,0,0,0,0,0,0,0,0,0],
  [0,0,0,0,0,0,0,0,0,0,0,0,0,0,0,0]]);
```

CHWP: target is qubit 3, control: qubit 4, logical 0 (HWP at 22.5 at the transmitted arm)

```
> HWP1:=Kron(Id,Kron(Id, evalf(NZCHWP(22.5*Pi/180))));
```

CHWP: target is qubit 3, control: qubit 4, logical 1 (HWP at -22.5 at the reflected arm)

```
> HWP2:=Kron(Id, Kron(Id, evalf(NCHWP(-(22.5)*Pi/180)))) ;
```

CHWP: Target is qubit 1, control: qubit 2, logical 1 (HWP at horizontal to apply the controlled-Z)

```
> HWP3:=Kron(Kron(evalf(NCHWP(Pi/2)), Id), Id);
```

Graph Preperation:

```
> GP:=HWP3.HWP2.HWP1.BSBS;
> C:=1/sqrt(16)*Vector([1, 1, 1, -1, 1, 1, 1, -1, 1, -1, -1, -1,
  -1, 1, 1, 1]);
> CDP:=C.HermitianTranspose(C);
> graphX:=GP.DMX.HermitianTranspose(GP);
> evalf(Trace(graphX.CDP));
```

$$0.8633316453 - 1.\ 10^{-11}\ I \qquad \textbf{(3.5)}$$

```
> graphP:=GP.CD.HermitianTranspose(GP);
> Trace(graphP.CDP);
```

$$0.9880197359 + 0.\ I \qquad \textbf{(3.6)}$$

General formulea for measurment rotations:

Outcome of measuring in HH: M= H tensor Id tensor H tensor Id

```
> H:=Matrix([[1, 0], [0,0]]);
> MHHP:=Kron(H, Kron(Id, Kron(H, Id)));
> Hadamard := 1/sqrt(2)* Matrix([[1, 1], [1, -1]]);
```

The output or the state of path qubits for each tomography setting on the polarization qubits

Measurement bases

Rotation that takes H to H

```
> RHH:= evalf(HWP(0*Pi/180).QWP(0*Pi/180));
```

Rotation that takes V to H

```
> RVH:= evalf(HWP(45*Pi/180).QWP(0*Pi/180));
```

Rotation that takes D to H

```
> RDH:= evalf(HWP(22.5*Pi/180).QWP(45*Pi/180));
```

Rotation that takes A to H

```
> RAH:= evalf(HWP(67.5*Pi/180).QWP(45*Pi/180));
```

Rotation that takes L to H

```
> RLH:= evalf(HWP(67.5*Pi/180).QWP(0*Pi/180));
```

Rotation that takes R to H

```
> RRH:= evalf(HWP(22.5*Pi/180).QWP(0*Pi/180));
> evalf(RRH.(zero+I*one)/sqrt(2));
```

Measurement result of perfect Graph, B1 =H, B2 = H

```
> HH16:= Kron(RHH, Kron(Id, Kron(RHH, Id)));
> HHCDP:=MHHP.HH16.CDP.HermitianTranspose(HH16).
  HermitianTranspose(MHHP)/(Trace(HermitianTranspose(MHHP).
  HermitianTranspose(HH16).CDP.HH16.MHHP));
> HHCDX:=MHHP.HH16.graphX.HermitianTranspose(HH16).
```

```
HermitianTranspose(MHHP)/(Trace(HermitianTranspose(MHHP).
HermitianTranspose(HH16).graphX.HH16.MHHP));
> evalm(HHCDX);
> #evalm(HHCDP);
> Trace(HHCDX.HHCDP);
```

$$0.9648488733 + 0.\,I \qquad \textbf{(5.1.1.1)}$$

```
> Trace(HHCDX.HHCDX);
```

$$0.9682480268 - 4.727991982\ 10^{-18}\,I \qquad \textbf{(5.1.1.2)}$$

Effect of visibility on purity and fidelity

```
> Id16:=1/16*Matrix([[1,0,0,0,0,0,0,0,0,0,0,0,0,0,0,0],
[0,1,0,0,0,0,0,0,0,0,0,0,0,0,0,0],
[0,0,1,0,0,0,0,0,0,0,0,0,0,0,0,0],
[0,0,0,1,0,0,0,0,0,0,0,0,0,0,0,0],
[0,0,0,0,1,0,0,0,0,0,0,0,0,0,0,0],
[0,0,0,0,0,1,0,0,0,0,0,0,0,0,0,0],
[0,0,0,0,0,0,1,0,0,0,0,0,0,0,0,0],
[0,0,0,0,0,0,0,1,0,0,0,0,0,0,0,0],
[0,0,0,0,0,0,0,0,1,0,0,0,0,0,0,0],
[0,0,0,0,0,0,0,0,0,1,0,0,0,0,0,0],
[0,0,0,0,0,0,0,0,0,0,1,0,0,0,0,0],
[0,0,0,0,0,0,0,0,0,0,0,1,0,0,0,0],
[0,0,0,0,0,0,0,0,0,0,0,0,1,0,0,0],
[0,0,0,0,0,0,0,0,0,0,0,0,0,1,0,0],
[0,0,0,0,0,0,0,0,0,0,0,0,0,0,1,0],
[0,0,0,0,0,0,0,0,0,0,0,0,0,0,0,1]]);
> #evalm(Id16);
> HHCDXNP:=0.94*HHCDX+0.06*Id16;
> PurityHHCDX:=Trace(HHCDX.HHCDX);
```

$$\text{PurityHHCDX} := 0.9682480268 - 4.727991982\ 10^{-18}\,I \qquad \textbf{(5.1.1.1.1)}$$

```
> PurityHHCDXNP:=Trace(HHCDXNP.HHCDXNP);
```

$$\text{PurityHHCDXNP} := 0.8628189564 - 4.401005128\ 10^{-18}\,I \qquad \textbf{(5.1.1.1.2)}$$

```
> FIdelityHHCDXNP:=Trace(HHCDXNP.HHCDP);
```

$$\text{FIdelityHHCDXNP} := 0.9107079409 + 0.\,I \qquad \textbf{(5.1.1.1.3)}$$

Measurement result of perfect Graph, B1 =V, B2 = H

```
> VH16:= Kron(RVH, Kron(Id, Kron(RHH, Id)));
> VHCDP:=MHHP.VH16.CDP.HermitianTranspose(VH16).
HermitianTranspose(MHHP)/(Trace(HermitianTranspose(MHHP).
HermitianTranspose(VH16).CDP.VH16.MHHP));
> VHCDX:=MHHP.VH16.graphX.HermitianTranspose(VH16).
HermitianTranspose(MHHP)/(Trace(HermitianTranspose(MHHP).
```

```
  HermitianTranspose(VH16).graphX.VH16.MHHP));
> evalm(VHCDX);
> FidelityVHCDX:=Trace(VHCDX.VHCDP);
```

$$\text{FidelityVHCDX} := 0.9351608582 + 0.\,I \qquad \textbf{(5.1.2.1)}$$

Effect of visibility on Purity and Fidelity

```
> VHCDXNP:=0.94*VHCDX+0.06*Id16;
> PurityVHCDX:=Trace(VHCDX.VHCDX);
```

$$\text{PurityVHCDX} := 0.8997737806 - 2.779141365\ 10^{-19}\,I \qquad \textbf{(5.1.2.1.1)}$$

```
> PurityVHCDXNP:=Trace(VHCDXNP.VHCDXNP);
```

$$\text{PurityVHCDXNP} := 0.8023151126 - 2.456961837\ 10^{-19}\,I \qquad \textbf{(5.1.2.1.2)}$$

```
> FIdelityVHCDXNP:=Trace(VHCDXNP.VHCDP);
```

$$\text{FIdelityVHCDXNP} := 0.8828012069 + 0.\,I \qquad \textbf{(5.1.2.1.3)}$$

Measurement result of perfect Graph, B1 =H, B2 = V

```
> HV16 := Kron(RHH, Kron(Id, Kron(RVH, Id)));
> HVCDP:=MHHP.HV16.CDP.HermitianTranspose(HV16).
  HermitianTranspose(MHHP)/evalf(Trace(HermitianTranspose
  (MHHP).MHHP.HV16.CDP.HermitianTranspose(HV16)));
> HVCDX:=MHHP.HV16.graphX.HermitianTranspose(HV16).
  HermitianTranspose(MHHP)/evalf(Trace(HermitianTranspose
  (MHHP).MHHP.HV16.graphX.HermitianTranspose(HV16)));
> evalf(evalm(HVCDX));
> FidelityHVCDX:=evalf(Trace(HVCDX.HVCDP));
```

$$\text{FidelityHVCDX} := 0.9714522819 + 0.\,I \qquad \textbf{(5.1.3.1)}$$

Effect of visibility:

```
> HVCDXNP:=0.94*HVCDX+0.06*Id16;
> PurityHVCDX:=evalf(Trace(HVCDX.HVCDX));
```

$$\text{PurityHVCDX} := 0.9673495634 - 7.047324502\ 10^{-19}\,I \qquad \textbf{(5.1.3.1.1)}$$

```
> PurityHVCDXNP:=evalf(Trace(HVCDXNP.HVCDXNP));
```

$$\text{PurityHVCDXNP} := 0.8620250742 - 6.227015934\ 10^{-19}\,I \qquad \textbf{(5.1.3.1.2)}$$

```
> FIdelityHVCDXNP:=evalf(Trace(HVCDXNP.HVCDP));
```

$$\text{FIdelityHVCDXNP} := 0.9169151448 - 2.\ 10^{-28}\,I \qquad \textbf{(5.1.3.1.3)}$$

Measurement result of perfect Graph, B1 =V, B2 = V

```
> VV16 := Kron(RVH, Kron(Id, Kron(RVH, Id)));
> VVCDP:=MHHP.VV16.CDP.HermitianTranspose(VV16).
  HermitianTranspose(MHHP)/evalf(Trace(HermitianTranspose
  (MHHP).MHHP.VV16.CDP.HermitianTranspose(VV16)));
> VVCDX:=MHHP.VV16.graphX.HermitianTranspose(VV16).
  HermitianTranspose(MHHP)/evalf(Trace(HermitianTranspose
  (MHHP).MHHP.VV16.graphX.HermitianTranspose(VV16)));
> evalf(evalm(VVCDX));
```

```
> FidelityVVCDX:=evalf(Trace(VVCDX.VVCDP));
```

$$\text{FidelityVVCDX} := 0.9315895919 + 0.\,I \tag{5.1.4.1}$$

Effect of visibility:

```
> VVCDXNP:=0.94*VVCDX+0.06*Id16;
> PurityVVCDX:=evalf(Trace(VVCDX.VVCDX));
```

$$\text{PurityVVCDX} := 0.9013929659 - 5.708777159\ 10^{-19}\,I \tag{5.1.4.2}$$

```
> PurityVVCDXNP:=evalf(Trace(VVCDXNP.VVCDXNP));
```

$$\text{PurityVVCDXNP} := 0.8037458248 - 5.044275498\ 10^{-19}\,I \tag{5.1.4.3}$$

```
> FIdelityVVCDXNP:=evalf(Trace(VVCDXNP.VVCDP));
```

$$\text{FIdelityVVCDXNP} := 0.8794442164 + 1.\ 10^{-28}\,I \tag{5.1.4.4}$$

Measurement result of perfect Graph, B1 =R, B2 = V

```
> RV16 :=  Kron(RRH, Kron(Id, Kron(RVH, Id)));
> RVCDP:=MHHP.RV16.CDP.HermitianTranspose(RV16).
  HermitianTranspose(MHHP)/evalf(Trace(HermitianTranspose
  (MHHP).MHHP.RV16.CDP.HermitianTranspose(RV16)));
> RVCDX:=MHHP.RV16.graphX.HermitianTranspose(RV16).
  HermitianTranspose(MHHP)/evalf(Trace(HermitianTranspose
  (MHHP).MHHP.RV16.graphX.HermitianTranspose(RV16)));
> evalm(evalf(RVCDP));
> FidelityRVCDX:=evalf(Trace(RVCDX.RVCDP));
```

$$\text{FidelityRVCDX} := 0.8689342793 - 1.5\ 10^{-11}\,I \tag{5.1.5.1}$$

Effect of visibility:

```
> RVCDXNP:=0.94*RVCDX+0.06*Id16;
> PurityRVCDX:=evalf(Trace(RVCDX.RVCDX));
```

$$\text{PurityRVCDX} := 0.8374854533 + 3.031662009\ 10^{-11}\,I \tag{5.1.5.2}$$

```
> PurityRVCDXNP:=evalf(Trace(RVCDXNP.RVCDXNP));
```

$$\text{PurityRVCDXNP} := 0.7472771461 + 2.678776549\ 10^{-11}\,I \tag{5.1.5.3}$$

```
> FIdelityRVCDXNP:=evalf(Trace(RVCDXNP.RVCDP));
```

$$\text{FIdelityRVCDXNP} := 0.8205482228 - 2.125525728\ 10^{-11}\,I \tag{5.1.5.4}$$

Measurement result of perfect Graph, B1 =R, B2 = H

```
> RH16 := Kron(RRH, Kron(Id, Kron(RHH, Id)));
> RHCDP:=MHHP.RH16.CDP.HermitianTranspose(RH16).
  HermitianTranspose(MHHP)/(Trace(HermitianTranspose(MHHP).
  MHHP.RH16.CDP.HermitianTranspose(RH16)));
> RHCDX:=MHHP.RH16.graphX.HermitianTranspose(RH16).
  HermitianTranspose(MHHP)/(Trace(HermitianTranspose(MHHP).
  MHHP.RH16.graphX.HermitianTranspose(RH16)));
> evalm(evalf(RHCDP));
> evalm(evalf(RHCDX));
> FidelityRHCDX:=Trace(RHCDX.RHCDP);
```

(5.1.6.1)

FidelityRHCDX := 0.8639595216 + 1. 10^{-12} I **(5.1.6.1)**

Effect of visibility:

```
> RHCDXNP:=0.94*RHCDX+0.06*Id16;
> PurityRHCDX:=evalf(Trace(RHCDX.RHCDX));
```

PurityRHCDX := 0.8487329760 + 4.153228294 10^{-17} I **(5.1.6.2)**

```
> PurityRHCDXNP:=evalf(Trace(RHCDXNP.RHCDXNP));
```

PurityRHCDXNP := 0.7572154577 + 3.787969251 10^{-17} I **(5.1.6.3)**

```
> FIdelityRHCDXNP:=evalf(Trace(RHCDXNP.RHCDP));
```

FIdelityRHCDXNP := 0.8158719503 + 0. I **(5.1.6.4)**

Measurement result of perfect Graph, B1 =D, B2 = V

```
> DV16 := Kron(RDH, Kron(Id, Kron(RVH, Id)));
> DVCDP:=MHHP.DV16.CDP.HermitianTranspose(DV16).
  HermitianTranspose(MHHP)/evalf(Trace(HermitianTranspose
  (MHHP).MHHP.DV16.CDP.HermitianTranspose(DV16)));
> DVCDX:=MHHP.DV16.graphX.HermitianTranspose(DV16).
  HermitianTranspose(MHHP)/evalf(Trace(HermitianTranspose
  (MHHP).MHHP.DV16.graphX.HermitianTranspose(DV16)));
> evalm(evalf(DVCDP));
> evalm(evalf(DVCDX));
> FidelityDVCDX:=Trace(DVCDX.DVCDP);
```

FidelityDVCDX := 0.8562074297 − 2.46041240 10^{-13} I **(5.1.7.1)**

Effect of visibility:

```
> DVCDXNP:=0.94*DVCDX+0.06*Id16;
> PurityDVCDX:=evalf(Trace(DVCDX.DVCDX));
```

PurityDVCDX := 0.8415165505 − 4.702515185 10^{-17} I **(5.1.7.2)**

```
> PurityDVCDXNP:=evalf(Trace(DVCDXNP.DVCDXNP));
```

PurityDVCDXNP := 0.7508390240 − 4.208827091 10^{-17} I **(5.1.7.3)**

```
> FIdelityDVCDXNP:=evalf(Trace(DVCDXNP.DVCDP));
```

FIdelityDVCDXNP := 0.8085849839 + 1.88721234 10^{-13} I **(5.1.7.4)**

Measurement result of perfect Graph, B1 =D, B2 = H

```
> DH16 := Kron(RDH, Kron(Id, Kron(RHH, Id)));
> DHCDP:=MHHP.DH16.CDP.HermitianTranspose(DH16).
  HermitianTranspose(MHHP)/evalf(Trace(HermitianTranspose
  (MHHP).MHHP.DH16.CDP.HermitianTranspose(DH16)));
> DHCDX:=MHHP.DH16.graphX.HermitianTranspose(DH16).
  HermitianTranspose(MHHP)/evalf(Trace(HermitianTranspose
  (MHHP).MHHP.DH16.graphX.HermitianTranspose(DH16)));
> evalm(evalf(DHCDX));
```

```
> FidelityDHCDX:=Trace(DHCDX.DHCDP);
```

$$\text{FidelityDHCDX} := 0.8503205582 + 0.\,I \qquad \textbf{(5.1.8.1)}$$

Effect of visibility:

```
> DHCDXNP:=0.94*DHCDX+0.06*Id16;
> PurityDHCDX:=evalf(Trace(DHCDX.DHCDX));
```

$$\text{PurityDHCDX} := 0.8567706643 - 3.590384246\ 10^{-17}\,I \qquad \textbf{(5.1.8.2)}$$

```
> PurityDHCDXNP:=evalf(Trace(DHCDXNP.DHCDXNP));
```

$$\text{PurityDHCDXNP} := 0.7643175590 - 3.018279600\ 10^{-17}\,I \qquad \textbf{(5.1.8.3)}$$

```
> FIdelityDHCDXNP:=evalf(Trace(DHCDXNP.DHCDP));
```

$$\text{FIdelityDHCDXNP} := 0.8030513247 + 0.\,I \qquad \textbf{(5.1.8.4)}$$

Measurement result of perfect Graph, B1 =D, B2 = R

```
> DR16 :=  Kron(RDH, Kron(Id, Kron(RRH, Id)));
> DRCDP:=MHHP.DR16.CDP.HermitianTranspose(DR16).
  HermitianTranspose(MHHP)/evalf(Trace(MHHP.DR16.CDP.
  HermitianTranspose(DR16).HermitianTranspose(MHHP)));
> DRCDX:=MHHP.DR16.graphX.HermitianTranspose(DR16).
  HermitianTranspose(MHHP)/evalf(Trace(MHHP.DR16.graphX.
  HermitianTranspose(DR16).HermitianTranspose(MHHP)));
> evalm(evalf(DRCDP));
> evalm(evalf(DRCDX));
> FidelityDRCDX:=Trace(DRCDX.DRCDP);
```

$$\text{FidelityDRCDX} := 0.8440563814 - 1.\ 10^{-11}\,I \qquad \textbf{(5.1.9.1)}$$

Effect of visibility:

```
> DRCDXNP:=0.94*DRCDX+0.06*Id16;
> PurityDRCDX:=evalf(Trace(DRCDX.DRCDX));
```

$$\text{PurityDRCDX} := 0.9143709074 - 2.435365739\ 10^{-17}\,I \qquad \textbf{(5.1.9.2)}$$

```
> PurityDRCDXNP:=evalf(Trace(DRCDXNP.DRCDXNP));
```

$$\text{PurityDRCDXNP} := 0.8152131338 - 2.095401411\ 10^{-17}\,I \qquad \textbf{(5.1.9.3)}$$

```
> FIdelityDRCDXNP:=evalf(Trace(DRCDXNP.DRCDP));
```

$$\text{FIdelityDRCDXNP} := 0.7971629986 + 0.\,I \qquad \textbf{(5.1.9.4)}$$

Measurement result of perfect Graph, B1 =D, B2 = D

```
> DD16 := Kron(RDH, Kron(Id, Kron(RDH, Id)));
> DDCDP:=MHHP.DD16.CDP.HermitianTranspose(DD16).
  HermitianTranspose(MHHP)/evalf(Trace(HermitianTranspose
  (MHHP).MHHP.DD16.CDP.HermitianTranspose(DD16)));
> DDCDX:=MHHP.DD16.graphX.HermitianTranspose(DD16).
  HermitianTranspose(MHHP)/evalf(Trace(HermitianTranspose
  (MHHP).MHHP.DD16.graphX.HermitianTranspose(DD16)));
```

```
> evalm(evalf(DDCDP));
> evalm(evalf(DDCDX));
> FidelityDDCDX:=Trace(DDCDX.DDCDP);
```

FidelityDDCDX := 0.8584524054 + 0. I **(5.1.10.1)**

Effect of visibility:

```
> DDCDXNP:=0.94*DDCDX+0.06*Id16;
> PurityDDCDX:=evalf(Trace(DDCDX.DDCDX));
```

PurityDDCDX := 0.8478270918 − 4.920938966 10^{-17} I **(5.1.10.2)**

```
> PurityDDCDXNP:=evalf(Trace(DDCDXNP.DDCDXNP));
```

PurityDDCDXNP := 0.7564150183 − 4.231334103 10^{-17} I **(5.1.10.3)**

```
> FIdelityDDCDXNP:=evalf(Trace(DDCDXNP.DDCDP));
```

FIdelityDDCDXNP := 0.8106952611 + 0. I **(5.1.10.4)**

Measurement result of perfect Graph, B1 =R, B2 = D

```
> RD16 := Kron(RRH, Kron(Id, Kron(RDH, Id)));
> RDCDP:=MHHP.RD16.CDP.HermitianTranspose(RD16).
  HermitianTranspose(MHHP)/evalf(Trace(HermitianTranspose
  (MHHP).MHHP.RD16.CDP.HermitianTranspose(RD16)));
> RDCDX:=MHHP.RD16.graphX.HermitianTranspose(RD16).
  HermitianTranspose(MHHP)/evalf(Trace(HermitianTranspose
  (MHHP).MHHP.RD16.graphX.HermitianTranspose(RD16)));
> evalm(evalf(RDCDP));
> evalm(evalf(RDCDX));
> FidelityRDCDX:=Trace(RDCDX.RDCDP);
```

FidelityRDCDX := 0.8701658844 + 0. I **(5.1.11.1)**

Effect of visibility:

```
> RDCDXNP:=0.94*RDCDX+0.06*Id16;
> PurityRDCDX:=evalf(Trace(RDCDX.RDCDX));
```

PurityRDCDX := 0.8424768336 − 5.709950721 10^{-17} I **(5.1.11.2)**

```
> PurityRDCDXNP:=evalf(Trace(RDCDXNP.RDCDXNP));
```

PurityRDCDXNP := 0.7516875303 − 5.071562396 10^{-17} I **(5.1.11.3)**

```
> FIdelityRDCDXNP:=evalf(Trace(RDCDXNP.RDCDP));
```

FIdelityRDCDXNP := 0.8217059312 + 0. I **(5.1.11.4)**

Measurement result of perfect Graph, B1 =H, B2 = D

```
> HD16 := Kron(RHH, Kron(Id, Kron(RDH, Id)));
> HDCDP:=MHHP.HD16.CDP.HermitianTranspose(HD16).
  HermitianTranspose(MHHP)/evalf(Trace(HermitianTranspose
  (MHHP).MHHP.HD16.CDP.HermitianTranspose(HD16)));
> HDCDX:=MHHP.HD16.graphX.HermitianTranspose(HD16).
  HermitianTranspose(MHHP)/evalf(Trace(HermitianTranspose
```

```
   (MHHP).MHHP.HD16.graphX.HermitianTranspose(HD16)));
> evalm(evalf(HDCDX));
```

```
> evalf(HDCDX.HDCDP);
```

$$0.9662477776 - 3.558\ 10^{-18}\ I \qquad \textbf{(5.1.12.1)}$$

Effect of visibility:

```
> HDCDXNP:=0.94*HDCDX+0.06*Id16;
> PurityHDCDX:=evalf(Trace(HDCDX.HDCDX));
```

$$\text{PurityHDCDX} := 0.9620930113 - 1.841547008\ 10^{-17}\ I \qquad \textbf{(5.1.12.2)}$$

```
> PurityHDCDXNP:=evalf(Trace(HDCDXNP.HDCDXNP));
```

$$\text{PurityHDCDXNP} := 0.8573803848 - 1.619526069\ 10^{-17}\ I \qquad \textbf{(5.1.12.3)}$$

```
> FIdelityHDCDXNP:=evalf(Trace(HDCDXNP.HDCDP));
```

$$\text{FIdelityHDCDXNP} := 0.9120229109 - 3.345\ 10^{-18}\ I \qquad \textbf{(5.1.12.4)}$$

Measurement result of perfect Graph, B1 =V, B2 = D

```
> VD16 := Kron(RVH, Kron(Id, Kron(RDH, Id)));
> VDCDP:=MHHP.VD16.CDP.HermitianTranspose(VD16).
  HermitianTranspose(MHHP)/evalf(Trace(HermitianTranspose
  (MHHP).MHHP.VD16.CDP.HermitianTranspose(VD16)));
> VDCDX:=MHHP.VD16.graphX.HermitianTranspose(VD16).
  HermitianTranspose(MHHP)/evalf(Trace(HermitianTranspose
  (MHHP).MHHP.VD16.graphX.HermitianTranspose(VD16)));
> evalm(evalf(VDCDX));
```

```
> evalf(VDCDX.VDCDP);
```

$$0.9427280388 - 3.781\ 10^{-18}\ I \qquad \textbf{(5.1.13.1)}$$

Effect of visibility:

```
> VDCDXNP:=0.94*VDCDX+0.06*Id16;
> PurityVDCDX:=evalf(Trace(VDCDX.VDCDX));
```

$$\text{PurityVDCDX} := 0.9135965043 - 6.010487642\ 10^{-18}\ I \qquad \textbf{(5.1.13.2)}$$

```
> PurityVDCDXNP:=evalf(Trace(VDCDXNP.VDCDXNP));
```

$$\text{PurityVDCDXNP} := 0.8145288713 - 5.418831326\ 10^{-18}\ I \qquad \textbf{(5.1.13.3)}$$

```
> FIdelityVDCDXNP:=evalf(Trace(VDCDXNP.VDCDP));
```

$$\text{FIdelityVDCDXNP} := 0.8899143565 - 3.553\ 10^{-18}\ I \qquad \textbf{(5.1.13.4)}$$

Measurement result of perfect Graph, B1 =V, B2 = L

```
> VL16 := Kron(RVH, Kron(Id, Kron(RLH, Id)));
> VLCDP:=(MHHP.VL16.CDP.HermitianTranspose(VL16).
  HermitianTranspose(MHHP))/evalf(Trace(MHHP.VL16.CDP.
  HermitianTranspose(VL16).HermitianTranspose(MHHP)));
```

```
> VLCDX:=(MHHP.VL16.graphX.HermitianTranspose(VL16).
  HermitianTranspose(MHHP))/evalf(Trace(MHHP.VL16.graphX.
  HermitianTranspose(VL16).HermitianTranspose(MHHP)));
> evalm(evalf(VLCDX));
> FidelityVLCDX:=Trace(VLCDX.VLCDP);
```

$$\text{FidelityVLCDX} := 0.9880197362 - 9.87\ 10^{-18}\ I \qquad \textbf{(5.1.14.1)}$$

Effect of visibility:

```
> VLCDXNP:=0.94*VLCDX+0.06*Id16;
> PurityVLCDX:=evalf(Trace(VLCDX.VLCDX));
```

$$\text{PurityVLCDX} := 1.000000000 - 1.817165642\ 10^{-17}\ I \qquad \textbf{(5.1.14.2)}$$

```
> PurityVLCDXNP:=evalf(Trace(VLCDXNP.VLCDXNP));
```

$$\text{PurityVLCDXNP} := 0.8908750002 - 1.605647560\ 10^{-17}\ I \qquad \textbf{(5.1.14.3)}$$

```
> FIdelityVLCDXNP:=evalf(Trace(VLCDXNP.VLCDP));
```

$$\text{FIdelityVLCDXNP} := 0.9324885521 - 9.27\ 10^{-18}\ I \qquad \textbf{(5.1.14.4)}$$

Measurement result of perfect Graph, B1 =H, B2 = L

```
> HL16 := Kron(RHH, Kron(Id, Kron(RLH, Id)));
> HLCDP:=MHHP.HL16.CDP.HermitianTranspose(HL16).
  HermitianTranspose(MHHP)/evalf(Trace(HermitianTranspose
  (MHHP).MHHP.HL16.CDP.HermitianTranspose(HL16)));
> HLCDX:=MHHP.HL16.graphX.HermitianTranspose(HL16).
  HermitianTranspose(MHHP)/evalf(Trace(HermitianTranspose
  (MHHP).MHHP.HL16.graphX.HermitianTranspose(HL16)));
> evalm(evalf(HLCDX));
> evalf(HLCDX.HLCDP);
```

$$0.9880197361 - 4.195\ 10^{-17}\ I \qquad \textbf{(5.1.15.1)}$$

Effect of visibility:

```
> HLCDXNP:=0.94*HLCDX+0.06*Id16;
```

$$\text{HLCDXNP} := \begin{bmatrix} 16 \text{ x } 16 \text{ Matrix} \\ \text{Data Type: complex}_8 \\ \text{Storage: rectangular} \\ \text{Order: Fortran\_order} \end{bmatrix} \qquad \textbf{(5.1.15.2)}$$

```
> PurityHLCDX:=evalf(Trace(HLCDX.HLCDX));
```

$$\text{PurityHLCDX} := 1.000000000 - 7.973278432\ 10^{-17}\ I \qquad \textbf{(5.1.15.3)}$$

```
> PurityHLCDXNP:=evalf(Trace(HLCDXNP.HLCDXNP));
```

$$\text{PurityHLCDXNP} := 0.8908749999 - 7.045188824\ 10^{-17}\ I \qquad \textbf{(5.1.15.4)}$$

```
> FIdelityHLCDXNP:=evalf(Trace(HLCDXNP.HLCDP));
```

$$\text{FIdelityHLCDXNP} := 0.9324885519 - 3.943\ 10^{-17}\ I \qquad \textbf{(5.1.15.5)}$$

Measurement result of perfect Graph, B1 =R, B2 = L

```
> RL16 := Kron(RRH, Kron(Id, Kron(RLH, Id)));
> RLCDP:=MHHP.RL16.CDP.HermitianTranspose(RL16).
  HermitianTranspose(MHHP)/(Trace(HermitianTranspose(MHHP).
  MHHP.RL16.CDP.HermitianTranspose(RL16)));
> RLCDX:=MHHP.RL16.graphX.HermitianTranspose(RL16).
  HermitianTranspose(MHHP)/(Trace(HermitianTranspose(MHHP).
  MHHP.RL16.graphX.HermitianTranspose(RL16)));
> evalm(evalf(RLCDX));

> evalf(RLCDX.RLCDP);
```

$$0.9244344936 - 4.33\ 10^{-17}\ I \qquad \textbf{(5.1.16.1)}$$

Effect of visibility:

```
> RLCDXNP:=0.94*RLCDX+0.06*Id16;
```

$$\text{RLCDXNP} := \begin{bmatrix} 16 \text{ x } 16 \text{ Matrix} \\ \text{Data Type: complex}_8 \\ \text{Storage: rectangular} \\ \text{Order: Fortran\_order} \end{bmatrix} \qquad \textbf{(5.1.16.2)}$$

```
> PurityRLCDX:=evalf(Trace(RLCDX.RLCDX));
```

$$\text{PurityRLCDX} := 0.8991396670 - 9.124934864\ 10^{-17}\ I \qquad \textbf{(5.1.16.3)}$$

```
> PurityRLCDXNP:=evalf(Trace(RLCDXNP.RLCDXNP));
```

$$\text{PurityRLCDXNP} := 0.8017548098 - 8.044238515\ 10^{-17}\ I \qquad \textbf{(5.1.16.4)}$$

```
> FIdelityRLCDXNP:=evalf(Trace(RLCDXNP.RLCDP));
```

$$\text{FIdelityRLCDXNP} := 0.8727184240 - 4.07\ 10^{-17}\ I \qquad \textbf{(5.1.16.5)}$$

Measurement result of perfect Graph, w01 =0, w02 = Pi/2 = RRH

```
> assign(HM, HWP(``*``(``+``(``*``(22.5, ``*``(π))), ``/``(1, 180))))
> assign(HR16, Kron(HM, Kron(Id, Kron(RRH, Id))))
> HRCDP:=MHHP.HR16.CDP.HermitianTranspose(HR16).
  HermitianTranspose(MHHP)/evalf(Trace(HermitianTranspose
  (MHHP).MHHP.HR16.CDP.HermitianTranspose(HR16)));
> HRCDX:=MHHP.HR16.graphX.HermitianTranspose(HR16).
  HermitianTranspose(MHHP)/evalf(Trace(HermitianTranspose
  (MHHP).MHHP.HR16.graphX.HermitianTranspose(HR16)));
> evalm(evalf(HRCDX));
> evalf(HRCDX.HRCDP);
> evalf(HRCDX.HRCDP);
```

$$0.8440563818 + 2.135568967\ 10^{-11}\ I \qquad \textbf{(5.1.17.1)}$$

Effect of visibility:

```
> HRCDXNP:=0.94*HRCDX+0.06*Id16;
```

```
> PurityHRCDX:=evalf(Trace(HRCDX.HRCDX));
```

$$\text{PurityHRCDX} := 0.9143709081 + 8.386823920\ 10^{-11}\ I \qquad \textbf{(5.1.17.2)}$$

```
> PurityHRCDXNP:=evalf(Trace(HRCDXNP.HRCDXNP));
```

$$\text{PurityHRCDXNP} := 0.8152131340 + 7.410597619\ 10^{-11}\ I \qquad \textbf{(5.1.17.3)}$$

```
> FIdelityHRCDXNP:=evalf(Trace(HRCDXNP.HRCDP));
```

$$\text{FIdelityHRCDXNP} := 0.7971629989 + 1.501798120\ 10^{-11}\ I \qquad \textbf{(5.1.17.4)}$$

Measurement result of perfect Graph, w01=0, w02 = 0

```
> HH16:=Kron(HM, Kron(Id, Kron(HM, Id)));
> HHCDP:=MHHP.HH16.CDP.HermitianTranspose(HH16).MHHP/(Trace
  (MHHP.HH16.CDP.HermitianTranspose(HH16).MHHP)):
> HHCDX:=MHHP.HH16.graphX.HermitianTranspose(HH16).MHHP/
  (Trace(MHHP.HH16.graphX.HermitianTranspose(HH16).MHHP)):
> evalm(evalf(HHCDX));
> evalf(HHCDX.HHCDP);
```

$$0.8584524054 + 2.956365723\ 10^{-11}\ I \qquad \textbf{(5.1.18.1)}$$

Effect of visibility:

```
> HHCDXNP:=0.94*HHCDX+0.06*Id16;
> PurityHHCDX:=evalf(Trace(HHCDX.HHCDX));
```

$$\text{PurityHHCDX} := 0.8478270915 + 1.580857631\ 10^{-11}\ I \qquad \textbf{(5.1.18.2)}$$

```
> PurityHHCDXNP:=evalf(Trace(HHCDXNP.HHCDXNP));
```

$$\text{PurityHHCDXNP} := 0.7564150182 + 1.394606461\ 10^{-11}\ I \qquad \textbf{(5.1.18.3)}$$

```
> FIdelityHHCDXNP:=evalf(Trace(HHCDXNP.HHCDP));
```

$$\text{FIdelityHHCDXNP} := 0.8106952611 + 2.958983780\ 10^{-11}\ I \qquad \textbf{(5.1.18.4)}$$

Measurement result of perfect Graph, B1 =R, B2 = R, or theta1 = theta2 = Pi/2.

```
> RR16 := Kron(RRH, Kron(Id, Kron(RRH, Id)));
> RRCDP:=MHHP.RR16.CDP.HermitianTranspose(RR16).
  HermitianTranspose(MHHP)/evalf(Trace(HermitianTranspose(MHHP).
  MHHP.RR16.CDP.HermitianTranspose(RR16)));
> RRCDX:=MHHP.RR16.graphX.HermitianTranspose(RR16).
  HermitianTranspose(MHHP)/evalf(Trace(HermitianTranspose(MHHP).
  MHHP.RR16.graphX.HermitianTranspose(RR16)));
> evalm(evalf(RRCDX));
> evalf(RRCDX.RRCDP);
```

$$0.8332170416 + 2.400\ 10^{-17}\ I \qquad \textbf{(6.1)}$$

Effect of visibility:

```
> RRCDXNP:=0.94*RRCDX+0.06*Id16;
> PurityRRCDX:=evalf(Trace(RRCDX.RRCDX));
```

(6.2)

$$\text{PurityRRCDX} := 0.8579917418 + 4.409155521\ 10^{-17}\ I \quad \textbf{(6.2)}$$

```
> PurityRRCDXNP:=evalf(Trace(RRCDXNP.RRCDXNP));
```

$$\text{PurityRRCDXNP} := 0.7653965030 + 3.834182225\ 10^{-17}\ I \quad \textbf{(6.3)}$$

```
> FIdelityRRCDXNP:=evalf(Trace(RRCDXNP.RRCDP));
```

$$\text{FIdelityRRCDXNP} := 0.7869740191 + 2.264\ 10^{-17}\ I \quad \textbf{(6.4)}$$

Appendix F

Tomography Results with Error Bars

These results are calculated using the code borrowed from Julio Barreiro. The code is capable of estimating the error bars on the fidelity of density matrices using Monte Carlo simulations in a very efficient manner. However, it requires over complete set of data for Maximum Likelihood reconstruction. Our experimental data were only complete, hence, to be able to use this code, we have extrapolated the over-complete set of data from the available complete set. It is for this reason that this data is not reported in the body of the thesis and is presented in this appendix. For the Monte Carlo simulation, we have chosen 200 data points from the Poisson distribution. The results are shown in the following figure.

Basis	Exp reconstruction from Julio's Code error bar estimated with n = 200
HH	0.832 ± 0.005
HV	0.856 ± 0.004
VH	0.955 ± 0.002
VV	0.933 ± 0.002
RH	0.797 ± 0.005
RV	0.623 ± 0.006
DV	0.656 ± 0.008
DH	0.703 ± 0.007
DR	0.751 ± 0.006
DD	0.552 ± 0.008, purity = 0.87
RD	0.840 ± 0.006
HD	0.908 ± 0.003
VD	0.929 ± 0.003
VL	0.952 ± 0.003
HL	0.879 ± 0.004
RL	0.847 ± 0.005

Basis	Exp reconstruction from Julio's Code, error bar estimated with n = 200
0, pi/2	0.865 ± 0.004
0,0	0.888 ± 0.005
pi/2, pi/2	0.740 ± 0.005
Source	0.885 ± 0.005

Figure F.1 The results of the experiment reported with error bars. The error bars are calculated from the Monte Carlo simulation with 200 data points.

Appendix G

Contributions to the Field

Please note that the main results for the experimental work presented in this thesis is not published as a journal paper yet, however it is presented in two conferences, namely Fio 2011 (San Jose, CA) and CQIQC 2011 (Toronto).

Publications

1. Seth Lloyd, Lorenzo Maccone, Raul Garcia-Patron, Vittorio Giovannetti, Yutaka Shikano, Stefano Pirandola, Lee A. Rozema, Ardavan Darabi, Yasaman Soudagar, Lynden K. Shalm, and Aephraim M. Steinberg, "Closed Timelike Curves via Postselection: Theory and Experimental Test of Consistency," Phys. Rev. Lett. 106, 040403 (2011)
2. Soudagar Y., et al., "Cluster-state quantum computing in optical fibres," Journal of Optical Society of America B, Vol. 24, No. 2. Accepted on 27 June 2006
3. Bussieres, F., et al., "Manipulating time-bin qubits with fiber optics components," Digest of the LEOS Summer Topical Meetings (IEEE Cat. No. 06TH8863C), 2006, p 22-25.

Conference Publications and Attendances

1. Soudagar Y., et al, "Experimental Demonstration of a 4-qubit Loop Graph for One-way Quantum Computing," Frontier in Optics, San Jose, USA, 2011
2. Soudagar Y., et al, "A photonic loop-graph state for one-way quantum computing," CQIQC (Toronto, Canada), 2011
3. Darabi A, et al, "Violation of Heisenberg's Precision Limit by Weak Measurement Using a Composite Circuit One-Way model of Quantum Computing," CQIQC (Toronto, Canada), 2011
4. Soudagar Y.., et al., "Experimental realization of Closed Timelike Curves via Postselection," Cross Border (Ottawa, Canada), 2010
5. Soudagar Y. "Quantum NOON states and sensing," department seminar, Department of Physics Engineering, École Polytechnique de Montréal, 2010
6. Soudagar Y., et al, "Demonstration of a 4-qubit Hyperentangled Loop Cluster," QIPC (Rome, Italy), 2009

7. Soudagar Y., et al., “Demonstration of a Loop Cluster for Quantum Information Applications,” CLEO (Baltimore, USA), 2009

8. Soudagar Y. “The Cluster State Model of Quantum Computation,” department seminar, Department of Physics Engineering, École Polytechnique de Montréal, 2006